Recent Progress on All-Inorganic Metal Halide Perovskite Solar Cells

Jia Liang[1*], Yabing Qi[2*]

[1]Department of Materials Science, Fudan University, 220 Handan Road, Shanghai, 200433, China
[2]Energy Materials and Surface Science Unit (EMSSU), Okinawa Institute of Science and Technology Graduate University (OIST), 1919-1 Tancha, Onna-son, Okinawa 904-0495, Japan

*Corresponding authors: Jia Liang, Email: jialiang@fudan.edu.cn; Yabing Qi, Email: Yabing.Qi@OIST.jp

Abstract

Metal halide perovskites have attracted tremendous interest because of their unique chemical and physical properties. Among them, organic-inorganic metal halide (OMH) perovskite solar cells (PSCs) exhibit a rapid development with the power conversion efficiency (PCE) increased from initially 3.8% to nowadays 25.5%. However, the inherent chemical instability of these materials against moisture, heat and ultraviolet light hinders their commercialization. Therefore, by replacing organic cations with inorganic cations, all-inorganic metal halide (IMH) PSCs are regarded as promising alternatives, and their PCEs have exceeded 20% since the first report in 2015. In this review, we discuss the latest progress of IMH perovskites and their applications in solar cells, which is followed by a summary of existent challenges in the IMH PSC field and an outlook on future development.

Keywords: perovskites, all-inorganic, solar cells, $CsPbBr_3$, $CsPb(I_xBr_{1-x})_3$, $CsPbI_3$

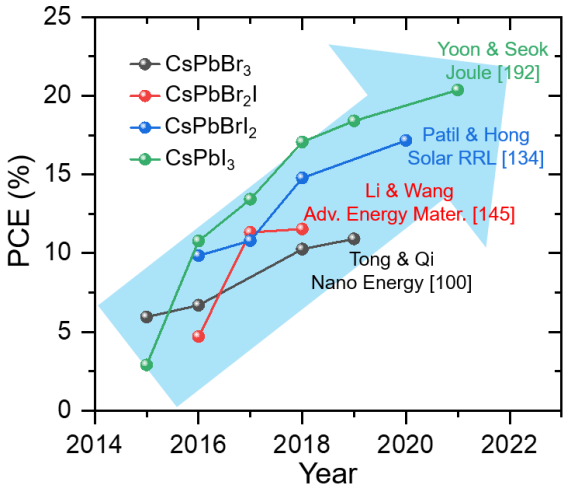

1. Introduction

For the past twelve years, organic-inorganic metal halide (OMH) perovskites have attracted much attention because they possess unique chemical and physical properties, such as long carrier lifetime, large carrier mobility, high optical absorption, small effective mass and exceeding 25%

power conversion efficiency (PCE) in solar cells.[1-19] So far, typical OMH perovskites include $CH_3NH_3PbI_3$ ($MAPbI_3$) and $HC(NH_2)_2PbI_3$ ($FAPbI_3$), but the existence of organic cations makes them suffer from poor photochemical and thermal instability issues.[20-32] In order to improve the stability, a series of Cesium (Cs)-incorporated OMH perovskites have been developed, e.g., $FA_{0.9}Cs_{0.1}PbI_3$, $FA_{0.8}Cs_{0.2}PbI_{0.84}Br_{0.16}$, $Cs_{0.05}(MA_{0.17}FA_{0.83})_{0.95}Pb(I_{0.83}Br_{0.17})_3$, and so on.[33-37] Although these Cs-incorporated perovskites can display superior stability to OMH perovskites, they still face challenges for the long-term stability due to the remaining organic components.

For this reason, all-inorganic metal halide (IMH) perovskites without any organic components emerged to be alternatives since 2015 and have exhibited excellent moisture and heat resistance.[38-44] Three basic types of IMH perovskites, including $CsPbCl_3$, $CsPbBr_3$, and $CsPbI_3$, were proposed according to previous literature.[45-47] Their properties and stabilities vary. $CsPbCl_3$ is not suitable for solar cell applications because of the large bandgap (about 3.0 eV).[48-49] $CsPbBr_3$ possesses a bandgap of 2.3 eV, which is still large for solar cell applications, however, it shows a much better stability than other perovskites.[50-53] $CsPbI_3$ with a narrow bandgap of 1.7 eV [54] is a good absorber for solar energy harvesting, especially for tandem devices. However, the black phase $CsPbI_3$ is not stable and quickly degrades to a yellow non-perovskite phase at room temperature, which basically does not absorb much sun light.[54-56] Besides the three basic types, the mixed-halide IMH perovskite, $CsPb(I_xBr_{1-x})_3$ was also reported showing a narrower bandgap than $CsPbBr_3$ and better stability than $CsPbI_3$.[57-61]

In this review, we summarize the latest progress of IMH perovskites and their applications in solar cells. We first discuss the fundamental insights of IMH perovskites, including crystal structures, electronic structures, and photovoltaic properties. Then, we compare the IMH perovskite solar cells (PSCs) in terms of their compositions, including $CsPbBr_3$, $CsPb(I_xBr_{1-x})_3$ and $CsPbI_3$, as well as their structures and photovoltaic performances (**Table 1**). Finally, we present the challenges in the IMH PSC field and provide an outlook on future development.

Table 1. Summary of $CsPbX_3$-based IMH-PSCs in literature. Device configuration, power conversion efficiency (PCE), and stability/condition are compared.

Materials	Publication Year	Device Configuration	PCE (%)	Stability/Condition	Ref
$CsPbBr_3$	2016	FTO/c-TiO_2/$CsPbBr_3$/spiro/Au	5.4	-	115
	2016	FTO/d-TiO_2/mp-TiO_2/$CsPbBr_3$/PTAA/Au	6.2	No significant decay for 16 days/in air with 15–20% relative humidity (RH)	78
	2016	FTO/c-TiO_2/mp-TiO_2/$CsPbBr_3$/carbon	6.7	No significant decay for 3000 h/in air with 90–95% RH	84

	2018	FTO/GQDs/CsPbBr$_3$/PQDs/carbon	4.1	Maintaining 80% of its initial PCE for 200 h/in air with 50% RH	116
	2018	FTO/mp-TiO$_2$/CsPbBr$_3$/PTAA/Au	5.95	-	77
	2018	FTO/c-TiO$_2$/CsPbBr$_3$/spiro/Au	6.95	No significant decay for 60 days/in air with 30% RH	98
	2018	FTO/c-TiO$_2$/CsPbBr$_3$/carbon	8.86	Maintaining 86% of its initial PCE for 30 days/an environmental chamber with 25–35% RH	99
	2018	FTO/c-TiO$_2$/mp-TiO$_2$/GQDs/CsPbBr$_3$/CISZ-GQDs/carbon	9.43	Maintaining 98% of its initial PCE for 40 days/in air with 80% RH	114
	2018	FTO/c-TiO$_2$/mp-TiO$_2$/GQDs/CsPbBr$_3$/carbon	9.72	Maintaining 87% of its initial PCE for 130 days/in air with90% RH	90
	2018	FTO/c-TiO$_2$/m-TiO$_2$/Cs$_{0.91}$Rb$_{0.09}$PbBr$_3$/carbon	9.86	Maintaining 97% of its initial PCE for 700 h/in air	106
	2018	FTO/c-TiO$_2$/m-TiO$_2$/CsPb$_{0.97}$Ln$_{0.03}$Br$_3$/carbon	10.14	No significant decay for 110 days/in air with 80% RH	107
	2018	FTO/c-TiO$_2$/m-TiO$_2$/CsPb$_{0.97}$Tb$_{0.03}$Br$_3$/SnS:ZnS/NiO$_x$/carbon	10.26	No significant decay for 40 days/in air with 80% RH	112
	2019	FTO/c-TiO$_2$/mp-TiO$_2$/CsPbBr$_3$/Ti$_3$C$_2$-MXene/carbon	9.01	Maintaining 80% of its initial PCE for 1900 h/in a moisture environment	108
	2019	FTO/c-TiO$_2$/m-TiO$_2$/CsPbBr$_3$/CsPbBr$_3$-CsPb$_2$Br$_5$/CsPbBr	10.17	Maintaining 85% of its initial PCE for 3000 h/in air with 45% RH	113

		$_3$-Cs_4PbBr_6/carbon			
	2019	FTO/c-TiO_2/m-TiO_2/$CsPbBr_3$/Cu(Cr,M)O_2/carbon	10.18	No significant decay for 60 days/in air with 80% RH	109
	2019	FTO/c-TiO_2/m-TiO_2/$CsPbBr_3$/MnS/carbon	10.45	Maintaining 80% of its initial PCE for 90 days/in air with 80% RH	111
	2019	FTO/SnO_2/$CsPbBr_3$/$CsMBr_3$/carbon	10.60	No significant decay for 10 days/in air with 80% RH	110
	2019	FTO/c-TiO_2/$CsPbBr_3$/spiro/Ag	10.91	Maintaining 80% of its initial PCE for 30 days/in air without any encapsulation	100
	2021	FTO/L-TiO_2/Sm-$CsPbBr_3$/carbon	9.81	No significant decay for 60 days/in air with 80% RH	117
$CsPbBr_2I$	2016	FTO/c-TiO_2/$CsPbBr_2I$/Au	4.7	Good stability in N_2 environment and ambient conditions	119
	2016	FTO/d-TiO_2/mp-TiO_2/$CsPbBr_2I$/PTAA/Au	6.3	-	120
	2017	FTO/c-TiO_2/mp-TiO_2/$CsPb_{0.9}Sn_{0.1}Br_2I$/carbon	11.33	No significant decay for 90 days/in air with encapsulation	125
	2018	FTO/c-TiO_2/mp-TiO_2/$CsPb_{0.995}Mn_{0.005}Br_{1.99}I_{1.01}$/carbon	7.36	Maintaining 92% of its initial PCE for 700 h/in air with encapsulation	124
	2018	FTO/c-TiO_2/$CsPbBr_2I$/carbon	9.16	Maintaining 90% of its initial PCE for 60 days/in air with 45% RH	123
	2018	ITO/SnO_2/C_{60}/$CsPb_{0.75}Sn_{0.25}Br_2I$/spiro/Au	11.53	Maintaining 90% of its initial PCE for 120 min/in air with 50–60% RH	145

	2019	ITO/SnO_2/$CsPbBr_2I$/spiro/Ag	9.86	Maintaining 85% of its initial PCE for 30 days/in air with 35% RH	121
	2019	FTO/TiO_2(CsBr)/ $CsPbBr_2I$/carbon	10.71	-	127
	2019	FTO/TiO_2/$SmBr_3$/ $CsPbBr_2I$/PTAA/ Au	10.88	Maintaining 70% of its initial PCE for 24 h/in air without encapsulation	126
	2020	FTO/c-TiO_2/$CsPbBr_2I$/PCBM/Au	8.65	Maintaining 90% of its initial PCE for 1000 h/in air with encapsulation	122
	2020	ITO/ZnO/$CsPbBr_2I$/spiro/Ag	10.16	Maintaining 70% of its initial PCE for 800 h/in air with 15% RH	148
	2020	FTO/TiO_2/BAI:$CsPbBr_2I$/spiro/Au	10.78	Maintaining 90% of its initial PCE for 144 h/in air with 30% RH	150
	2020	ITO/SnO_2/MgO/ $CsPbBr_2I$/spiro/Ag	11.04	Maintaining 90% of its initial PCE for 1250 h/in air with 25% RH	149
	2020	FTO/TiO_2/PEG:$CsPbBr_2I$/PCBM/Ag	11.10	Maintaining 90% of its initial PCE for 600 h/in air without encapsulation	146
	2020	FTO/SnO_2/$CsPbBr_2I$-PEI/NiO_x/Au	11.30	No significant decay for 30 days/in air	147
$CsPbBrI_2$	2016	FTO/c-TiO_2/$CsPbBrI_2$/spiro/Ag	9.84	Depending upon the ambient humidity	128
	2017	FTO/c-TiO_2/$CsPbBrI_2$/P3HT/Au	7.7	Maintaining 90% of its initial PCE for 240 h/in air with encapsulation	129
	2017	FTO/c-TiO_2/$Cs_{0.925}K_{0.075}PbBrI_2$/spiro/Au	10.0	Maintaining 80% of its initial PCE for 120 h/an interior atmosphere with 20% RH	138
	2017	FTO/c-TiO_2/mp-TiO_2/$CsPb_{0.98}Sr_{0.02}BrI_2$/P3HT/Au	10.8	No significant decay after first week for 30 days/in air with 50% RH with encapsulation	137

	2018	FTO/c-TiO_2/m-TiO_2/$CsPbBrI_{1.78}F_{0.22}$/spiro/Ag	10.26	Maintaining 80% of its initial PCE for 72 h/in air with 20% RH	141
	2018	FTO/c-TiO_2/mp-TiO_2/$CsPbBrI_2$/spiro/Ag	10.56	Long-term phase stability at room temperature and at 100 ℃ for more than a week	130
	2018	FTO/SnO_2/$CsPb_{0.8}Ge_{0.2}BrI_2$/P3HT/spiro/Au	10.8	No significant decay for 7 h/in air with 50−60% RH	140
	2018	FTO/TiO_2/$Pb(Ac)_2$:$CsPbBrI_2$/PCBM/Ag	12.00	Maintaining 80% of its initial PCE for 30 days/in air with 20% RH	131
	2018	FTO/TiO_2/$CsPbBrI_2$/P3HT/Au	12.02	Maintaining 90% of its initial PCE for 960 h/in a dry glovebox	151
	2018	FTO/TiO_2/$CsPbBrI_2$/$CsPbBrI_2$ NSs/$CsPbBrI_2$ QDs/PTAA/Au	12.39	No significant decay for 60 days/in air with 25−35% RH	143
	2018	FTO/NiO_x/$CsPbBrI_2$/ZnO@C_{60}/Ag	13.3	Maintaining 80% of its initial PCE for 360 h/thermal treatment at 85 ℃	152
	2018	FTO/TiO_2/$CsPbBrI_2$/$CsPbI_2Br$ QDs/PTAA/Au	13.47	Maintaining 97% of its initial PCE for 35 days/under dark storage conditions with 25−35% RH	139
	2018	FTO/TiO_2/$CsPbBrI_2$/$CsPbI_3$ QDs/PTAA/Au	14.45	No significant decay for 3 weeks/in air with 60% RH	142
	2018	FTO/TiO_2/$CsPbBrI_2$ with DMSO-adducts/spiro/Au	14.78	No significant decay for 500 h/in air with 20% RH	154
	2019	FTO/c-TiO_2/mp-TiO_2/$CsPb_{0.95}Eu_{0.05}BrI_2$/spiro/Au	13.71	Maintaining 93% of its initial PCE for 300 h/under continuous illumination at the maximum power point	136
	2019	ITO/SnO_2/$CsPbI_2Br$-$Pb(Ac)_2$-CsBr/spiro/Au	15.78	Maintaining 86% of its initial PCE for 1368 h/in N_2 atmosphere	159

	2019	ITO/SnO_2/$CsPbBrI_2$/PTAA/Au	16.58	Maintaining 90% of its initial PCE for 4000h/in air with 20-30% RH	132
	2020	FTO/c-TiO_2/mp-TiO_2/2-ThPy-$CsPbI_2Br$/spiro/Ag	12.69	Maintaining 92% of its initial PCE for 30 days/in air with 40% RH	161
	2020	FTO/SnO_2/PANI-$CsPbBrI_2$/carbon	13.52	Maintaining 80% of its initial PCE for 100 h/in dry air	158
	2020	ITO/SnO_2/PEI-$CsPbI_2Br$/spiro/Au	15.48	Maintaining 81.9% of its initial PCE for 500 h/in air with 15−25% RH	160
	2020	FTO/TiO_2/NSs/$CsPbBrI_2$/NSs/spiro/Au	16.65	Maintaining 91% of its initial PCE for 648 h/in air with 35% RH	157
	2020	FTO/TiO_2/$CaCl_2$-$CsPbBrI_2$/spiro/Au	16.79	Maintaining 90% of its initial PCE for 1080 h/in air with 25% RH	155
	2020	FTO/c-TiO_2/mp-TiO_2/$Cs_{0.99}Rb_{0.01}PbI_2Br$/P3HT/Au	17.16	Maintaining 90% of its initial PCE for 120 h/65 ℃	134
	2021	FTO/bl-TiO_2/Graded $CsPbBr_xI_{3-x}$/PTAA/Au	13.82	Maintaining 90% of its initial PCE for 1000 h/under 1-sun illumination in N_2 atmosphere	153
	2021	ITO/NiO_x/$CsPbI_2Br$:S_8/c-Nb_2O_5/$PC_{61}BM$/Bphen/Ag	14.46	Maintaining 80% of its initial PCE for 24 h/in air with 40−60% RH	162
	2021	ITO/SnO_2/$CsPbBrI_2$/PTAA/Ag	16.02	Maintaining 77.5% of its initial PCE for 768h/in air with 10-20% RH	133
	2021	ITO/ZnO/SnO_2/$CsPbBrI_2$/mixed passivation layer/spiro/Ag	16.7	Maintaining 92% of its initial PCE for 1000 h/in a glovebox	144
	2021	ITO/ZnO/SnO_2/PEACl-KBr-$CsPbI_2Br$/spiro/MoO_3/Ag	16.9	Maintaining 87.5% of its initial PCE for 240 h/in N_2 atmosphere	156

$CsPbI_3$	2014	ITO/PEDOT:PSS /δ-$CsPbI_3$/PCBM/Al	0.09	-	35
	2015	FTO/c-TiO_2/$CsPbI_3$/spiro /Ag	2.9	-	163
	2016	FTO/TiO_2/α-$CsPbI_3$/spiro/Ag	4.13	-	190
	2016	FTO/TiO_2/$CsPbI_3$ QDs/spiro/MoO_x/ Al	10.77	Maintaining 27% of its initial PCE for 2 days/in air with 40−60% RH	38
	2017	FTO/c-TiO_2/b-$CsPbI_3$/carbon	4.65	-	165
	2017	ITO/Ca/C_{60}/$CsPbI_3$/TAPC/TAPC: MoO_3/Ag	9.4	Quickly degraded, assuming a transparent appearance after 336 h, even with an encapsulation	170
	2017	FTO/c-TiO_2/$CsPbI_3$/P3HT/Au	10.5	Maintaining 94% of its initial PCE for 2000 s/at the maximum power point	169
	2017	ITO/PTAA/Sulfobetaine Zwitterions-$CsPb(I_{0.98}Cl_{0.02})_3$ /PCBM/C_{60}/BCP/ Al	11.4	Maintaining 85% of its initial PCE for 30 days/in air	182
	2017	FTO/c-TiO_2/$CsPbI_3$·xEDAPbI_4/spiro/Ag	11.8	Maintaining 90% of its initial PCE for 30 days/in dry air without encapsulation	197
	2017	FTO/c-TiO_2/$CsPb_{0.96}Bi_{0.04}I_3$/CuI/Au	13.21	Maintaining 68% of its initial PCE for 168 h/in air without encapsulation	174
	2017	FTO/TiO_2/AX-$CsPbI_3$ QDs/spiro/MoO_x/ Al	13.43	-	168

	2018	FTO/c-TiO_2/m-TiO_2/m-Al_2O_3/$CsPb_{0.96}Sb_{0.04}I_3$/carbon	5.18	Maintaining 93% of its initial PCE for 37 days/in air with encapsulation	177
	2018	FTO/TiO_2/$CsPbI_3$:xEu/spiro/Au	6.8	-	178
	2018	FTO/c-TiO_2/m-TiO_2/PVP-$CsPbI_3$/spiro/Au	10.74	Maintaining 75% of its initial PCE for 500 h/in air with 45−55% RH	183
	2018	ITO/SnO_2/PEA-$CsPbI_3$/spiro/Au	12.4	Maintaining 93% of its initial PCE for 40 days/in air without encapsulation	184
	2018	FTO/c-TiO_2/mp-TiO_2/$CsPb_{0.95}Ca_{0.05}I_3$/P3HT/Au	13.3	Maintaining 85% of its initial PCE for 2 months/in air with encapsulation	176
	2018	FTO/c-TiO_2/PEAI-$CsPbI_3$/spiro/Ag	13.5	Maintaining 92% of its initial PCE for 200 h/in dry air under continuous illumination	195
	2018	ITO/SnO_2/$CsPbI_3$/spiro/Au	15.7	No significant decay for 500 h/under continuous illumination	164
	2018	FTO/c-TiO_2/PTABr-$CsPbI_3$/spiro/Ag	17.06	Maintaining 91% of its initial PCE for 500 h/in N_2 glovebox	194
	2019	FTO/c-TiO_2/PEG-$CsPbI_3$/spiro/Au/FTO	3.09	No significant decay for 25 days	186
	2019	FTO/bl-TiO_2/Sn doped $CsPbI_3$/CuSCN/Au	5.12	-	180
	2019	FTO/c-TiO_2/m-TiO_2/2% Ca^{2+}-doped $CsPbI_3$/spiro/Au	9.2	Maintaining 80% of its initial PCE for 120 h/in air with 20% RH	175

	2019	FTO/c-TiO_2/m-TiO_2/$CsPbI_3$:Br:InI_3/carbon	12.04	No significant decay for 1500 h/in air with encapsulation	171
	2019	FTO/TiO_2/Ge-$CsPbI_3$/spiro /Ag	12.15	Maintaining 85% of its initial PCE for 90 days/at the maximum power point	173
	2019	FTO/TiO_2/$CsPbI_3$ QDs/PTB7/MoO_3 /Ag	12.55	-	167
	2019	FTO/c-TiO_2/$CEG_{1.0MAI}$C$sPbI_3$/P3HT/Au	14.1	Maintaining 93% of its initial PCE for 30 days/in the dark with 60−70% RH	166
	2019	ITO/SnO_2/nano-ZnO/$Cs_{1.2}PbI_{3.2}$/spiro/MoO_3/Ag	16.39	Maintaining 95% of its initial PCE for 500 h/under continuous illumination	189
	2019	FTO/TiO_2/Pb(SCN)$_2$: 2%-$CsPbI_3$/PTAA/Au	17.04	-	179
	2019	FTO/c-TiO_2/CHI-$CsPbI_3$/spiro/Ag	18.4	Maintaining 92% of its initial PCE for 500 h/under continuous illumination at the maximum power point	68
	2020	FTO/TiO_2/MnI_2-$CsPbI_3$/PTAA/Au	16.52	The stability was significantly improved after introducing Mn^{2+}	181
	2020	FTO/TiO_2/GABr disposed $CsPbI_3$/PTAA/Au	18.02	Maintaining 92% of its initial PCE for 1 month/in air with 20−30% RH	188
	2020	FTO/c-TiO_2/NGBr-$CsPbI_3$/MoO_3/Au	18.27	Maintaining 90% of its initial PCE for 500 h/under continuous illumination	196
	2021	FTO/c-TiO_2/m-TiO_2/$CsPbI_3$/carbon	14.6	No significant decay for 30 days in dry air	191

	2021	FTO/TiO_2/UAT-$CsPbI_3$/spiro/Au	20.0	Maintaining 89% of its initial PCE for 550 h/in air with 20−30% RH	185
	2021	FTO/c-TiO_2/SDMS-$CsPbI_3$/spiro/Au	20.37	Maintaining 90% of its initial PCE for 150 h/under continuous illumination	192

2. All-inorganic metal halide perovskite candidates and their properties

2.1 Crystal and electronic structures

The formation of the perovskite structure (ABX_3, X = Cl, Br, and I) is commonly determined by the Goldschmidt's tolerance factor (*t*):[47,62-63]

$$t = \frac{(R_A + R_B)}{\sqrt{2}(R_B + R_X)}$$

where R_A, R_B, and R_X are the effective ionic radii of A, B, and X ions, respectively. A possible perovskite candidate can be predicted when *t* is in the range from 0.8 to 1.0. When *t* = 1.0, an ideal ABX_3 perovskite structure with a cubic crystal structure will be obtained. When *t* is in the range from 0.9 to 1.0, the perovskite structure is dominant by a cubic phase. When *t* is from 0.8 to 0.9, the perovskite structure will be distorted, and other structures, such as an orthorhombic, tetragonal, and rhombohedral crystal structures, will emerge. It has also been proposed that *t* alone is not sufficient for the prediction of stable perovskite structure, an additional indicator of octahedral factor (μ) is needed,[33,64]

$$\mu = \frac{R_B}{R_X}$$

which means the B site cation must have the appropriate size to be coordinated by six anions and can therefore fit into the octahedral void, the minimum and maximum values of μ are 0.41 and 0.72, respectively. Based on the two factors, theoretical and experimental results identified that inorganic Cs was the best choice for A site to form a stable all-inorganic perovskite structure. Moreover, it is well known that the high photovoltaic performance of the PSC strongly depends on the antibonding character of the valence band maximums of perovskites, which is resulted from the outermost electrons of the lead (Pb) cation hybridizing with the halogen anion p orbitals. Such a perfect structure suggests that Pb is the best choice for B-site.[40-44] Therefore, combining with the requirements of bandgaps, three kinds of IMH perovskites, including $CsPbBr_3$, $CsPb(I_xBr_{1-x})_3$ and $CsPbI_3$, were studied widely previously and will be reviewed in this following part.

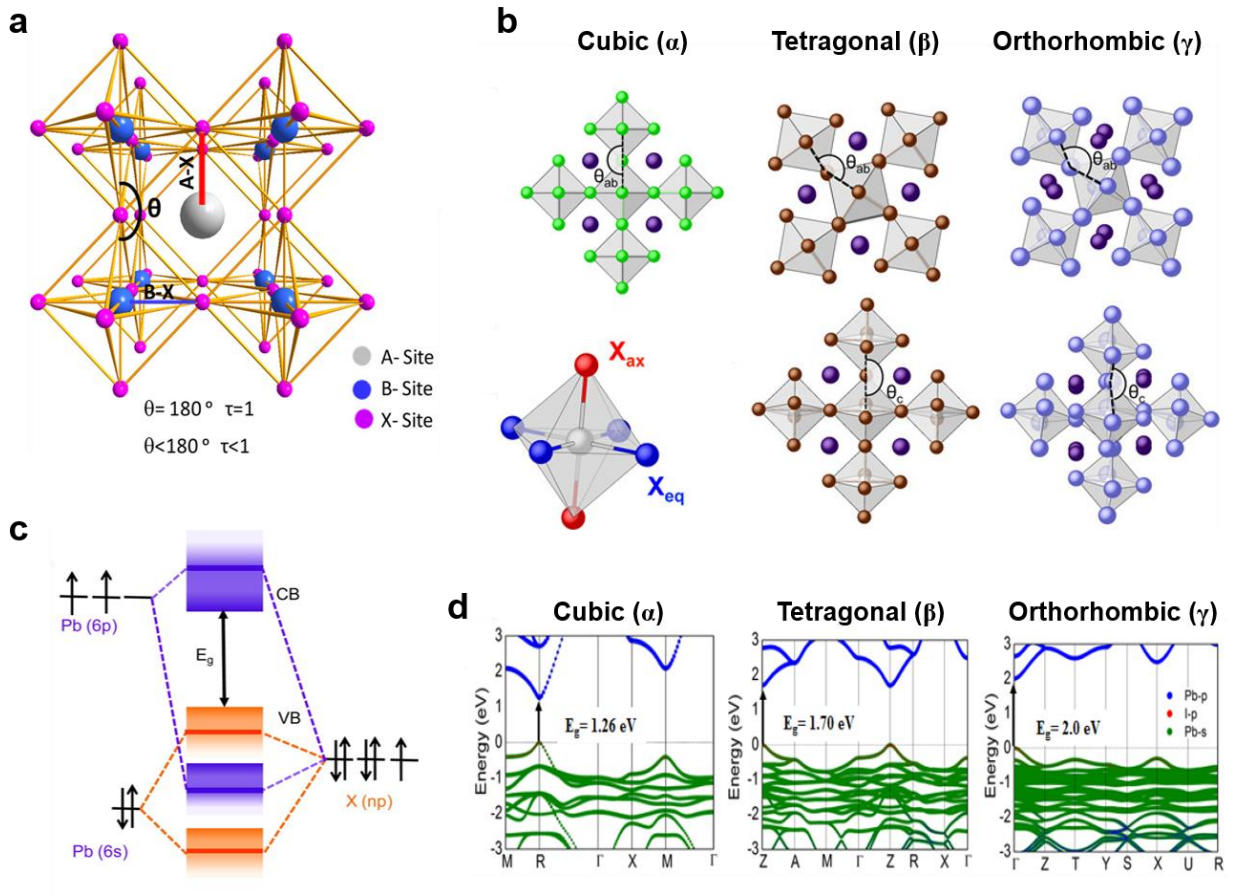

Fig. 1. a, Schematic of the ABX_3 perovskite with the tilting angle (θ), bond length, and Goldschmidt tolerance factor. Reproduced with permission from Dutta *et al.* [65], Copyright (2019) American Chemical Society. **b**, Schematic diagrams of the 3D arrangement of the $[PbX_6]^{4-}$ octahedra in $CsPbX_3$ perovskites with a cubic (α), tetragonal (β), and orthorhombic (γ) structure. Reproduced with permission from Bertolotti *et al.* [66], Copyright (2017) American Chemical Society. **c**, Schematic of the bonding/antibonding orbitals of $CsPbX_3$ showing the formation of the valence band (VB) and conduction band (CB). Reproduced with permission from Ravi *et al.* [67], Copyright (2016) American Chemical Society. **d**, Calculated band structures of the $CsPbI_3$ perovskites with a cubic (α), tetragonal (β), and orthorhombic (γ) structure. Reproduced with permission from Wang *et al.* [68], Copyright (2019) AAAS.

In general, $CsPbX_3$ (X = Br, I, and mixed halides) possesses a characteristic $[PbX_6]^{4-}$ octahedral structure, in which Pb^{2+} and X^- ions form a three-dimensional (3D) network of corner-sharing PbX_6 octahedra, and Cs^+ ions occupy the octahedral voids. Owing to the high flexibility of the $[PbX_6]^{4-}$ octahedral structure, $CsPbX_3$ has four types of crystal polymorphs, including cubic structure (α-, *Pm*3*m*), tetragonal structure (β-, *P*4/*mbm*), orthorhombic structure (γ-, *Pbnm*), and non-perovskite structure (δ-, *Pnma*). These four types of crystal polymorphs can be transferred between one another by tilting the octahedra, implying bending of the Pb-X-Pb angle from the ideal 180° value (**Fig. 1a**).[65] $CsPbI_3$ has an obvious difference among the four crystal polymorphs because of its large radius of iodine. Here, we therefore use $CsPbI_3$ as an example. At

room temperature, $CsPbI_3$ exhibits the non-perovskite δ-phase with Pb-I-Pb bond angles of 95.9° and 91.4°, which has a large bandgap of nearly 3.0 eV and is relatively inactive as a photovoltaic absorber, which will not be discussed in this review. Besides, $CsPbI_3$ has three kinds of black phases when the temperature rises from room temperature to the melting point, including α-, β-, and γ-phases, as shown in **Fig. 1b**.[66] Among them, α-phase has the highest symmetry with a cubic structure, and its Pb-I-Pb bond angle is an ideal 180° value with an undistorted lead iodide octahedra. Transitions from the α-phase to the lower symmetry modifications (β- and γ-phases) are observed progressively upon cooling. On the one hand, β-phase $CsPbI_3$ will be generated when a tetragonal distortion is applied on the ideal cubic structure, which shows out-of-plane tilting of the polyhedral along the *c*-axis, adopting the tetragonal space group. On the other hand, performing a second distortion on the α-phase $CsPbI_3$ will generate γ-phase $CsPbI_3$, which is another metastable perovskite phase with an orthorhombic structure.

Besides the crystal structure, the electronic structure of $CsPbX_3$ is also very important for its application in PSCs. The electronic structures of $CsPbX_3$ with different halides have been predicted by the density functional theory (DFT) calculations, which showed the similar features, as shown in **Fig. 1c**.[67] The conduction band minimum (CBM) consists of antibonding mixing of Pb 6p and X *n*p orbitals with dominant contributions from Pb 6p, while the valence band maximum (VBM) is mainly determined by antibonding hybridized Pb 6s and X *n*p orbitals with the major contribution from X np. Meanwhile, it has been demonstrated that the Cs^+ has little effect on the electronic structure near the band edge, although it can affect the electronic structure indirectly by tilting the $[PbX_6]^{4-}$ octahedra when it is replaced by other cations. In order to echo with **Fig. 1b**, here, we also use $CsPbI_3$ as an example. **Fig. 1d** shows the band structures of α-, β-, and γ-phase $CsPbI_3$ perovskites, which reveal that all of them have direct bandgaps, suggesting their potential applications in PSCs.[68] Moreover, the relative trend of the bandgap was calculated by the self-consistent GW approach, which yielded a gradually increasing trend with the values of 1.26, 1.70, and 2.0 eV for the α-, β-, and γ-phase $CsPbI_3$ perovskites, respectively. This trend has already been demonstrated experimentally. For γ-phase $CsPbI_3$, the band edge emission was around 700 nm based on the photoluminescence (PL) spectra, which agreed with the bandgap of 1.73 eV.[54-56] For β-phase $CsPbI_3$, it showed an absorption edge of ~ 736 nm with a bandgap of 1.68 eV based on a Tauc plot.[68] For α-phase $CsPbI_3$, there is no experimental report till now because of its phase instability at room temperature.

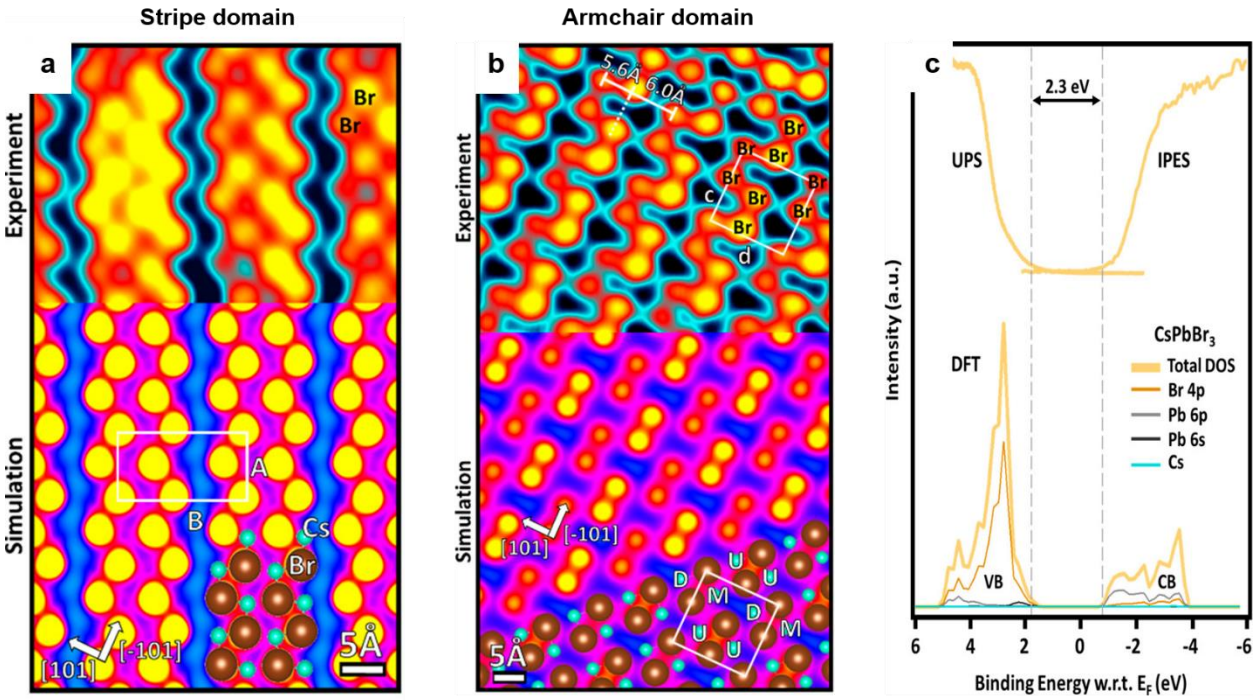

Fig. 2. Experimental STM images and simulated models of $CsPbBr_3$ with **a**, stripe domain and **b**, armchair domain. **c**, Experimental UPS-IPES spectra and calculated PDOS of the $CsPbBr_3$. Reproduced with permission from Hieulle *et al.* [69], Copyright (2020) American Chemical Society.

Recently, the atomic and electronic structures of $CsPbBr_3$ perovskites were also studied systemically by Hieulle and coworkers.[69] They first used the scanning tunneling microscopy (STM) to characterize the atomic structure of the $CsPbBr_3$ perovskite film on Au(111). Two different arrangements of Br anions, including the stripe domain and the armchair domain, were found, which originated from a complex interplay between Cs cations and Br anions (**Fig. 2a-b**). Further studies on the two kinds of domains were performed by scanning tunneling spectra (STS) and differential conductance (dI/dV) and the results revealed relatively similar electronic properties between them. Moreover, the electronic structure of the $CsPbBr_3$ perovskite was also studied by ultraviolet and inverse photoelectron spectroscopy (UPS-IPES), which showed the same result with previous literature and their DFT calculations, as shown in **Fig. 2c**. In short, this work first reported the band structure of the $CsPbBr_3$ perovskite based on its precise surface atomic structure obtained by STM, which may lead to a better prediction of interfacial properties of the $CsPbBr_3$ perovskite and a new way for the PSC engineering.

2.2 Photovoltaic properties

Except for the crystal structure and electronic structure, it is also necessary to provide a brief review on the photovoltaic properties of $CsPbX_3$ to help us understand their applications in PSCs, like carrier lifetime, carrier mobility, carrier diffusion length, mobility-lifetime product, electron-hole recombination rate and so on.

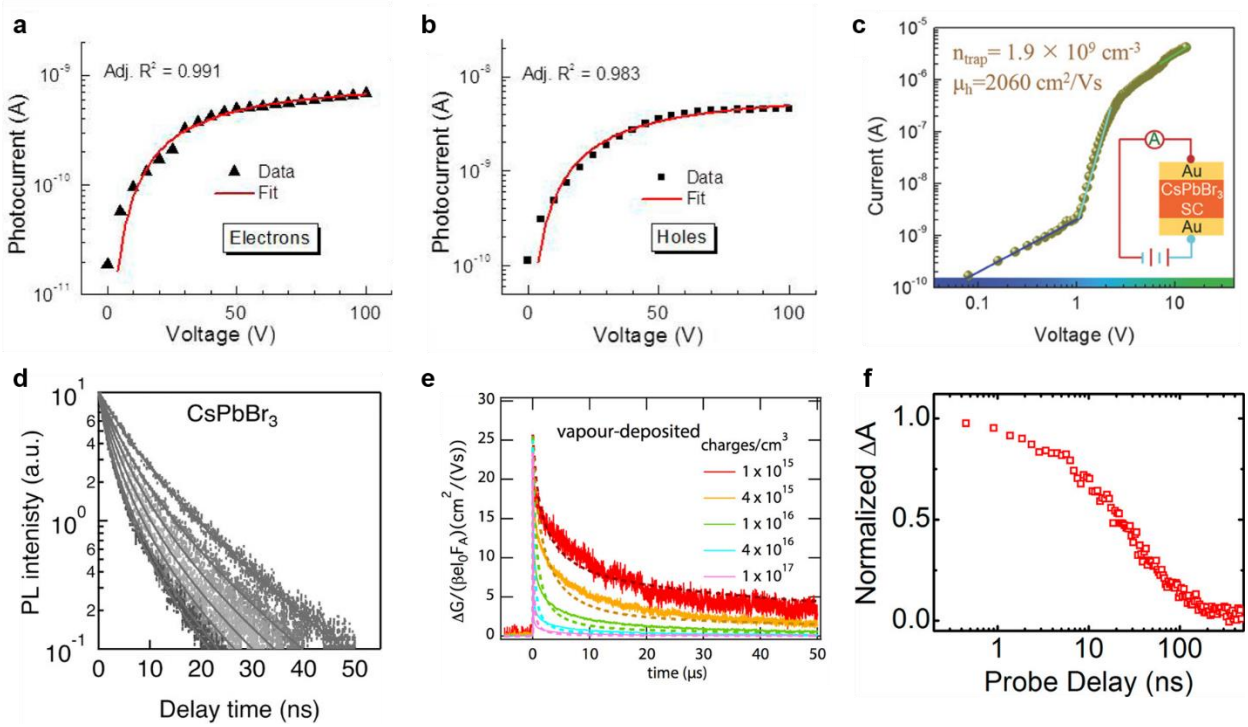

Fig. 3. Photoconductivity data from the samples of $CsPbBr_3$ for **a**, electrons and **b**, holes. The fitting of the data is based on the Many equation. Reproduced with permission from Stoumpos *et al.* [70], Copyright (2013) American Chemical Society. **c**, Current–voltage (*I–V*) curve of a hole-only device based on $CsPbBr_3$. The inset shows the device structure of the hole-only device. Reproduced with permission from Song *et al.* [71], Copyright (2017) Wiley-VCH Verlag GmbH & Co. KGaA, Weinheim. **d**, Time-resolved PL decay kinetics of the $CsPbBr_3$ single-crystal microplates at different excited carrier densities. Reproduced with permission from Zhu *et al.* [72], Copyright (2017) Wiley-VCH Verlag GmbH & Co. KGaA, Weinheim. **e**, time-resolved microwave conductivity traces for a vapor-deposited $CsPbI_3$ thin film with thickness of 260 nm. Reproduced with permission from Hutter *et al.* [73], Copyright (2017) American Chemical Society. **f**, Transient absorption dynamics of the band edge bleach feature for $CsPbI_3$. Reproduced with permission from Dastidar *et al.* [74], Copyright (2017) American Chemical Society.

In 2013, Stoumpos *et al.* prepared the $CsPbBr_3$ single crystal ingots by the vertical Bridgman method and the electron lifetime and mobility were demonstrated to be ~2.5 μs and 1000 $cm^2\ V^{-1}\ s^{-1}$, respectively. The mobility-lifetime products for electrons and holes in $CsPbBr_3$ single crystal ingots were also estimated by the photoconductivity measurements and the values were determined to be 1.7×10^{-3} cm^2/V and 1.3×10^{-3} cm^2/V, respectively (**Fig. 3a-b**).[70] Later, Song and coworkers also fabricated the $CsPbBr_3$ single crystal ingots by a modified vertical Bridgman method. They obtained the carrier mobility value of ~2000 $cm^2\ V^{-1}\ s^{-1}$, and also characterized other photovoltaic properties. For example, the $CsPbBr_3$ single crystal showed a large diffusion length of more than 10 μm, a high visible absorbance coefficient of about 10^5 cm^{-1} and a low trap-state density of 1.2×10^9 cm^{-3} (**Fig. 3c**). Furthermore, they fabricated a photodetector based on the $CsPbBr_3$ single crystal, which exhibited high light on/off ratio of more than 10^3.[71] In 2017, Zhu and coworkers synthesized $CsPbBr_3$ microplates and demonstrated that $CsPbBr_3$ had the same

chance with $MAPbBr_3$ and $FAPbBr_3$ in the application of photovoltaic devices, because it showed low carrier trapping rate constants (~10^7 s^{-1}), low surface recombination velocities (~10^3 cm s^{-1}), low electron-hole radiative recombination rate constants (~10^{-10} cm^3 s^{-1}), and modest carrier mobilities on the order of tens of cm^2 V^{-1} s^{-1} (**Fig. 3d**).[72]

Besides $CsPbBr_3$ perovskites, the photovoltaic properties of $CsPbI_3$ and $CsPb(I_xBr_{1-x})_3$ perovskites were also studied in the last few years. For example, Hutter *et al.* prepared $CsPbI_3$ films by the vapor deposition method, which showed the charge carrier mobility of around 25 cm^2 V^{-1} s^{-1} and the charge carrier lifetime of several μs (**Fig. 3e**). Moreover, by fitting the experimental time resolved microwave conductivity (TRMC) data to a kinetic model, the second-order recombination rate constant was determined to be 1.3 × 10^{-10} cm^3 s^{-1}.[73] Using pump-probe time-resolved terahertz spectroscopy (TRTS), Dastidar *et al.* investigated the carrier mobility and recombination kinetics of the solution-processed $CsPbI_3$ perovskite film (**Fig. 3f**).[74] By fitting the data with a kinetic model combining diffusion and recombination, a bimolecular recombination rate of 10^{-10} cm^3 s^{-1} and a charge carrier mobility > 30 cm^2 V^{-1} s^{-1} were determined. Moreover, the diffusion length for $CsPbI_3$ was estimated to be 1 μm in this work. For $CsPb(I_xBr_{1-x})_3$ perovskites, Kennedy *et al.* also measured the recombination dynamics and transport properties of individual $CsPbI_2Br$ microcrystals by ultrafast pump-probe microscopy.[75] By global fitting of power-dependent kineties, the carrier lifetime and mobility were determined to be ~1 ns and 10 cm^2 V^{-1} s^{-1}, respectively.

In short, for the carrier mobility, because the excitation and recombination of electrons and excitons were confined within the $[PbX_6]^{4-}$ octahedra,[76] it seems that the carrier mobility values of $CsPbX_3$ were similar and can be comparable with those of the corresponding hybrid ones. For the carrier lifetime, it relies on the film quality, which depends on the fabrication method. As a result, the carrier lifetime varies for $CsPbX_3$ perovskites fabricated by different methods. This can also be demonstrated indirectly by the example that the single crystals of $CsPbX_3$ showed higher values than the polycrystalline films. For the carrier diffusion length, most of them were on the order of 1 μm, which was much larger than the corresponding hybrid ones. Overall, the photovoltaic properties of $CsPbX_3$ perovskites indicate that $CsPbX_3$ perovskites are potentially good light absorbers for the applications in PSCs.

3. All-inorganic metal halide perovskite solar cells (IMH-PSCs)

As mentioned above, typical IMH perovskites include $CsPbBr_3$, $CsPb(I_xBr_{1-x})_3$ and $CsPbI_3$. In this section, we give a detailed discussion on their applications in PSCs. According to their bandgaps, we first review $CsPbBr_3$-based IMH-PSCs, mainly focusing on some effective strategies to improve their power conversion efficiencies (PCEs). Then we discuss $CsPb(I_xBr_{1-x})_3$-based IMH-PSCs, including $CsPbIBr_2$- and $CsPbI_2Br$-based IMH-PSCs. Finally, we review $CsPbI_3$-based IMH-PSCs in terms of enhancing their stability and PCEs at the same time.

3.1 $CsPbBr_3$-based IMH-PSCs

$CsPbBr_3$ has a wide bandgap of 2.3 eV, indicating that it can absorb the wavelength below 540 nm. This bandgap is a bit too high for its application in the PSC, however, $CsPbBr_3$ exhibits an excellent stability among all kinds of perovskites so far. Therefore, it is useful for us to study

$CsPbBr_3$-based IMH-PSCs, from which we can study the approaches to improving photovoltaic performances of PSCs carefully because they are less influenced by the stability of perovskites. Moreover, we can use it into the tandem devices by introducing some iodine into $CsPbBr_3$ as discussed in the next subsection. Thus, in this subsection, we mainly focus on the effective and promising methods to enhance PCEs of $CsPbBr_3$-based IMH-PSCs.

In 2015, Kulbak *et al.* first employed $CsPbBr_3$ into PSCs successfully, in which they prepared the $CsPbBr_3$ film by a two-step method.[77] In order to obtain a high PCE and open-circuit voltage (V_{OC}), they fabricated various PSC architectures with different electron transport materials (ETMs), including mesoporous (mp)-TiO_2, mp-Al_2O_3, and without mp-layer, and distinct hole transport materials (HTMs), including spiro-OMeTAD, poly[bis(4-phenyl)(2,4,6-trimethylphenyl)amine] (PTAA), and 4,4′-bis(N-carbazolyl)-1,1′-biphenyl (CBP), respectively. As a result, the $CsPbBr_3$-based IMH-PSCs with the structure of FTO/mp-TiO_2/$CsPbBr_3$/PTAA/Au showed the highest PCE of 5.95% with a large V_{OC} of 1.28 eV. In order to illustrate the good stability of $CsPbBr_3$-based IMH-PSCs, Kulbak *et al.* compared $MAPbBr_3$ and $CsPbBr_3$ directly in another work.[78] They first prepared the two kinds of perovskites using the same method and compared their thermal stability by thermogravimetric analysis (TGA). The result showed that $CsPbBr_3$ had a high temperature tolerance of 580 ℃, which was much higher than that of $MAPbBr_3$. Then they employed the two kinds of perovskites into PSCs with the same structure and compared their photovoltaic stability. As a result, the PCE of the $CsPbBr_3$-based IMH-PSC was slightly lower than that of the $MAPbBr_3$-based PSC, while the former exhibited much better stability than the latter. Finally, the stability of the two kinds of PSCs was tested under the electron beam, which also showed that the $CsPbBr_3$-based IMH-PSC had a better stability than the $MAPbBr_3$-based PSC. These results indicated that $CsPbBr_3$ as a stable light absorber was promising.

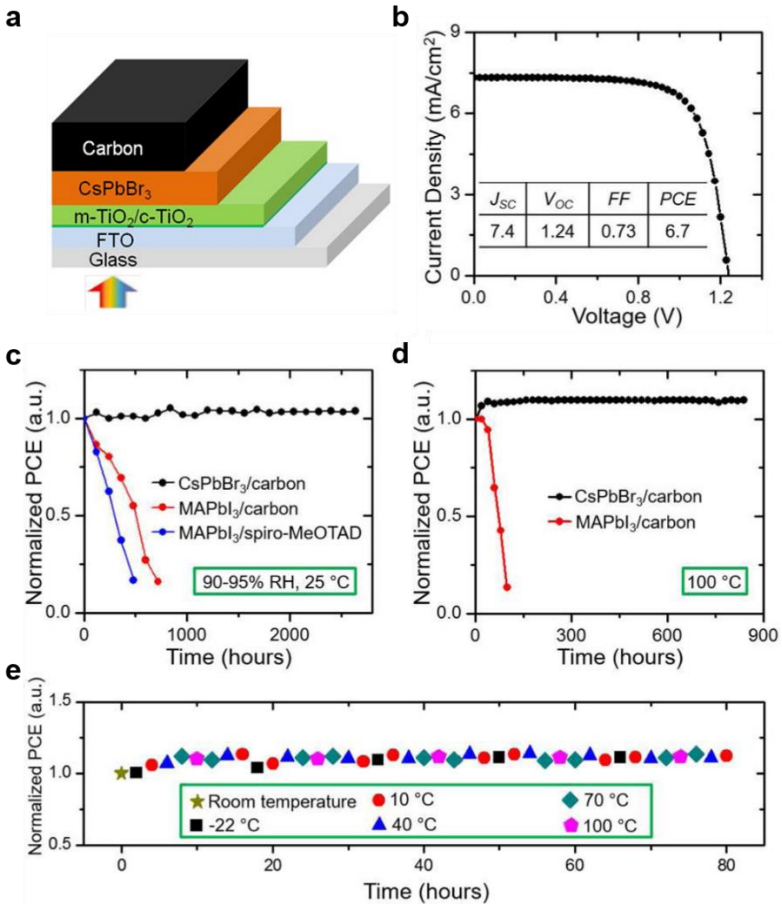

Fig. 4. a, Schematic diagram of the $CsPbBr_3$-based IMH-PSC with the carbon electrode. **b**, The champion *J*–*V* plot of the $CsPbBr_3$-based IMH-PSC with the carbon electrode. The inset shows corresponding photovoltaic parameters. Normalized PCEs of the $CsPbBr_3$-based IMH-PSCs with carbon electrodes, the $MAPbBr_3$-based PSCs with carbon electrodes and the $MAPbBr_3$-based PSCs with spiro-MeOTAD and Au electrode as a function of storage time under **c**, humid air (90–95% RH, 25 °C), **d**, high temperature (100 °C), and **e**, cycled temperature (-22 °C to 100 °C). Reproduced with permission from Liang *et al.* [84], Copyright (2016) American Chemical Society.

The two works proposed by Kulbak *et al.* opened a way for enhancing the stability of the PSC dramatically, however, the structures of PSCs still contained organic HTMs and noble metal electrodes, which increased the cost of PSCs. Moreover, some organic additives in commonly used HTMs, such as lithium bis(trifluoromethanesulfonyl)imide (LiTFSI) and tert-butylpyridine (tBP), are also hygroscopic and deliquescent, which accelerates the PSC degradation.[79-83] In order to resolve these shortcomings, Liang and coworkers proposed $CsPbBr_3$-based IMH-PSCs with carbon electrodes, as shown in **Fig. 4a**.[84-85] In this structure, low-cost carbon electrodes with high conductivity, stability, and processability were used to replace both instable organic HTMs and expensive noble metal electrodes for hole collection, as it had a proper work function compared with Au. A PCE of 6.7% and a V_{OC} of 1.24 eV were reported (**Fig. 4b**). The stability of the $CsPbBr_3$-based IMH-PSCs with carbon electrodes was also demonstrated to be excellent under different harsh conditions, such as high humidity, high temperature, low temperature, and a cycled

temperature (-22 ℃ to 100 ℃), as shown in **Fig. 4c-e**. Moreover, a $CsPbBr_3$-based IMH-PSC with a large active area (1.2 cm^2) was also fabricated, which showed a minor hysteresis and a PCE of 5.0%.

Considering that the bandgap of $CsPbBr_3$ is 2.3 eV, the PCE of ~7% is still far from its theoretical limit. Till now, three categories of effective strategies for boosting photovoltaic performances of $CsPbBr_3$-based IMH-PSCs were put forward according to previous literature: (1) developing novel preparation methods to enhance the quality of the $CsPbBr_3$ perovskite film; (2) doping the $CsPbBr_3$ perovskite with heteroatoms to enhance the quality of the $CsPbBr_3$ perovskite film; (3) optimizing the architecture of $CsPbBr_3$-based IMH-PSC to facilitate carrier transport.

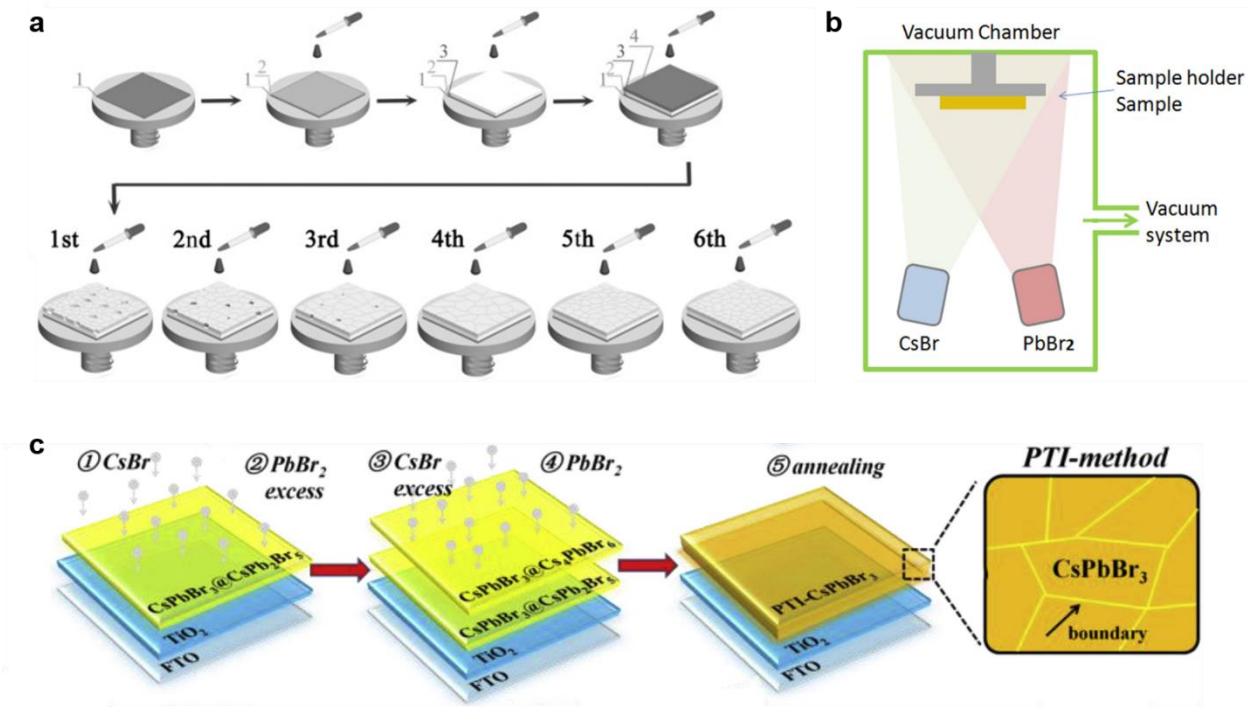

Fig. 5. a, Schematic diagram of the deposition process on 1) FTO with 2) compact-TiO_2, 3) mesoporous-TiO_2, and 4) $PbBr_2$, and the multistep solution-processed deposition of CsBr. Reproduced with permission from Duan *et al.* [90], Copyright (2018) Wiley-VCH Verlag GmbH & Co. KGaA, Weinheim. **b**, Schematic diagram of the dual-source coevaporation. Reproduced with permission from Lei *et al.* [98], Copyright (2018) Elsevier. **c**, Schematic diagram of the PTI method to produce $CsPbBr_3$ films. Reproduced with permission from Tong *et al.* [100], Copyright (2019) Elsevier.

The quality of the perovskite film is important for the photovoltaic performance of the PSC.[86-89] For example, a large number of defects at the interfaces and grain boundaries usually act as charge recombination centers in PSCs, which lead to a poor performance. Moreover, in $CsPbBr_3$-based IMH-PSCs, a high temperature is necessary to anneal $CsPbBr_3$, and the high temperature will result in poor crystallinity with uneven crystal sizes, pinholes, and large traps, which will further weaken their photovoltaic performances. Therefore, it is necessary to improve the quality of the $CsPbBr_3$ film, such as reducing its defects and pinholes, increasing its crystallinity. Till now,

several approaches have been put forward. Duan and coworkers developed a multi-step solution-processing method to convert $PbBr_2$ into $CsPbBr_3$ by spin coating the CsBr solution onto $PbBr_2$ in several steps, as shown in **Fig. 5a**.[90] By tuning the number of deposition cycles (*n*) of the CsBr solution, $n = 4$ was demonstrated to be the ideal cycle, which gave a good $CsPbBr_3$ film with large size and without pinholes. As a result, a PCE of 7.54% and a V_{OC} of 1.308 V were obtained. Vacuum thermal evaporation is a mature technique used in the coating industry that can easily deposit multiple layers of thin films with large areas, good uniformity and flatness.[91-97] Therefore, Lei *et al.* put forward vacuum thermal evaporation deposition of $CsPbBr_3$ films by dual-source coevaporation of CsBr and $PbBr_2$ powder (**Fig. 5b**).[98] By controlling the evaporation rate ratio of CsBr and $PbBr_2$, high-quality $CsPbBr_3$ films with good crystallinity and uniformity were obtained. Finally, the $CsPbBr_3$-based IMH-PSC showed a PCE of 6.95%. By optimizing the dual-source thermal deposition method, Zhang *et al.* developed a multiple sequential vacuum deposition method for the preparation of $CsPbBr_3$ film, in which CsBr and $PbBr_2$ were successfully deposited on the substrate with desired thicknesses, and followed by transformation into $CsPbBr_3$ films by an annealing procedure.[99] Meanwhile, by controlling the relative humidity at 30% during the annealing process, a high-quality $CsPbBr_3$ film with pure phase and large grain size could be achieved by this method. By employing it into the PSC with the structure of FTO/c-TiO_2/$CsPbBr_3$/carbon, a PCE of 8.86% was obtained. **Fig. 5c** displays a phase transition induced (PTI) method proposed by Tong and coworkers, which produced high quality $CsPbBr_3$ films by utilizing the derivative phases as nucleation sites to slow down the formation of $CsPbBr_3$ grains and release the stress concentration.[100] Based on this approach, the $CsPbBr_3$ films displayed large grain sizes, good uniformity, high crystallinity, reduced trap densities, and low surface potential barriers between the crystals and grain boundaries. As a result, the $CsPbBr_3$-based IMH-PSC with the carbon electrode showed the PCE as high as 9.86%. Moreover, the $CsPbBr_3$-based IMH-PSC with a n-i-p structure displayed a breakthrough PCE of 10.91%. In short, it is an effective strategy to boost the photovoltaic performance of the $CsPbBr_3$-based IMH-PSC by developing novel preparation methods for $CsPbBr_3$ films.

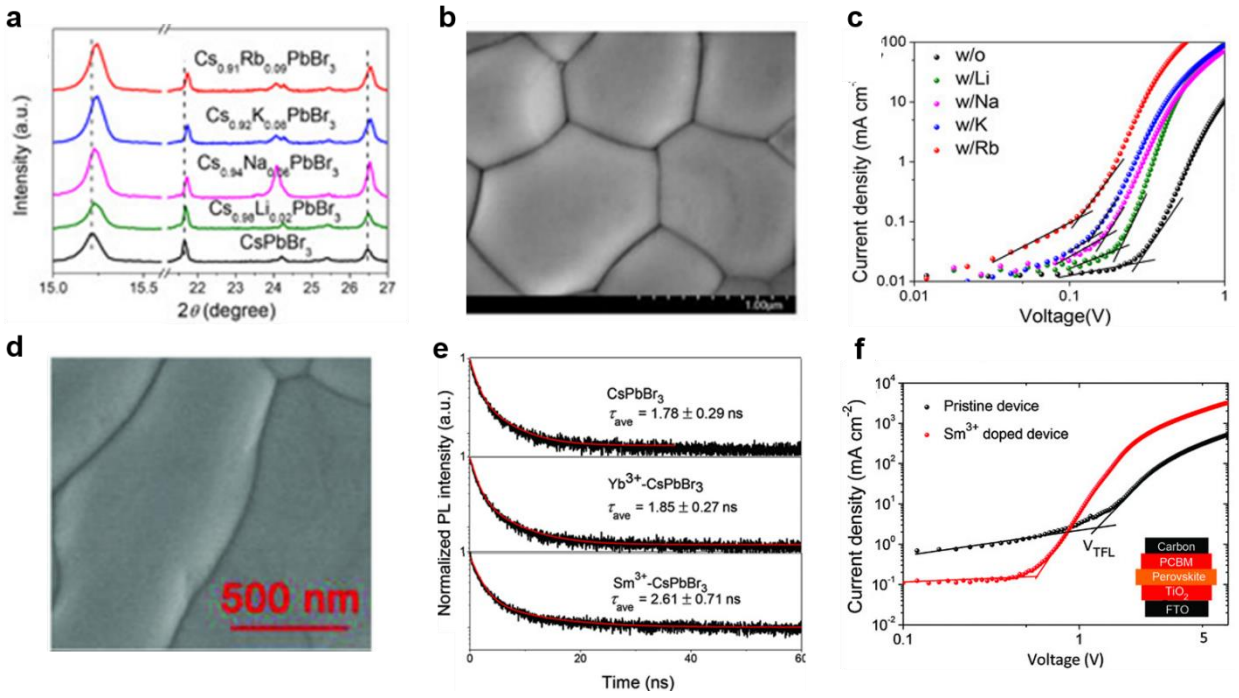

Fig. 6. a, The enlarged comparison of (100), (110), and (111) diffraction peaks of $CsPbBr_3$ with and without alkali metal ions. **b**, Typical scanning electron microscopy (SEM) image of $Cs_{0.91}Rb_{0.09}PbBr_3$. **c**, *J-V* curves under dark conditions for the hole-only devices based on $CsPbBr_3$ with and without alkali metal ions. Reproduced with permission from Li *et al.* [106], Copyright (2018) Wiley-VCH Verlag GmbH & Co. KGaA, Weinheim. **d**, Typical SEM image of $CsPb_{0.97}Sm_{0.03}Br_3$. **e**, Time-resolved PL curves of $CsPbBr_3$ with and without Yb^{3+}/Sm^{3+} ions. **f**, *J-V* curves under dark conditions for the hole-only devices based on $CsPbBr_3$ with and without Sm^{3+} ions. Reproduced with permission from Duan *et al.* [107], Copyright (2018) Wiley-VCH Verlag GmbH & Co. KGaA, Weinheim.

Recently, the incorporation of a handful of additives into perovskites has also emerged as an effective strategy to realize high-quality perovskite films, as these additives may passivate their defects, enhance their stability, and tune their band structures.[101-104] In this fashion, three kinds of partial substitutions can be adopted in $CsPbBr_3$ perovskites, including Cs-site substitution, Pb-site substitution, and Br-site substitution. The Br-site substitution will be discussed in the next subsection because it will lead to a big change in the bandgap. Therefore, we just discuss the other two kinds of substitutions here. In OMH-PSCs, various alkali metal ions were incorporated into A-sites of OMH perovskites to modulate their crystal structure.[105] The results showed enhanced PCEs, which can be ascribed to the larger grain sizes, smaller non-radiative losses, and stronger grain boundary passivation. Motivated by these works, Li *et al.* tried to introduce alkali metal cations into $CsPbBr_3$ perovskites to passivate its charge-carrier trapping.[106] According to X-ray diffusion (XRD) characterization, the introduced alkali metal cations led to a contracted lattice volume for the new IMH perovskites, which was beneficial for its application in the PSC (**Fig. 6a**). Moreover, the grain size became large when alkali metal cations were incorporated into $CsPbBr_3$ films, which could reduce the grain boundaries, maximize charge transportation kinetics, minimize

non-radiative recombination rate and enhance radiative recombination rate, as shown in **Figs. 6b-c**. As a result, a PCE up to 9.86% was achieved for $Cs_{0.91}Rb_{0.09}PbBr_3$-based IMH-PSCs with carbon electrodes. Except for incorporation dopants into A-site, introducing dopants into B-site could achieve the similar function. In the same group, Duan *et al.* introduced lanthanide ions into $CsPbBr_3$ film through the multistep solution-processed method.[107] Through systematic characterizations, the incorporation of Ln^{3+} ions also increased the grain size of the $CsPbBr_3$ film, prolonged the carrier lifetime and reduced charge recombination rate, as shown in **Fig. 6d-f**. Therefore, the results showed the $CsPb_{0.97}Sm_{0.03}Br_3$-based IMH-PSC with the structure of FTO/c-TiO_2/m-TiO_2/$CsPb_{0.97}Sm_{0.03}Br_3$/carbon gave a PCE as high as 10.14% with an ultrahigh V_{OC} of 1.594 V.

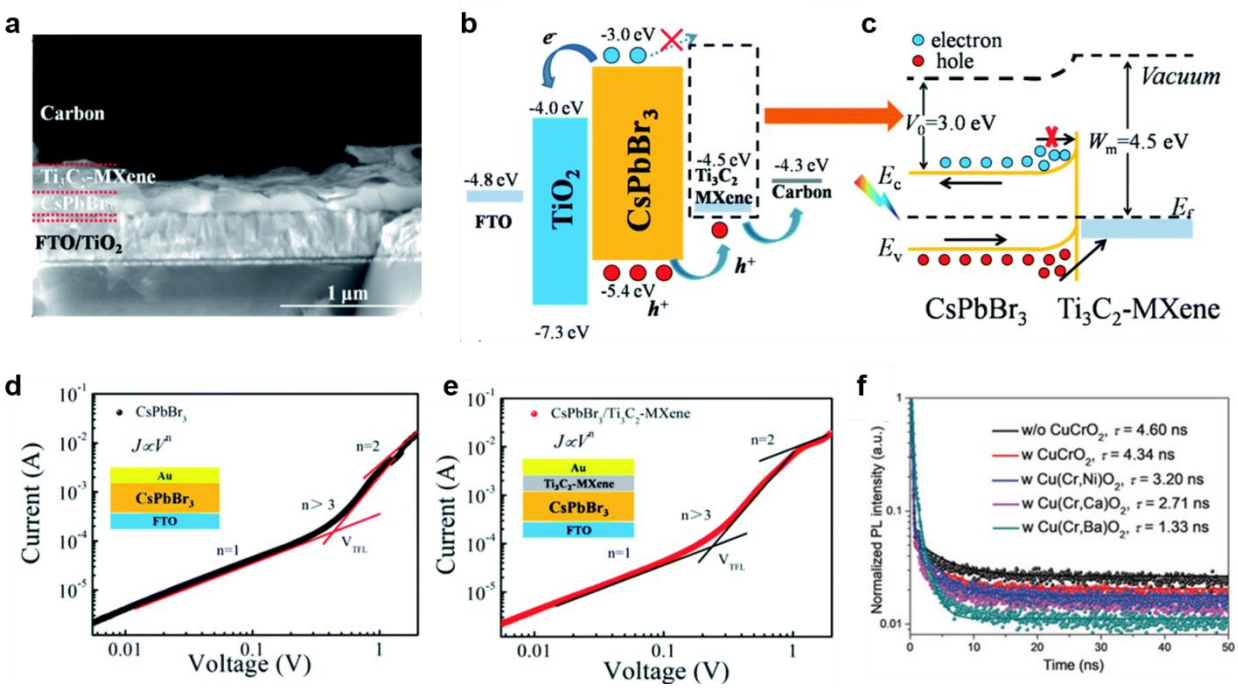

Fig. 7. a, Typical cross-sectional SEM image of the IMH-PSC with the structure of FTO/TiO_2/$CsPbBr_3$/Ti_3C_2-MXene/carbon. **b**, Energy alignment of the IMH-PSC in **a**. **c**, Carrier transport mechanism of the IMH-PSC in **a**. *J–V* curves of devices with FTO/$CsPbBr_3$/Au configuration **d**, without and **e**, with Ti_3C_2-MXene. Reproduced with permission from Tong *et al.* [108], Copyright (2018) The Royal Society of Chemistry. **f**, Time-resolved PL spectra of $CsPbBr_3$ films with and without the $Cu(Cr,M)O_2$ layer. Reproduced with permission from Duan *et al.* [109], Copyright (2019) Wiley-VCH Verlag GmbH & Co. KGaA, Weinheim.

Although much progress has been achieved by developing new preparation methods for $CsPbBr_3$ or doping $CsPbBr_3$ perovskites with heteroatoms, there are still some issues to be resolved in $CsPbBr_3$-based IMH-PSCs with carbon electrodes. One of the typical issues is the interface between $CsPbBr_3$ perovskites and carbon electrodes, which has large recombination and energy level mismatch, impeding the hole transfer in PSCs. In order to reduce the energy difference, inorganic HTMs were proposed in recent years, which facilitated hole transfer from $CsPbBr_3$ perovskites to carbon electrodes. In this respect, Chen *et al*. fabricated Ti_3C_2-MXene nanosheets

by exfoliation of raw Ti_3AlC_2 powder with a HF solution, and employed them into $CsPbBr_3$-based IMH-PSCs with carbon electrodes as efficient HTMs, as shown in **Fig. 7a**.[108] The improved work function alignment ensured a lower energy barrier between the $CsPbBr_3$ film and the carbon electrode (**Fig. 7b-c**), suggesting that the Ti_3C_2-MXene layer could effectively extract hole carriers from the $CsPbBr_3$ film and transport them to the counter electrode simultaneously (**Fig. 7d-e**). As a result, the $CsPbBr_3$-based IMH-PSC with the structure of FTO/TiO_2/$CsPbBr_3$/Ti_3C_2-MXene/carbon showed a PCE as high as 9.01%. For the same purpose, Duan and coworkers also fabricated another HTM of Cu(Cr,M)O_2 (Mg^{2+}, Ni^{2+}, Zn^{2+}, and Fe^{3+}) nanocrystals.[109] By tuning the VBMs of Cu(Cr,M)O_2 nanocrystals, the optimal $CsPbBr_3$-based IMH-PSC with the structure of FTO/TiO_2/$CsPbBr_3$/Cu(Cr,Ba)O_2/carbon achieved a PCE of 10.18%. Such a good performance can be ascribed to the bridged energy alignment from perovskite to Cu(Cr,Ba)O_2, as shown in **Fig. 7f**. Except for the two typical HTM layers, other HTM layers were also introduced in the $CsPbBr_3$-based IMH-PSCs with carbon electrodes, such as MnS layer, $CsMBr_3$ (M = Sn, Bi, Cu) layer, etc.[110-111] All of them showed enhanced PCEs, indicating that it is indeed an effective strategy to boost the photovoltaic performance of the $CsPbBr_3$-based IMH-PSC by introducing a HTM layer between the $CsPbBr_3$ film and the carbon electrode.

In the end of this section, we list a summary of the $CsPbBr_3$-based IMH-PSCs reported in the literature in **Table 1**.[77-78,84,90,98-100,106-117] Overall, the $CsPbBr_3$-based IMH-PSCs showed low PCEs because of the wide bandgap of $CsPbBr_3$. However, this kind of PSCs exhibited good stability among all kinds of PSCs so far. Moreover, the theoretical efficiency limit of the $CsPbBr_3$-based IMH-PSC is around 16.5%, indicating that there is still a lot of room for us to improve its PCE in the future.

3.2 $CsPb(Br_xI_{1-x})_3$-based IMH-PSCs

As mentioned above, the biggest shortcoming for $CsPbBr_3$ is the large bandgap, which limits its wide applications. Therefore, reducing the bandgap of $CsPbBr_3$ is a primary task to boost the PCEs of IMH-PSCs. As mentioned in Section 2.1, the VBM of the $CsPbX_3$ is mainly determined by the orbitals of X *n*p. Therefore, changing the composition of X-site is one of the most effective approaches to adjust the bandgap of $CsPbBr_3$. Till now, two typical mixed halide IMH perovskites of $CsPbBr_2I$ and $CsPbBrI_2$ have been studied widely.

3.2.1 $CsPbBr_2I$-based IMH-PSCs

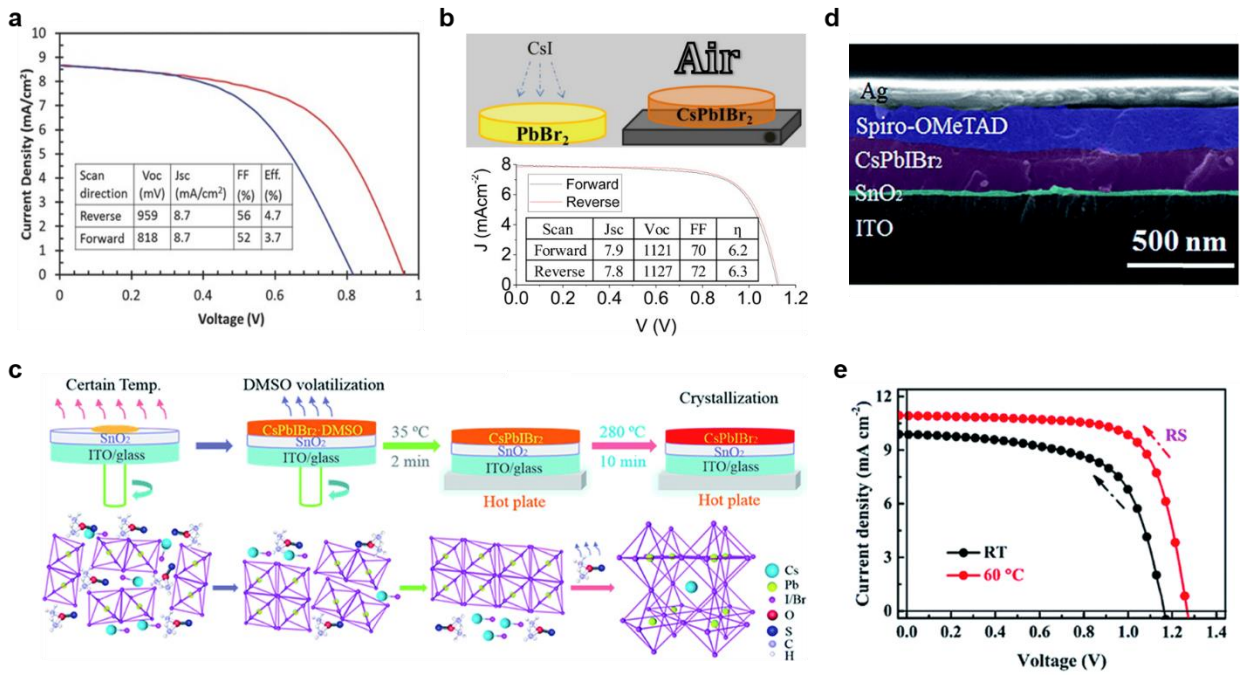

Fig. 8. a, *J–V* curves of the $CsPbBr_2I$-based IMH-PSC with the structure of FTO/c-TiO_2/ $CsPbBr_2I$/Au under reverse and forward scan, respectively. Reproduced with permission from Ma *et al.* [119], Copyright (2016) Wiley-VCH Verlag GmbH & Co. KGaA, Weinheim. **b**, Top: schematic diagram of the spray-assisted solution-processed method; Bottom: *J–V* curves of the $CsPbBr_2I$-based IMH-PSC under reverse and forward scan, respectively. Reproduced with permission from Ma *et al.* [120], Copyright (2016) American Chemical Society **c**, Schematic diagram of the preheating-assisted one-step spin-coating method. **d**, Typical cross-sectional SEM image of the $CsPbBr_2I$-based IMH-PSC with the structure of ITO/SnO_2/$CsPbIBr_2$/spiro-OMeTAD/Ag. **e**, *J–V* curves of the $CsPbBr_2I$-based IMH-PSC with different substrate temperature. Reproduced with permission from Ma *et al.* [121], Copyright (2019) The Royal Society of Chemistry.

Replacing 1/3 bromide in $CsPbBr_3$ by iodine will form $CsPbBr_2I$, which has a reduced bandgap of ~2.0 eV, indicating a promising potential in the application of three-junction tandem cells.[118] Moreover, $CsPbBr_2I$ takes after the good stability of $CsPbBr_3$ and can maintain stability up to its melting point, which is more than 460 ℃. Based on these merits, in 2016, Ma *et al.* first employed $CsPbBr_2I$ into IMH-PSCs successfully.[119] In their report, they prepared $CsPbBr_2I$ perovskite by the dual source evaporation method. According to systematic characterizations, the $CsPbBr_2I$ film annealed at 250 ℃ exhibited good quality in terms of crystallinity, thickness uniformity, and grain size uniformity. In order to simplify the architecture and eliminate all organic components in the PSCs, they fabricated an HTM-free IMH-PSC with the structure of FTO/c-TiO_2/$CsPbBr_2I$/Au. As a result, a PCE of 4.7% was obtained under reverse scanning mode. Unfortunately, a large hysteresis in this kind of PSC was detected and the PCE was 3.7% under forward scanning mode, as shown in **Fig. 8a**.

Obviously, the PCE of ~5% is too low for the $CsPbBr_2I$ perovskite with a bandgap of ~2.0 eV. Therefore, similar to $CsPbBr_3$-based IMH-PSCs, researchers also tried to improve the photovoltaic performances of $CsPbBr_2I$-based IMH-PSCs by the same strategies, including developing new preparation methods of $CsPbBr_2I$, doping the $CsPbBr_2I$ perovskite with heteroatoms, and optimizing the architecture of the $CsPbBr_2I$-based IMH-PSC.

As we mentioned above, the preparation methods of IMH perovskites are very important for their applications in PSCs because the film quality depends on the preparation method strongly. Therefore, except for the dual source evaporation method proposed by Ma *et al.*, other approaches were also developed to enhance the quality of the $CsPbBr_2I$ perovskite film. In the same group, Lau *et al.* prepared the $CsPbBr_2I$ perovskite film by a spray-assisted solution-processed method, as shown in **Fig. 8b**.[120] They used the spray method to prepare this perovskite because it is a common technique in industrial process and it is easy for making a large area cell as well as coating conformally. Moreover, the spray-assisted solution-processed method overcomes the issue of poor solubility of the bromide ion in the precursor solution faced by solution processing. Based on this method, Lau *et al.* fabricated dense $CsPbBr_2I$ perovskite films with small pinholes at high annealing temperature. Meanwhile, grain sizes of $CsPbBr_2I$ perovskites were in the range from 500 nm to 1000 nm. As a result, the PCE of the $CsPbBr_2I$-based IMH-PSC was improved to be 6.3% and the hysteresis seemed to be negligible (**Fig. 8b**). In another example, Guo *et al.* introduced a method of preheating-assisted one-step spin-coating method to prepare the $CsPbBr_2I$ perovskite film, as shown in **Fig. 8c**.[121] This method brought $CsPbBr_2I$ perovskite films high crystallinity, full coverage, micrometer-sized grains, and reduced defect densities. Finally, the PCE of the $CsPbBr_2I$-based IMH-PSC with the structure of ITO/SnO_2/$CsPbIBr_2$/spiro-OMeTAD/Ag was improved to 9.86%, as shown in **Fig. 8d-e**. Besides these novel preparation methods, other approaches were also proposed, e.g., intermolecular exchange route and antisolvent methods, all of which gave a high-quality $CsPbBr_2I$ film.[122-123]

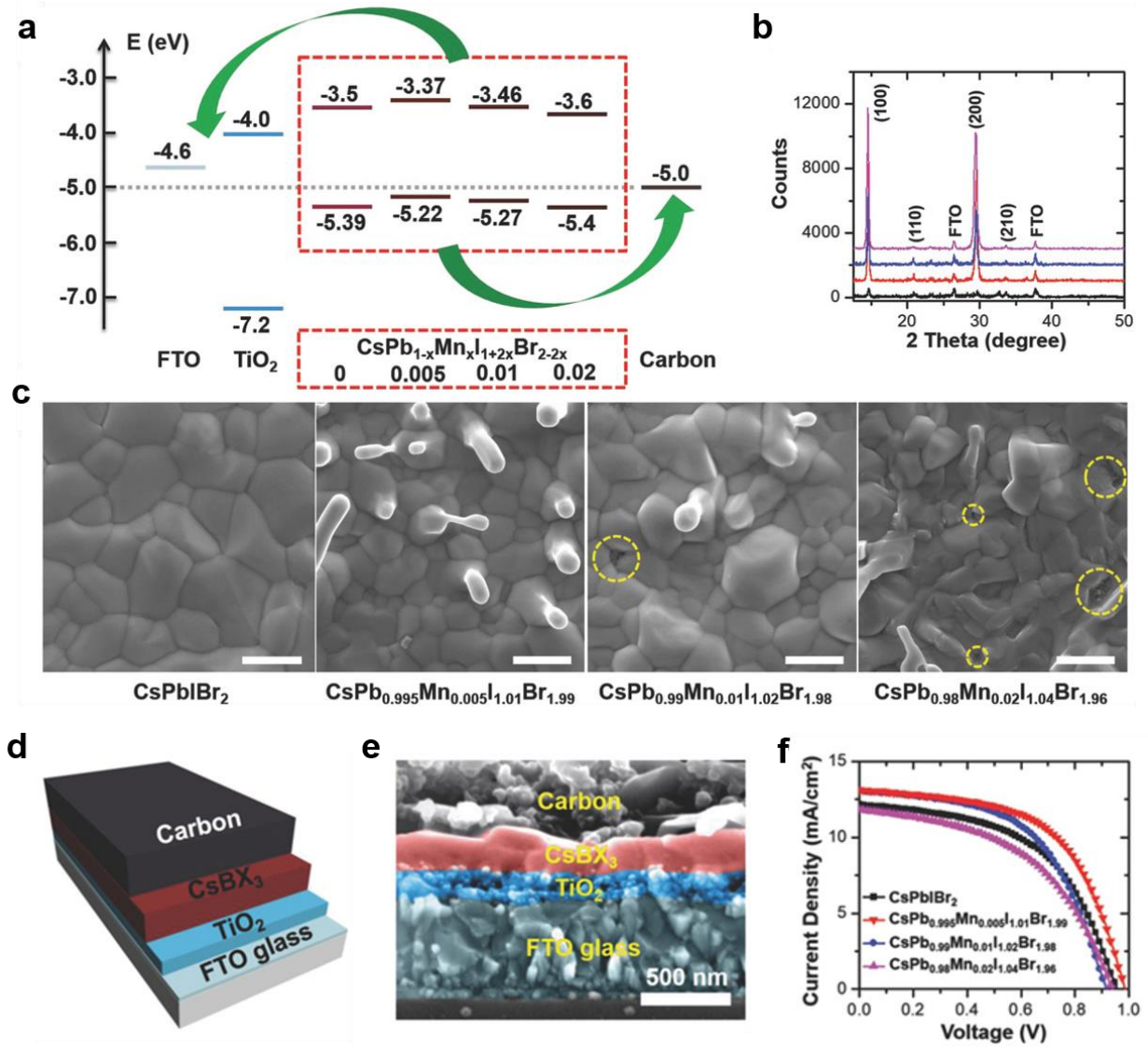

Fig. 9. a, Energy level diagram of FTO, TiO_2, $CsPbIBr_2$ (x = 0) and $CsPb_{1-x}Mn_xBr_{2-2x}I_{1+2x}$ perovskites (x = 0.005, 0.01, and 0.02), and carbon. **b**, XRD patterns and **c**, typical SEM images of $CsPbIBr_2$ and $CsPb_{1-x}Mn_xBr_{2-2x}I_{1+2x}$ (x = 0.005, 0.01, and 0.02) films, respectively. All the scale bars in **c** are 1 μm. The areas marked by yellow dash circles are several pinholes. **d**, Schematic diagram and **e**, cross-sectional SEM image of the IMH-PSC with the structure of FTO/c-TiO_2/m-TiO_2/$CsPbX_3$/carbon. **f**, *J-V* curves of the IMH-PSC with the structure of FTO/c-TiO_2/m-TiO_2/$CsPb_{1-x}Mn_xBr_{2-2x}I_{1+2x}$/carbon. Reproduced with permission from Liang *et al.* [124], Copyright (2018) Wiley-VCH Verlag GmbH & Co. KGaA, Weinheim.

As mentioned in Section 2.1, the CBM of the $CsPbX_3$ is mainly determined by the orbitals of Pb 6p. Doping the Pb-site in the $CsPbBr_2I$ perovskite by some heteroatoms will lead to characteristic changes on its CBM as well as bandgap and band alignment, all of which have a great influence on its light absorption. Therefore, impurity doping has been demonstrated to be an effective method to improve the photovoltaic performance. For example, Liang and coworkers used Mn^{2+}

as the dopant to modulate the properties of $CsPbBr_2I$ perovskites.[124] Because they used MnI_2 as the precursor of the Mn^{2+} dopants, the I:Br ratio varied with the change of Mn doping concentration. The absorption spectra showed that the bandgap was reduced from 1.89 eV of $CsPbBr_2I$ to 1.85 eV of $CsPb_{0.995}Mn_{0.005}Br_{1.99}I_{1.01}$, as shown in **Fig. 9a**. Moreover, XRD patterns and SEM images revealed that the Mn-doped perovskite of $CsPb_{0.995}Mn_{0.005}Br_{1.99}I_{1.01}$ exhibited better crystallinity and morphology than the $CsPbBr_2I$ perovskite, respectively (**Fig. 9b-c**). Based on these improved properties, Liang *et al.* fabricated IMH-PSCs with the structure of FTO/c-TiO_2/m-TiO_2/$CsPb_{0.995}Mn_{0.005}Br_{1.99}I_{1.01}$/carbon, which displayed an enhanced PCE of 7.36%, an increase of 19.9% when compared with $CsPbBr_2I$-based IMH-PSCs (**Fig. 9d-f**). Besides Mn^{2+} dopants, Liang *et al.* also tried to use Sn^{2+} as the dopant because Sn^{2+} is in the same group with Pb^{2+}.[125] The result showed when 1/10 Pb^{2+} was replaced by Sn^{2+}, the bandgap of the new perovskite $CsPb_{0.9}Sn_{0.1}Br_2I$ was reduced to 1.79 eV. With increased absorption, the IMH-PSCs based on $CsPb_{0.9}Sn_{0.1}Br_2I$ showed a remarkable PCE up to 11.33% and a high V_{OC} of 1.26 V. The dramatically enhanced photovoltaic performances in the above two works suggest that impurity doping is indeed an effective method to reduce the bandgaps of IMH perovskites and then improve their performances in PSC applications.

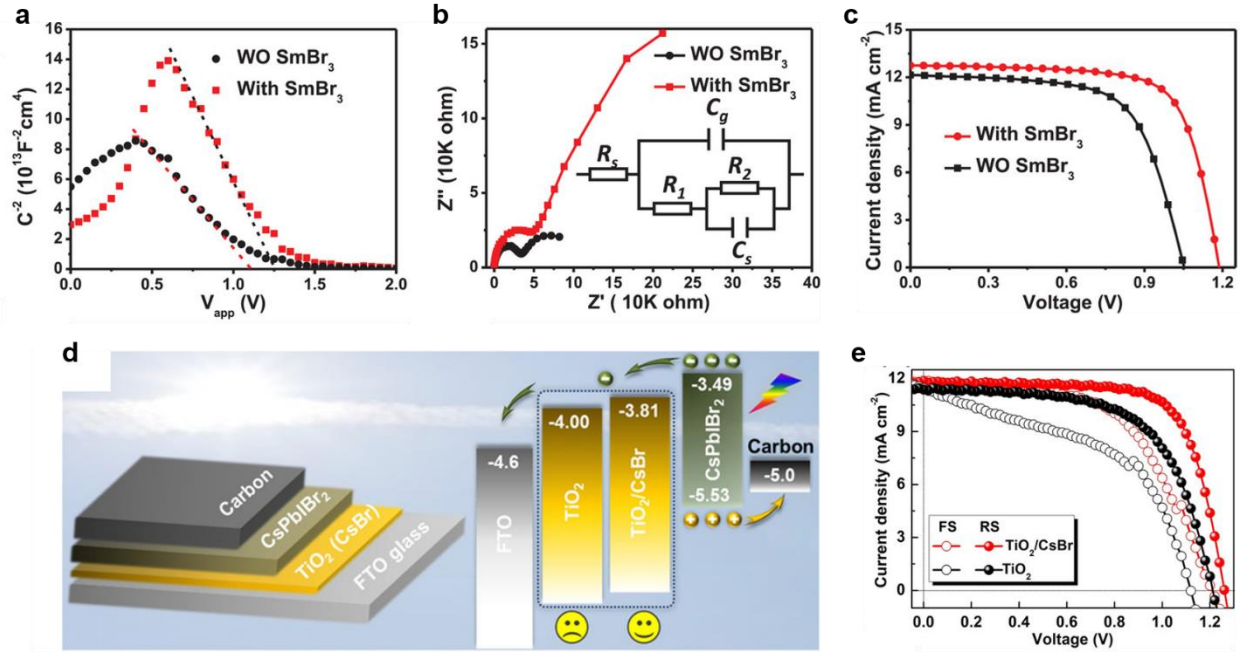

Fig. 10. a, Mott–Schottky curves of the $CsPbBr_2I$-based IMH-PSCs with and without $SmBr_3$ interface modification. **b**, Nyquist plots of the $CsPbBr_2I$-based IMH-PSCs with and without $SmBr_3$ interface modification under a bias voltage of 0 V. **c**, *J-V* curves of the $CsPbBr_2I$-based IMH-PSCs with $SmBr_3$ interface modification. Reproduced with permission from Subhani *et al.* [126], Copyright (2019) Wiley-VCH Verlag GmbH & Co. KGaA, Weinheim. **d**, Schematic diagram of the $CsPbBr_2I$-based IMH-PSCs with CsBr cluster layer. **e**, *J-V* curves of the $CsPbBr_2I$-based IMH-PSCs with CsBr cluster layer. Reproduced with permission from Zhu *et al.* [127], Copyright (2019) Wiley-VCH Verlag GmbH & Co. KGaA, Weinheim.

Besides the quality of the $CsPbBr_2I$ perovskite, the architecture of the $CsPbBr_2I$-based IMH-PSC is also vital for enhancing photovoltaic performance. Because the band structures of IMH perovskites have some changes when compared with those of OMH perovskites, some energy level mismatches can be found between IMH perovskites and traditional ETMs and HTMs, which may hinder charge extraction and transport. Band alignment engineering is an effective method to resolve this issue. In order to facilitate electron transfer between TiO_2 and $CsPbBr_2I$, Subhani *et al.* used $SmBr_3$ to enhance the TiO_2/$CsPbBr_2I$ interface interaction.[126] Encouragingly, a gradient energy band was created at the interface, which suppressed charge recombination occurring at the interface and the nonradiative recombination inside the perovskite and improved the charge extraction, as shown in **Fig. 10a-b**. As a result, the $SmBr_3$ interface modification enabled an increase of the performance of the $CsPbBr_2I$-based IMH-PSC by 30% in comparison with the analogous device without this layer, as shown in **Fig. 10c**. In the same year, Zhu *et al.* also employed CsBr cluster between TiO_2 and $CsPbBr_2I$.[127] Characterizations indicated that CsBr clusters triggered an increase in CBM from -4.00 to -3.81 eV and a decrease in work function from 4.11 to 3.86 eV for the TiO_2 layer, which promoted favorable band alignment, suppressed recombination, and improved charge carrier extraction and transport between TiO_2 and $CsPbBr_2I$ (**Fig. 10d**). As a result, the performance of the corresponding PSC exhibited a more than 20% enhancement in PCE (**Fig. 10e**).

3.2.2 $CsPbBrI_2$-based IMH-PSCs

Furthermore, replacing 2/3 bromide in $CsPbBr_3$ by iodine will form $CsPbBrI_2$, which has a smaller bandgap of ~1.85 eV and is promising for inclusion in tandem devices with c-Si and copper indium gallium selenide solar cells. Although the stability of the $CsPbBrI_2$ perovskite is poorer than that of the $CsPbBr_2I$ perovskite, it is better than the $CsPbI_3$ perovskite. In order to employ $CsPbBrI_2$ perovskites into IMH-PSCs, Sutton *et al.* first prepared a uniform $CsPbBrI_2$ perovskite thin film by a one-step solution processing route.[128] PL spectra and XRD patterns demonstrated that this material had a smaller bandgap of 1.92 eV when compared with the $CsPbBr_2I$ perovskite and better stability when compared with the $CsPbI_3$ perovskite. After assembling the $CsPbBrI_2$ perovskite into the IMH-PSC with the structure of FTO/c-TiO_2/m-TiO_2/$CsPbBrI_2$/spiro-OMeTAD/Ag, a champion PCE of 9.84% and an average PCE of 6.02% were achieved.

Compared with OMH-PSCs, the initial PCE of the $CsPbBrI_2$-based IMH-PSC is not very high. Therefore, a lot of approaches were put forward to improve its photovoltaic performance. In order to reverberate with $CsPbBr_3$ and $CsPbBr_2I$ perovskites, we also divide these approaches into three categories, including developing novel preparation methods, doping the $CsPbBrI_2$ perovskite with heteroatoms, and optimizing the architecture of the $CsPbBrI_2$-based IMH-PSC.

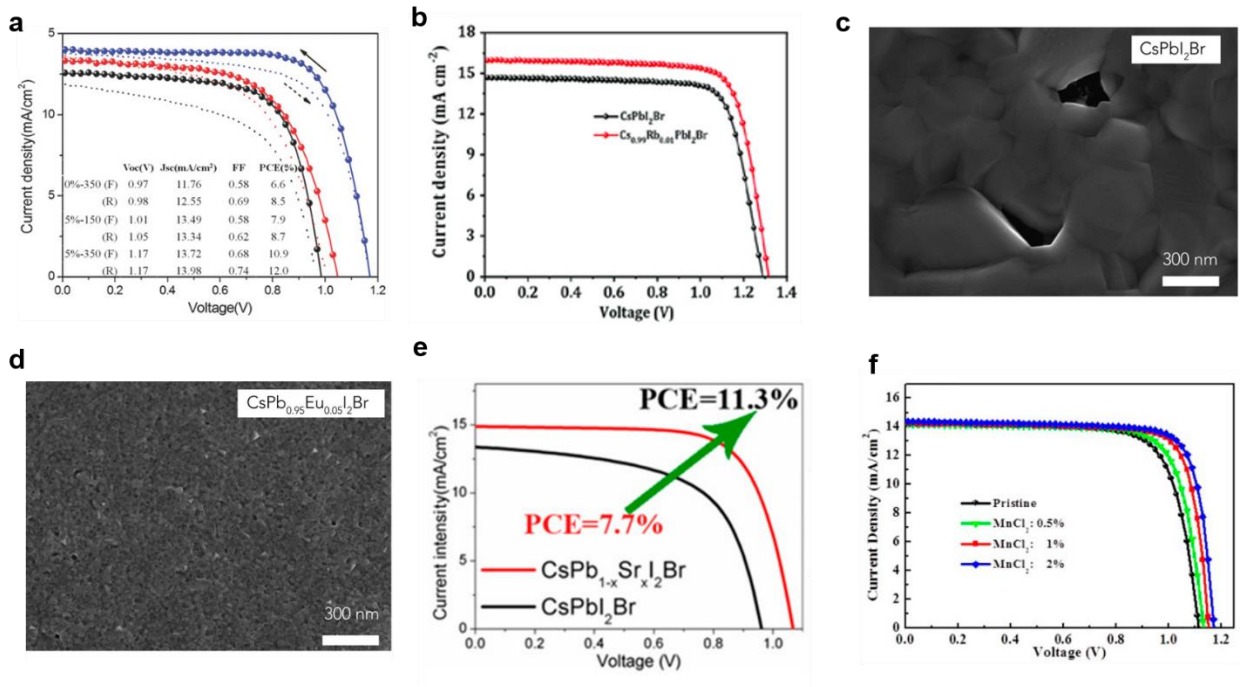

Fig. 11. a, *J-V* curves of the IMH-PSC based on the $CsPbBrI_2$ perovskite fabricated by the *in situ* grain boundary functionalization approach. Reproduced with permission from Zeng *et al.* [131], Copyright (2018) Wiley-VCH Verlag GmbH & Co. KGaA, Weinheim. **b**, *J-V* curves of the IMH-PSC based on the $CsPbBrI_2$ perovskite with and without the Rb dopants. Reproduced with permission from Patil *et al.* [134], Copyright (2020) Wiley-VCH Verlag GmbH & Co. KGaA, Weinheim. Typical SEM images of **c**, the $CsPbBrI_2$ perovskite and **d**, the $CsPb_{0.95}Eu_{0.05}BrI_2$ perovskite. Reproduced with permission from Xiang *et al.* [136], Copyright (2019) Elsevier. *J-V* curves of the IMH-PSC based on the $CsPbBrI_2$ perovskite doped by **e**, Sr^{2+} and **f**, Mn^{2+}. Reproduced with permission from Lau *et al.* [137], Copyright (2017) American chemistry society. Reproduced with permission from Bai *et al.* [139], Copyright (2018) American chemistry society.

For the strategy of developing new preparation methods, Ma *et al.* proposed the dual source thermal evaporation method to prepare $CsPbBrI_2$ perovskite thin films. Meanwhile, they investigated the effect of the stoichiometry on the stability of $CsPbBrI_2$ perovskite thin films. As a result, the PCE of the $CsPbBrI_2$-based IMH-PSC was enhanced to 7.7%.[129] Wang and coworkers developed a one-step method and a 100-130 °C low temperature annealing process to synthesize $CsPbBrI_2$ perovskite thin films. By adjusting precursors, the PCE of the $CsPbBrI_2$-based IMH-PSC was improved to 10.56%.[130] In the same year, Zeng *et al.* put forward the *in situ* grain boundary functionalization approach to fabricate $CsPbBrI_2$ perovskite thin films. By annealing at high temperature, a PCE as high as 12% was achieved, as shown in **Fig. 11a**.[131] Moreover, Xue and coworkers put forward a surface-induced secondary grain growth technique to prepare the $CsPbBrI_2$ perovskite thin films.[132] In their work, they spin-coated an ammonium iodide isopropanol solution onto the crystallized perovskite thin films. As a result, the PCE of $CsPbBrI_2$-based IMH-PSC was enhanced to 16.58%.[132] Recently, Wang and coworkers have proposed a strategy of intermediate adduct (IMAT) engineering to improve the performance of the $CsPbBrI_2$-

based IMH-PSC.[133] In their study, they incorporated (chloromethylene)-dimethylammonium chloride into the precursor to form an IMAT precursor via the strong bond between C=N and perovskite compound. As a result, a high V_{OC} of 1.26 V and a champion PCE of 16.02% were obtained.[133] In these works, such high PCEs can be ascribed to the improved quality of $CsPbBrI_2$ perovskite films, such as large grain size, low recombination rate, and no pinhole, created by these new preparation methods.

For the strategy of doping the $CsPbBrI_2$ perovskite with some heteroatoms, Nam *et al.* incorporated potassium (K) cations into the A-site of the $CsPbBrI_2$ perovskite to form a new $Cs_{0.925}K_{0.075}PbBrI_2$ perovskite. Based on various characterizations, the new film showed efficient carrier extraction, improved carrier generation and transportation. Therefore, IMH-PSCs based on $Cs_{0.925}K_{0.075}PbBrI_2$ perovskites showed an enhanced PCE of 10%, as well as extended operational lifetime against air. Similarly, Patil and coworkers introduced rubidium (Rb) cations into the $CsPbBrI_2$ perovskite under ambient conditions.[134] According to various characterizations, the new $Cs_{1-x}Rb_xPbI_2Br$ perovskites exhibited uniform grains, pinhole-free morphology, high crystallinity, and extremely dense. As a result, the fabricated IMH-PSCs with the $Cs_{0.99}Rb_{0.01}PbI_2Br$ perovskite showed a PCE of 17.16%, which was much higher than the IMH-PSCs with the $CsPbI_2Br$ perovskite, as shown in **Fig. 11b**. Besides the Cs-site replacement, the Pb-site of the $CsPbBrI_2$ perovskite can also be replaced by some dopants. In organic-inorganic hybrid PSCs, europium (Eu) has been regarded as an efficient dopant to improve their PCEs because its slightly smaller radium is expected to be incorporated into the perovskite lattice to increase the tolerance factor and result in an enhancement of the perovskite stability.[135] Therefore, Xiang and coworkers incorporated Eu cations into the $CsPbBrI_2$ perovskite to stabilize its α-phase at room temperature.[136] In addition, the incorporation of Eu boosted the morphology of the $CsPbBrI_2$ perovskite and reduced their non-radiative recombination, as shown in **Fig. 11c-d**. As a result, the IMH-PSCs based on $CsPb_{0.95}Eu_{0.05}BrI_2$ perovskites showed a higher PCE of 13.34% and a larger V_{OC} of 1.27 V. Moreover, the solid-state nuclear magnetic resonance and high-angle annular dark-field scanning transmission electron microscopy revealed that Eu was incorporated into the perovskite lattice. Besides Eu dopants, other dopants at the Pb-site, such as Ge, Sr, and Mn, were also introduced into the $CsPbBrI_2$ perovskite to form new perovskites.[137-141] Just like $CsPb_{0.95}Eu_{0.05}BrI_2$ perovskites, all of these new perovskites showed large grain sizes, high effective lifetime and other improved properties, which were beneficial for their applications in PSCs. However, the incorporation mechanisms were distinct for different dopants. Some dopants, just like the Eu dopant, may substitute for Pb ions in the lattice without changing the original octahedral structure, while the other dopants may insert into the interstices of the $CsPbBrI_2$ lattice structure during the thin film growth process. Regardless of which incorporation mechanism it is, all of them exhibited improved photovoltaic performances, as shown in **Fig. 11e-f**.[137-141]

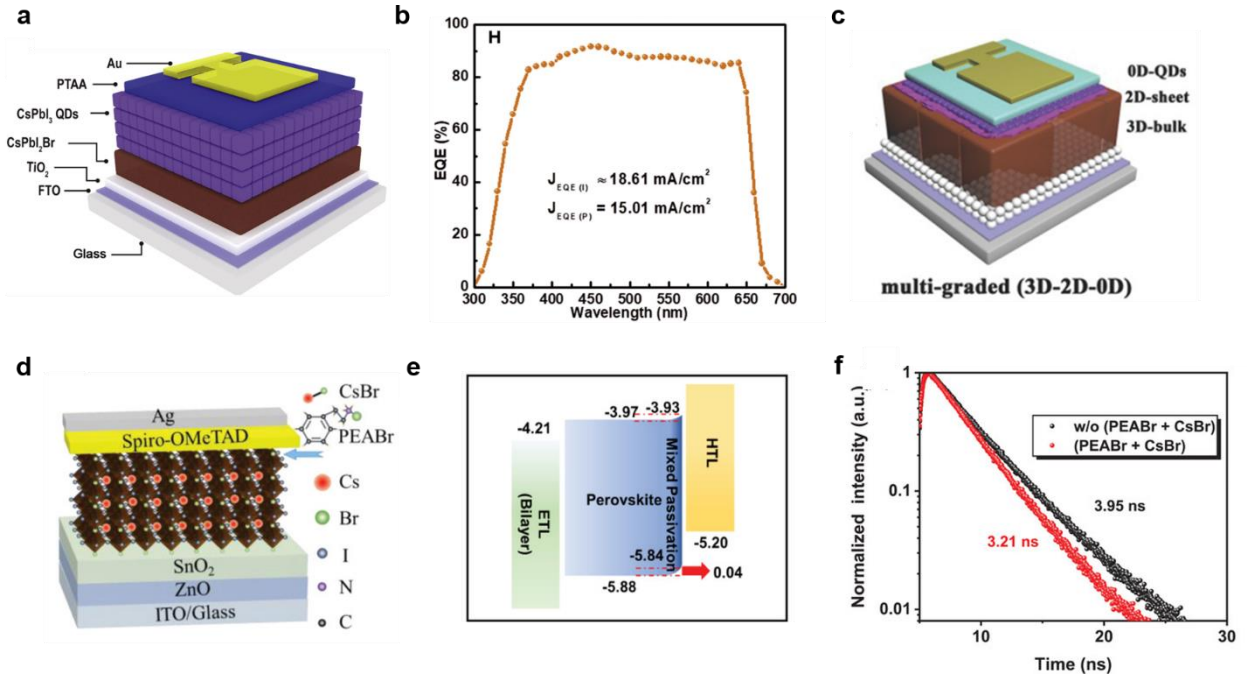

Fig. 12. a, Schematic diagram of the $CsPbBrI_2$-based IMH-PSC with an integrated perovskite layer based on the IMH perovskites of $CsPbBrI_2$ and $CsPbI_3$ quantum dot film. **b**, IPCE spectrum of the $CsPbBrI_2$-based IMH-PSC in **a**. Reproduced with permission from Bian *et al.* [142], Copyright (2019) Elsevier. **c**, Schematic diagram of the $CsPbBrI_2$-based IMH-PSC with a 3D-2D-0D dimension-profiled perovskite layer. Reproduced with permission from Zhang *et al.* [143], Copyright (2018) Wiley-VCH Verlag GmbH & Co. KGaA, Weinheim. **d**, Schematic diagram and **e**, energy band diagram of the $CsPbBrI_2$-based IMH-PSC with a mixed passivation layer between $CsPbBrI_2$ and spiro-OMeTAD. **f**, TRPL curves of the $CsPbBrI_2$ perovskite films with and without the mixed passivation layer. Reproduced with permission from He *et al.* [144], Copyright (2021) Wiley-VCH Verlag GmbH & Co. KGaA, Weinheim.

For the strategy of optimizing the architecture of the $CsPbBrI_2$-based IMH-PSC, a number of approaches were tried to improve their performance as well. For example, Bian *et al.* reported an integrated structure based on IMH perovskites of $CsPbBrI_2$ and $CsPbI_3$ quantum dot film, as shown in **Fig. 12a**.[142] This kind of IMH-PSC could harvest the light from 300 nm to 700 nm, covering most of the visible solar spectrum (**Fig. 12b**). The graded band structure was beneficial for improving its carrier collection. Therefore, IMH-PSCs with this new structure showed an improved PCE as high as 14.45%. In the same group, Zhang *et al.* also reported another new structure for the $CsPbBrI_2$-based IMH-PSC, in which $CsPbBrI_2$ perovskites were distributed within bulk-nanosheet-quantum dots or the 3D-2D-0D dimension-profiled interface structure, as shown in **Fig. 12c**.[143] Upon optimization, improved hole extraction, decreased recombination loss, and well-matched energy levels together afforded a PCE as high as 12.39%. Moreover, similar to the addition of the $SmBr_3$ layer in the $CsPbBr_2I$-based IMH-PSCs as a passivation layer,[126] He and coworkers also added a mixed passivation layer of phenylethylammonium bromide and cesium bromide between $CsPbBrI_2$ and spiro-OMeTAD in the $CsPbBrI_2$-based IMH-PSCs,[144] as shown in **Fig. 12d**. Besides reducing the low trap density in the $CsPbBrI_2$ perovskite layer, the mixed

passivation layer also improved the energy level alignment, facilitated the hole extraction at the $CsPbBrI_2$/spiro-OMeTAD interface, drove the interface electron separation, and suppressed the charge recombination, as shown in **Fig. 12e-f**. As a result, the $CsPbBrI_2$-based IMH-PSCs showed a higher PCE of 16.7%, a V_{OC} of 1.3 V, and an excellent FF of 0.82. Moreover, this IMH-PSC exhibited remarkable long-term stability. [144]

For comparison, the photovoltaic performances of the $CsPb(Br_xI_{1-x})_3$-based IMH-PSCs, including $CsPbBr_2I$- and $CsPbBrI_2$-based IMH-PSCs, are listed in **Table 1**.[119,123,127-162] Although the stability of $CsPb(Br_xI_{1-x})_3$ became poorer when compared with $CsPbBr_3$, it was improved when new preparation methods were developed or some dopants were added into their lattices. Meanwhile, the photovoltaic performances of $CsPb(Br_xI_{1-x})_3$-based IMH-PSCs were enhanced when compared with $CsPbBr_3$-based IMH-PSCs because of their narrower bandgaps. Therefore, it is promising to study $CsPb(Br_xI_{1-x})_3$-based IMH-PSCs and their applications in tandem devices.

3.3 $CsPbI_3$-based IMH-PSCs

$CsPbI_3$ possesses four types of crystal polymorphs, including α-, β-, γ-, and δ-phases, and it prefers the δ-phase with a bandgap of 2.8 eV with respect to the α-, β-, and γ-phases due to the thermodynamic equilibrium. However, the $CsPbI_3$ perovskite in δ-phase is not suitable for the application in PSCs. The transition of $CsPbI_3$ from δ-phase to α-, β-, and γ-phases can be ascribed to its own lattice structure, which can be stabilized in the perovskite structure (α-, β-, and γ-phases) under the designated temperature. At room temperature, the $CsPbI_3$ perovskite film cannot maintain its perovskite structure, and tends to form a δ-phase. In 2014, the first $CsPbI_3$-based IMH-PSC with a PCE of 0.09% was reported by Choi *et al.*[35] when they tried to introduce Cs^+ into $MAPbI_3$-based OMH-PSCs. Such a low PCE can be ascribed to the δ-phase $CsPbI_3$ perovskite, which further demonstrated that the δ-phase $CsPbI_3$ is not suitable for the application in PSCs. Therefore, it is imperative to keep $CsPbI_3$ perovskite films in black phases, including α-, β-, and γ-phases, to achieve a high PCE for the $CsPbI_3$-based IMH-PSC. In order to achieve this goal, Eperon *et al.* prepared black $CsPbI_3$ perovskite films by careful processing control and development of a low-temperature phase transition.[163] Specifically, they added some hydroiodic (HI) acid into the precursor solution before spin-coating, and then converted $CsPbI_3$ perovskite film from yellow to black phase at 100 ℃. As a result, the first black $CsPbI_3$-based IMH-PSC with a PCE of 2.9% was obtained. Although this PCE was much higher than 0.09%, it was still much lower compared with the theoretical limit for a material with a bandgap of ~1.7eV. So far, a great deal of effort has been dedicated to improving the stability and efficiency of the $CsPbI_3$-based IMH-PSC and many of them showed promising results. Similar to $CsPbBr_3$ and $CsPb(Br_xI_{1-x})_3$, we also review these efforts from three aspects, including developing new preparation methods, doping the $CsPbI_3$ perovskite with heteroatoms, and optimizing the architecture of the $CsPbI_3$-based IMH-PSC.

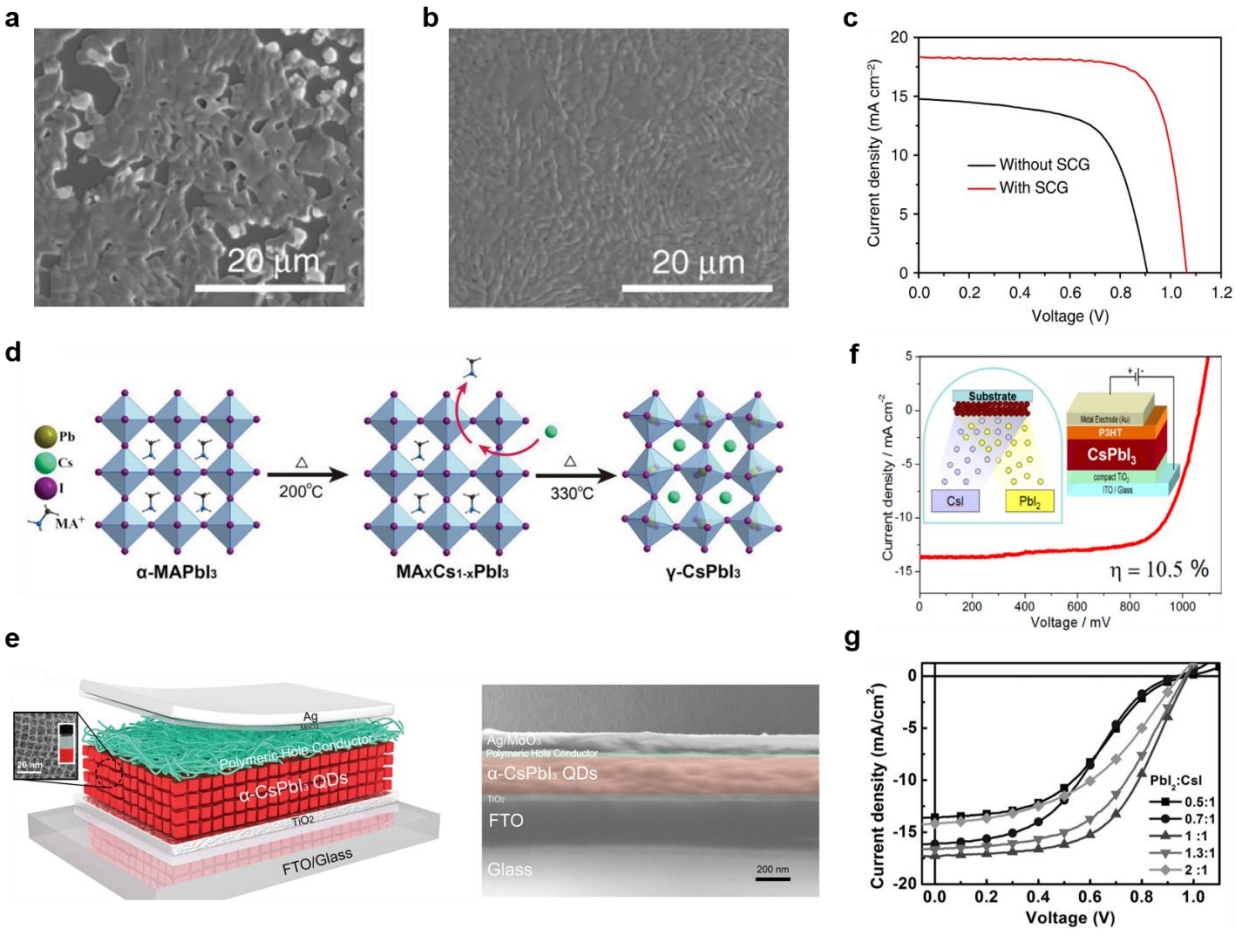

Fig. 13. Typical SEM images of $CsPbI_3$ perovskite films prepared by **a**, the common solution-processing method and **b**, the solvent-controlled growth method. **c**, *J-V* curves of the IMH-PSCs based on the $CsPbI_3$ films prepared by the common solution-processing method or solvent-controlled growth method. Reproduced with permission from Wang *et al.* [164], Copyright (2018) Springer Nature. **d**, Schematic diagram of the $CsPbI_3$ perovskite films prepared by the cation exchange growth method. Reproduced with permission from Lau *et al.* [166], Copyright (2019) Wiley-VCH Verlag GmbH & Co. KGaA, Weinheim. **e**, Schematic diagram and cross-sectional SEM image of the IMH-PSC based on the $CsPbI_3$ nanocrystal film. Reproduced with permission from Yuan *et al.* [167], Copyright (2018) Elsevier. **f**, *J-V* curve of the $CsPbI_3$-based IMH-PSC, in which the $CsPbI_3$ film was prepared by the thermal evaporation method. The inset is the schematic diagram of the thermal evaporation method. Reproduced with permission from Frolova *et al.* [169], Copyright (2017) American Chemistry Society. **g**, *J-V* curves of the IMH-PSCs based on the $CsPbI_3$ films prepared by the thermal evaporation method with different ratios of precursors. Reproduced with permission from Chen *et al.* [170], Copyright (2017) Wiley-VCH Verlag GmbH & Co. KGaA, Weinheim.

To deliver a higher PCE for the $CsPbI_3$-based IMH-PSCs, the quality of the $CsPbI_3$ perovskite film is important, as the pinholes and grain boundaries usually result in serious recombination and poor photovoltaic performance. The quality of the perovskite film mainly depends on the preparation

method, especially for $CsPbI_3$ perovskite films because their quality prepared by the initial solution-processing method was poor, as shown in **Fig. 13a**.[164] Therefore, developing new preparation methods is key to enhancing the PCE or stability of the $CsPbI_3$-based IMH-PSC. Liang and coworkers developed a facile and scalable synthesis approach to produce $CsPbI_3$ powder with high yield and reproducibility.[165] After dissolving $CsPbI_3$ powder into the DMF solution, a PCE as high as 4.65% was obtained for the $CsPbI_3$-based IMH-PSC with the structure of FTO/c-TiO_2/$CsPbI_3$/carbon. In order to further increase the PCE, Wang *et al.* developed the solvent-controlled growth method to prepare $CsPbI_3$ perovskite films.[164] In their method, the $CsPbI_3$ perovskite films were free of pinholes and showed crystal size above 5 μm (**Fig. 13b**). Moreover, the $CsPbI_3$ perovskite films showed good stability when they were stored in dry nitrogen box for 7-60 days. As a result, when Wang and coworkers fabricated the $CsPbI_3$-based IMH-PSC with the structure of ITO/SnO_2/$CsPbI_3$/spiro-OMeTAD/Au, the PCE was increased from 8.58% to 15.75%, as shown in **Fig. 13c**. Meanwhile, this $CsPbI_3$-based IMH-PSC could tolerate over 500h under constant illumination. As for the processing optimization, deposition of $MAPbI_3$ perovskite films exhibited the best example among all perovskites because it has been studied extensively for more than 10 years. Making full use of the excellent quality of the $MAPbI_3$ perovskite film, Lau *et al.* put forward a simple cation exchange growth method and then produced a high quality $CsPbI_3$ perovskite film with black phase.[166] Specifically, they used a $MAPbI_3$ perovskite film as a template for Cs^+ to replace MA^+ to form $CsPbI_3$ perovskite film with compact and pinhole-free morphology, as shown in **Fig. 13d**. Moreover, this $CsPbI_3$ perovskite film also showed better crystallinity and longer carrier lifetime. Therefore, the IMH-PSC based on this $CsPbI_3$ perovskite film displayed a PCE as high as 14.1%.

Highly crystalline $CsPbI_3$ nanocrystals were demonstrated to be stable and considered as a powerful platform for stable optoelectronics devices because of their high surface-to-volume ratio and high surface energy. Therefore, employing them into $CsPbI_3$-based IMH-PSCs is promising (**Fig. 13e**) [167]. However, it is very difficult to make them a uniform film until Swarnkar *et al.* put forward an effective method to cast electronically conductive nanocrystal films.[38] In this method, the nanocrystals were first spin-cast on the substrate, and then dipped in a saturated MeOAc solution of either $Pb(OAc)_2$ or $Pb(NO_3)_2$. As a result, when they fabricated IMH-PSCs with this $CsPbI_3$ nanocrystal film, a large PCE of 10.77% and a large V_{OC} of 1.23 V were observed. Meanwhile, this kind of $CsPbI_3$-based IMH-PSCs showed excellent stability. However, in this work, the thickness of the $CsPbI_3$ layer was ~ 200 nm, which was thinner than traditional OMH perovskite layers. A direct result is that although the thin $CsPbI_3$ layer gave a high PCE, its current density (J_{SC}) was still limited. Therefore, how to control the thickness and then obtain a high PCE is an open question. In the same group, Sanehira *et al.* proposed a post-treatment to tune and improve the electronic coupling between nanocrystals.[168] Based on the enhanced carrier mobility in $CsPbI_3$ films, the PCE of $CsPbI_3$-based IMH-PSCs was increased to 13.43% with the thickness of $CsPbI_3$ nanocrystal layer of ~ 400 nm.

Compared with solution-processing methods, it has also been reported to use the thermal evaporation method to prepare $CsPbI_3$ perovskite films. For example, Frolova *et al.* prepared $CsPbI_3$ perovskite films by thermal coevaporation of CsI and PbI_2, as shown in **Fig. 13f**.[169] Characterization results showed that this kind of $CsPbI_3$ film exhibited high purity, uniform

morphology, good crystallinity. Moreover, Frolova *et al.* demonstrated that this method was reproducible, while the solution-processing method was strongly affected by the solvent properties, wetting, and other parameters. As a result, the best IMH-PSC based on this kind of $CsPbI_3$ film showed a PCE of 10.5% (**Fig. 13f**). Later, in order to make $CsPbI_3$-based IMH-PSCs toward industrial fabrication, Chen *et al.* developed an all-vacuum-deposited device, in which the $CsPbI_3$ film was vacuum deposited by co-sublimation of CsI and PbI_2, combining with the vacuum-sublimed ETMs and HTMs. In this work, they studied the stoichiometric ratio of the precursors and demonstrated its importance for the device performance. Finally, the stoichiometrically balanced $CsPbI_3$-based IMH-PSCs delivered the PCE as high as 9.4%, as shown in **Fig 13g**.[170]

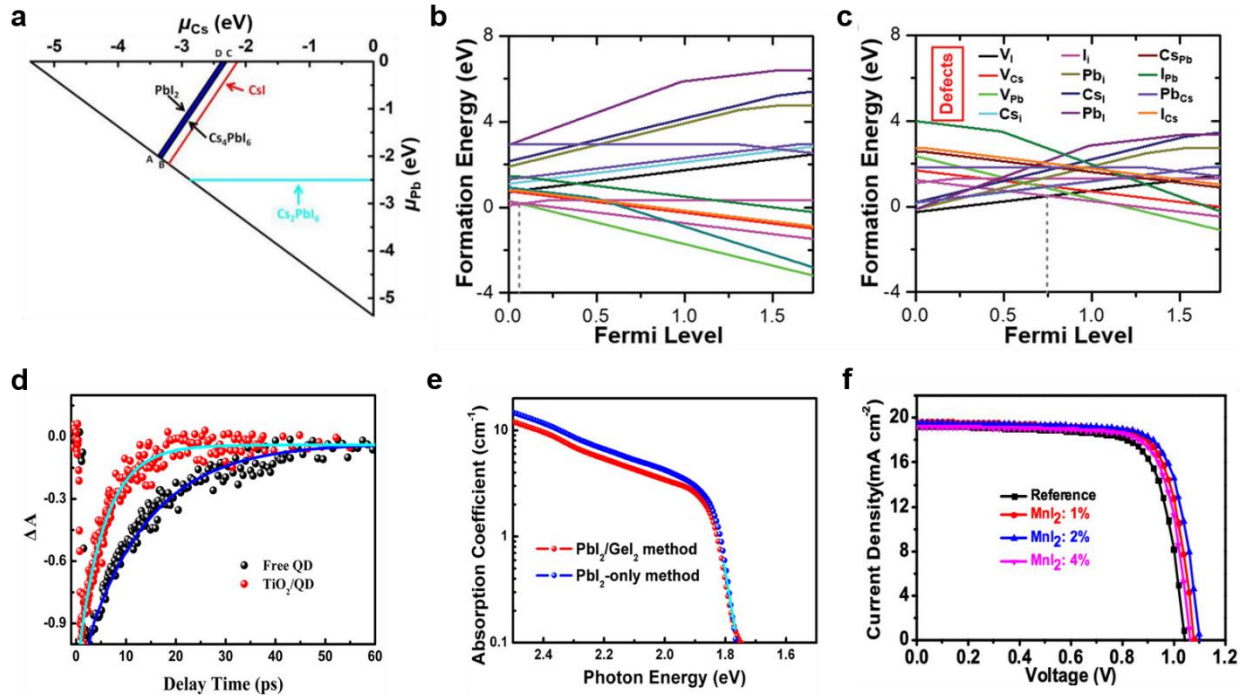

Fig. 14. a, The thermodynamic stability range for the equilibrium growth of $CsPbI_3$ (blue region). The defect formation energies as a function of the Fermi level of 12 native point defects in $CsPbI_3$ calculated under **b**, lead-rich and **c**, lead-poor growth condition. Reproduced with permission from Liang *et al.* [171], Copyright (2019) Wiley-VCH Verlag GmbH & Co. KGaA, Weinheim. **d**, TA responses of the free $CsSn_{0.6}Pb_{0.4}I_3$ perovskite and $CsSn_{0.6}Pb_{0.4}I_3/TiO_2$ composite measured with a pump light wavelength of 470 nm and probe light wavelengths of 760 nm. Reproduced with permission from Liu *et al.* [172], Copyright (2017) American chemistry society. **e**, UV-vis spectra of the $CsPbI_3$ perovskite films with and without GeI_2 in their precursors. Reproduced with permission from Liu *et al.* [173], Copyright (2019) American chemistry society. **f**, *J-V* curves of the IMH-PSC based on the $CsPbI_3$ perovskites with and without Mn^{2+}. Reproduced with permission from Yao *et al.* [181], Copyright (2020) American chemistry society.

In the studies on the $CsPbI_3$ perovskite, it was demonstrated that there were lots of unavoidable shallow- or deep-level defects in $CsPbI_3$ perovskites during crystal formation. Liang and coworkers investigated the distribution of native point defects in the $CsPbI_3$ perovskite using the DFT method.[171] The chemical potential chart of Pb *vs.* Cs and the formation energies of the 12

native point defects in $CsPbI_3$ perovskites were calculated, as shown in **Fig. 14a-c**. The calculation results showed that such a large number of defects in $CsPbI_3$ perovskites could be ascribed to the elements of Pb and I. In $CsPbBr_3$ perovskites, it has been mentioned that the incorporation of a small number of additives into perovskites was an effective strategy to realize a high-quality perovskite film with a low defect density. Therefore, many works on introducing a small number of additives in $CsPbI_3$ perovskites have been conducted. These additives can be divided into two kinds, one is the inorganic component, and the other is the organic component.

As an element in the same group with Pb, Sn was introduced into $CsPbI_3$ perovskites to replace part of Pb by Liu and coworkers.[172] The new perovskite of $CsSn_xPb_{1-x}I_3$ showed better stability than perovskites of $CsPbI_3$ and $CsSnI_3$, and was stable when exposed to ambient for a long time. Although this perovskite was not assembled into an IMH-PSC, Liu and coworkers investigated the exciton dynamics in the sample of $CsSn_xPb_{1-x}I_3/TiO_2$ by the ultrafast transient absorption (TA) spectroscopy, which demonstrated that the photoexcited electrons in $CsSn_xPb_{1-x}I_3$ can transfer into TiO_2 at a fast rate of 1.12×10^{11} s^{-1}, as shown in **Fig. 14d**, suggesting that $CsSn_xPb_{1-x}I_3$ was a promising material in the PSC application. In the same group, Liu *et al.* also tried to incorporate Ge, another element in the same group with Pb, into $CsPbI_3$ perovskites.[173] Due to the different mechanism from Sn, Ge was not incorporated into $CsPbI_3$ lattice. Therefore, the intrinsic properties of $CsPbI_3$ perovskites were not affected by the incorporation of Ge, such as the bandgap, as shown in **Fig. 14e**. It seems that this incorporation was an invalid method, however, introduction of GeI_2 brought other significant advantages such as less toxic Pb waste, better surface passivation, and better reproducibility. In this work, Liu *et al.* also fabricated an IMH-PSC based on this kind of $CsPbI_3$ perovskite and a PCE of over 12% was obtained. Except for the elements from the same group with Pb, elements from other groups, such as Bi, Sb, Mn, and so on, were also tried to introduce into $CsPbI_3$ perovskites to enhance their photovoltaic performances.[174-181] Most of these additives led to better morphologies, higher crystallinities, and lower defect densities in $CsPbI_3$ perovskite films. Therefore, the IMH-PSCs based on $CsPbI_3$ perovskites with these additives showed better stability and higher PCEs. Especially for the $CsPbI_3$ perovskite with Mn^{2+} additives, its PCE reached to 16.52%, which had an enhancement of ~10% when compared with the control sample (**Fig. 14f**).[181] Moreover, this kind of IMH-PSC also showed an enhanced humidity and thermal stability.

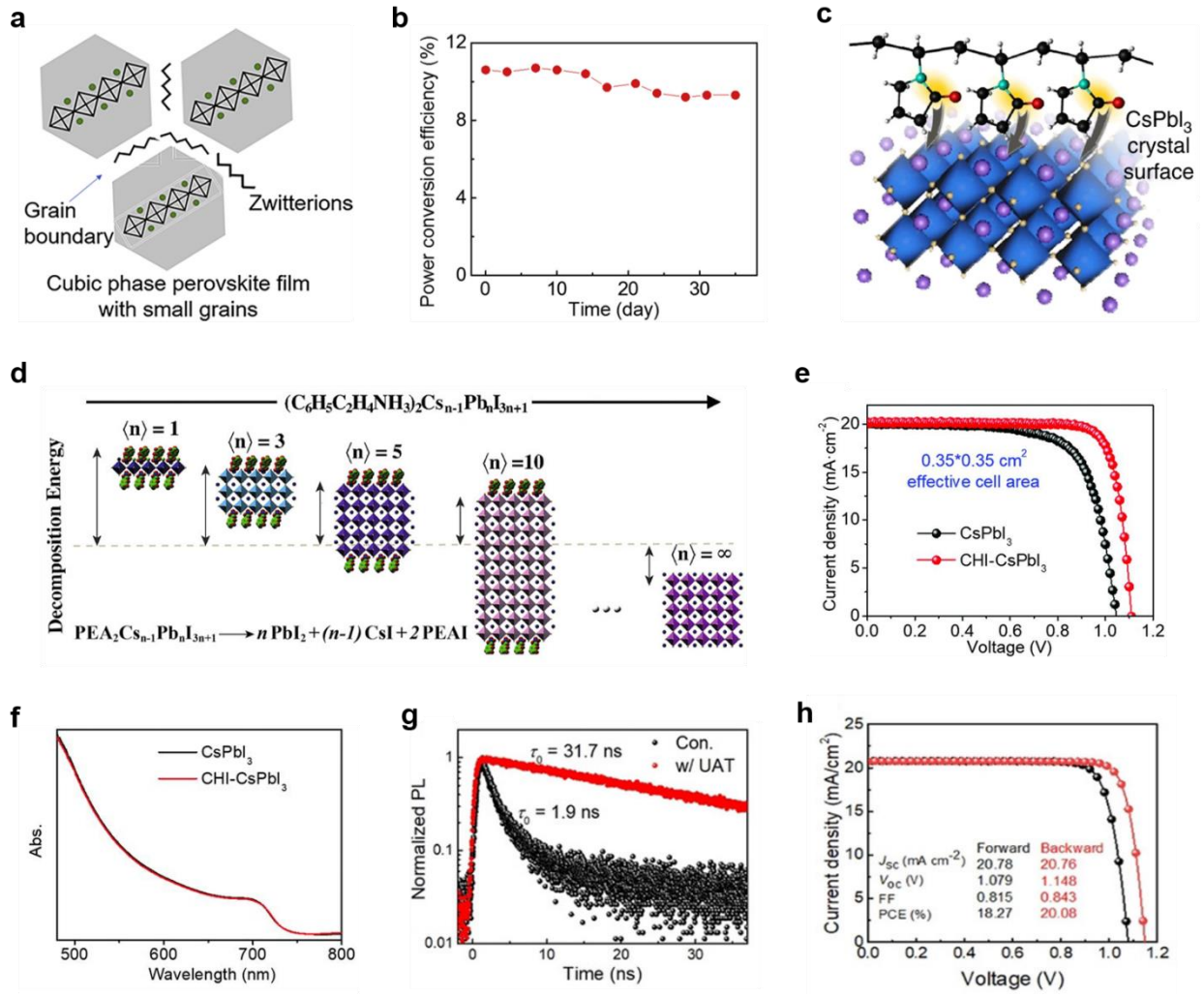

Fig. 15. a, The zwitterion molecules are expelled toward the grain surface and grain boundaries during $CsPbI_3$ grain growth, which leads to small grains. **b**, The PCE of the IMH-PSCs based on $CsPbI_3$ with the treatment of sulfobetaine zwitterion as a function of storage time. Reproduced with permission from Wang *et al.* [182], Copyright (2018) Elsevier. **c**, PVP anchored at the surface of the $CsPbI_3$ perovskites via the combination between N/O and Cs. Reproduced with permission from Li *et al.* [183], Copyright (2018) Springer Nature. **d**, Schematic showing the introduction of PEA into $CsPbI_3$ perovskites with different ratios. Reproduced with permission from Jiang *et al.* [184], Copyright (2019) Elsevier. **e**, *J-V* curves, and **f**, UV-vis spectra of the IMH-PSC based on the $CsPbI_3$ perovskites with and without the treatment of CHI. Reproduced with permission from Wang *et al.* [68], Copyright (2019) AAAS. **g**, TRPL spectra of the IMH-PSC based on the $CsPbI_3$ perovskites with and without the treatment of UAT. **h**, *J-V* curves of the IMH-PSC based on the $CsPbI_3$ perovskites with the treatment of UAT under different testing modes. Reproduced with permission from Yu *et al.* [185], Copyright (2021) Wiley-VCH Verlag GmbH & Co. KGaA, Weinheim.

As mentioned above, the IMH-PSCs based on $CsPbI_3$ nanocrystal films showed excellent stability, because their high surface-to-volume ratio made Gibbs free energy become the dominant factor in

the surface energy. Hence, it can effectively enhance the photovoltaic performances of $CsPbI_3$-based IMH-PSCs by reducing the grain size and increasing the surface-to-volume ratio in the $CsPbI_3$ perovskite film. This kind of structure was also achieved by Wang and coworkers through introducing a small amount of sulfobetaine zwitterion into the $CsPbI_3$ precursor solution, in which the average size of grain size was ~30 nm.[182] This can be ascribed to the zwitterions impeded the crystallization of $CsPbI_3$ perovskite films *via* electrostatic interaction with the ions and colloids in the $CsPbI_3$ precursor solution, as shown in **Fig. 15a**. As a result, the IMH-PSC based on the $CsPbI_3$ perovskite with the treatment of sulfobetaine zwitterion showed an PCE as high as 11.4%, as well as excellent stability (**Fig. 15b**). Following the same mechanism, Li *et al.* achieved the similar result by introducing polymer poly-vinylpyrrolidone (PVP) into the $CsPbI_3$ perovskite.[183] In their report, the grain size of the $CsPbI_3$ perovskite film was reduced to around 100 nm. Moreover, the acylamino groups of PVP induced the improvement of electron cloud density on the surface of the $CsPbI_3$ perovskite, and thus the decreased surface tension can be obtained to stabilize $CsPbI_3$ grains in the cubic phase even in the micrometer scale, as shown in **Fig. 15c**. Meanwhile, the $CsPbI_3$ perovskite treated by PVP exhibited a long carrier diffusion length of 1.5 μm. After assembling this kind of $CsPbI_3$ perovskite into an IMH-PSC, a high PCE of 10.74% was obtained, as well as excellent thermal/moisture stability was demonstrated. In OMH perovskites, 2-dimentional (2D) OMH perovskites were very promising recently because they were demonstrated to have better stability than 3D OMH perovskites. Inspired by this phenomenon, Jiang *et al.* tried to add a small amount of phenylethylammonium iodide (PEA) into the $CsPbI_3$ precursor solution to induce reduced-dimensional perovskite formation, as shown in **Fig. 15d**.[184] Encouragingly, the resulting quasi-2D $CsPbI_3$ perovskites suppressed significantly the undesirable phase transition and thus reduced their defect densities. Meanwhile, in order to increase the precursor solubility, Jiang *et al.* used cesium acetate and hydrogen lead trihalide as the $CsPbI_3$ precursor, and thus the thickness of the $CsPbI_3$ perovskite film could be increased to 500 nm. Combining these two merits, the IMH-PSCs based on $CsPbI_3$ perovskites with the treatment of PEA showed a PCE as high as 12.4% and enhanced stability. Besides, Wang and coworkers incorporated choline iodine (CHI) into the $CsPbI_3$ perovskite to improve the corresponding IMH-PSC performance.[68] The additives of CHI not only passivated the surface trap states of $CsPbI_3$ perovskites, but also resulted in better matching of the energy levels at the interfaces between the $CsPbI_3$ perovskite and the HTM (and the ETM). Therefore, the PCEs of IMH-PSCs based on this kind of $CsPbI_3$ perovskites were improved to 18.4%, as shown in **Fig. 15e**. Meanwhile, the stability of this IMH-PSC was excellent. Besides introducing organic components into the $CsPbI_3$ perovskite to obtain a high PCE, it is worth emphasizing another contribution of this work here. It is well known that $CsPbI_3$ perovskites possess three kinds of black phases, including α-, β-, and γ-phases, and it has been demonstrated that α- and β-phase $CsPbI_3$ are prone to convert to γ-phase $CsPbI_3$ at room temperature. Therefore, it is hard to synthesize $CsPbI_3$ perovskites in α- and β-phase. In this work, Wang and coworkers synthesized $CsPbI_3$ perovskite in β-phase successfully by adjusting the precursor species and ratio, which showed a narrower band gap of 1.68 eV than the $CsPbI_3$ perovskite in γ-phase (1.73 eV), as shown in **Fig. 15f**. The results in this work indicate that most of the previously reported XRD patterns that have been incorrectly indexed to the α-$CsPbI_3$ phase are actually the γ-$CsPbI_3$ phase. Although these organic additives passivated the surface trap states and enhanced the PCE to a high level, most of them showed that the charge

lifetime of $CsPbI_3$ perovskites was in the range of 10-20 ns, suggesting that defects in $CsPbI_3$ perovskites were still severe. Therefore, in order to improve the quality of the $CsPbI_3$ perovskite, Yu *et al.* proposed a solution modification approach, in which the urea-ammonium thiocyanate (UAT) additive fully exploited the coordination activity of SCN^- for high-quality $CsPbI_3$ perovskite films.[185] This approach not only improved the $CsPbI_3$ perovskite film morphology, but also suppressed film defects and non-radiative charge recombination. As a result, the IMH-PSCs based on $CsPbI_3$ perovskites treated by UAT showed a PCE of over 20%. Moreover, this kind of PSC exhibited high operational stability with almost no PCE degradation after 1000 h working under continuous light illumination and bias voltage. In addition to the above mentioned organic additives, other additives were also tried for incorporation into $CsPbI_3$ perovskites to enhance their photovoltaic performances in IMH-PSCs, such as ethylenediamine, poly(ethylene glycol), etc.[186] All of them showed several advantages for high quality $CsPbI_3$ perovskite films, including uniform morphology, no pinhole, high crystallinity, low non-radiative recombination rate, suggesting that introducing organic additives is an effective method to improve the PCEs of $CsPbI_3$-based IMH-PSCs.

As mentioned above, the main cause for low performances of $CsPbI_3$-based IMH-PSCs is the stability of the lattice structure of the $CsPbI_3$ perovskite. Therefore, most works to study $CsPbI_3$-based IMH-PSCs focused on the $CsPbI_3$ perovskite itself, and only a handful of works focused on optimizing the architecture of $CsPbI_3$-based IMH-PSCs. Actually, it is also of paramount importance to study the architecture of $CsPbI_3$-based IMH-PSCs because the band structure of $CsPbI_3$ has a large difference with previously studied OMH perovskites.[187] Hence, the band structure of $CsPbI_3$ might have a large mismatch with that of the traditional ETMs/HTMs. Moreover, it is well known that the dopants in the traditional HTMs of spiro-OMeTAD can cause PSC instability. In order to resolve these problems, Yuan and coworkers proposed a new dopant-free polymer HTM of PTB7.[167] The $CsPbI_3$-based IMH-PSC with the new HTM of PTB7 showed efficient charge extraction and thus low V_{OC} loss. As a result, this kind of IMH-PSC showed a PCE as high as 12.55% and a V_{OC} as high as 1.27 V. Moreover, Yan and coworkers put forward a post-treatment process to compensate the band alignment mismatch.[188] In their method, they employed guanidine hydrobromide (GABr) to treat the $CsPbI_3$ layer and then formed a passivation layer on its surface. The characterization results indicated a lower nonradiative recombination rate and better band alignment between $CsPbI_3$ layer and the interface layer, which resulted in the decreased electron transport barrier for electron collection and superb hole contact for creating a driving force in hole transfer and preventing electrons from flowing in the opposite direction. As a result, the GABr-treated $CsPbI_3$-based IMH-PSCs exhibited a high PCE of 18.02%, which was significantly better than the original one (16.58%).

In order to make a clear comparison, the photovoltaic performances of the $CsPbI_3$-based IMH-PSCs are also listed in **Table 1**.[35,68,163-185,189-197] Clearly, this kind of IMH-PSC showed the highest PCE among all the IMH-PSCs due to the narrower bandgap of the $CsPbI_3$ perovskite. It is therefore promising to study it in the future, especially regarding its application in tandem cells.

As we mentioned in the Section 2.1, Pb is the best choice for B-site in perovskites so far, because the outermost electrons of the lead (Pb) cation hybridizing with the halogen anion p orbitals form the antibonding character of the valence band maximums of perovskites, which is important to achieve the high photovoltaic performance of PSCs. However, Pb is toxic. On the one hand, the maximum allowed Pb^{2+} concentration in air and water is set as 0.15 μg/L and 15 μg/L, respectively, according to the U.S. Environmental Protection Agency.[198-200] In addition, the harm of Pb^{2+} to the earth and human being is irreversible [198-200]. Therefore, researchers have explored Pb-free IMH-PSCs as environmentally-friendly alternatives.

Up to date, the Pb-free IMH perovskites can be divided into three categories, including group IV-based perovskites (e.g., $CsSnI_3$, $CsSnBr_3$), double perovskites (e.g., $CsAgBiBr_3$, $CsAgSbBr_3$), and perovskite derivatives (e.g., $Cs_3Bi_2I_9$, $Cs_3Sb_2I_9$).[201-204] $CsSnI_3$ is considered as the most promising candidate among them because of its isoelectronic structure with Pb, suitable bandgap, high intrinsic charge carrier mobility, and highest photovoltaic performance among all kinds of Pb-free perovskites. However, when compared with the Pb-based IMH perovskites, all the reported $CsSnI_3$ solar cells in the literature have so far shown inferior photovoltaic performances. The main reason can be ascribed to the low formation energy of Sn vacancies, which leads to excessive p-doping in Sn-based perovskites.[205] Recently, several works have reported the performance improvement of the $CsSnI_3$-based IMH PSCs. Composition engineering is an effective method to improve photovoltaic performance in organic-inorganic lead halide perovskites, and Chen and coworkers employed this method into $CsSnI_3$ perovskites to propose the cesium tin-germanium triiodide ($CsSn_{0.5}Ge_{0.5}I_3$) perovskite film as the light absorber in the IMH-PSCs.[206] When the Ge element was introduced into $CsSnI_3$ films, a native-oxide layer was formed on the surface of $CsSn_{0.5}Ge_{0.5}I_3$, which exhibited enhanced stability. Meanwhile, the carrier lifetime and carrier diffusion coefficient of $CsSn_{0.5}Ge_{0.5}I_3$ were also increased when compared with the pristine $CsSnI_3$. As a result, the PCE of $CsSn_{0.5}Ge_{0.5}I_3$-based PSCs was improved to 7.11%, which was much higher than the $CsSnI_3$-based control PSCs (1.7%). Besides the addition of inorganic cations into the precursor solution, incorporation of some organic functional groups also helps enhance the photovoltaic performance of the IMH-PSC. These functional groups can make strong coordination interaction with defects, which enhances the electron density around Sn^{2+} and protects it from oxidation to Sn^{4+}, leading to a better film morphology, lower defect density, and higher optical absorption. In another recent study, Ye and coworkers incorporated *N,N'*-methylenebis(acrylamide) (MBAA) into the $CsSnI_3$ layer.[207] The lone electron pairs of -NH and -CO units of MBAA were designed to form coordination bonding with Sn^{2+} in the $CsSnI_3$ layer, leading to a reduced Sn^{4+} density and better stability, and finally the PCE of the $CsSnI_3$-based IMH-PSC was improved to 7.5%. Overall, the PCE of the $CsSnI_3$-based IMH-PSC exhibits a marked enhancement when compared with its initial performance. The study on the $CsSnI_3$-based IMH-PSCs is still in its infancy, and it can be expected that the performance of the $CsSnI_3$-based IMH-PSC will be further enhanced in the near future.

4 Conclusion and outlook

PSCs have experienced an unprecedent success in the past twelve years. The record PCE of the OMH-PSC has increased from an initial value of 3.8% to the recent value of 25.5%. However, the

stability of OMH perovskites is still a challenge for their commercialization. IMH perovskites are considered as promising candidates to resolve this issue, especially the stability at high temperature. With the investigation of IMH perovskites, several challenges emerge and need to be resolved, e.g., improving the PCE, narrowing the bandgap, preparing novel ETMs/HTMs, etc. Below, some vital aspects are listed.

$CsPbBr_3$-based IMH-PSCs exhibited the best stability property among all kinds of IMH-PSCs so far. However, their photovoltaic performances were still lower than other kinds of IMH-PSCs although the PCE has almost been doubled to 10.91% by Jiang, Qi and coworkers [100] since the first report emerged in 2015 [77]. The main challenge and critical issue faced by $CsPbBr_3$-based IMH-PSCs is still the large bandgap of $CsPbBr_3$ of 2.3 eV. In order to push $CsPbBr_3$-based IMH-PSCs to commercialization, three possible options can be adopted in future. First, according to the Shockley-Queisser efficiency limit (S-Q limit) mode, the highest PCE and V_{OC} of the $CsPbBr_3$-based IMH-PSCs can reach ~16.5% and ~1.9 V, respectively.[208] Therefore, there is still plenty of room to improve for enhancing the PCE of the $CsPbBr_3$-based IMH-PSC. The strategies include reducing the defect density, boosting the uniformity of the $CsPbBr_3$ perovskite film, decreasing the non-radiative recombination rate and so on. Second, as mentioned above, the CBM of $CsPbBr_3$ consists of antibonding mixing of Pb 6p and Br 5p orbitals, and the VBM is mainly determined by antibonding hybridized Pb 6s and Br 5p orbitals. Therefore, it is possible to narrow the bandgap of the $CsPbBr_3$ perovskite by composition engineering at the Pb-site and Br-site. As we know, narrowing the bandgap by adjusting the Br-site composition has already been realized so far, e.g., $CsPb(Br_xI_{1-x})_3$ perovskites. However, there is no report on changing the bandgap by adjusting the Pb-site composition. Therefore, it is an opportunity to narrow the bandgap of $CsPbBr_3$ by this method. Finally, $CsPbBr_3$-based IMH-PSCs can only utilize the sunlight below 540 nm because of the large bandgap of $CsPbBr_3$ (2.3 eV). In order to enhance its light harvesting ability, a possible way is to assemble the $CsPbBr_3$-based IMH-PSC into a three-junction tandem cell. Till now, there is no report on this kind of device. Therefore, developing three-junction tandem solar cells based on $CsPbBr_3$-based IMH-PSCs with other solar cells, such as the other kinds of PSCs, Si-based solar cells, CIGS solar cells, and so on, may be worth further investigations in the future.

As for $CsPb(Br_xI_{1-x})_3$-based IMH-PSCs, the better light harvesting ability than $CsPbBr_3$-based IMH-PSCs and the better stability property than $CsPbI_3$-based IMH-PSCs make them a promising candidate in large-scale applications. However, their photovoltaic performances are not satisfactory when compared with OMH-PSCs. For $CsPbBr_2I$-based IMH-PSCs, the bandgap of $CsPbBr_2I$ (~2.0 eV) is much smaller than that of $CsPbBr_3$, while the highest efficiency of $CsPbBr_2I$-based IMH-PSCs (11.53%) is slightly higher than that of $CsPbBr_3$-based IMH-PSCs. For $CsPbBrI_2$-based IMH-PSCs, the bandgap of ~1.85 eV can result in a highest PCE of ~22% in theory, while the highest PCE that has been obtained so far is ~17%.[134,209] Therefore, enhancing the PCE of the $CsPb(Br_xI_{1-x})_3$-based IMH-PSC is a primary task in the near future. Moreover, different from the $CsPbBr_3$ perovskites, it is easier to change the bandgap of the $CsPb(Br_xI_{1-x})_3$ perovskite by adjusting the Pb-site composition. For example, the bandgap of the $CsPbBr_2I$ perovskite was reduced to 1.85 eV when partial Pb^{2+} was replaced by Mn^{2+}.[124] However, the efficiency was still relative lower considering such a low bandgap. Thus it is necessary to make further efforts on enhancing the PCE of the $CsPb(Br_xI_{1-x})_3$-based IMH-PSCs.

Finally, similarly to the $CsPbBr_3$-based IMH-PSCs, in order to maximize the utilization of sunlight, $CsPb(Br_xI_{1-x})_3$-based IMH-PSCs can also be integrated into a tandem cell as the front cell.

$CsPbI_3$-based IMH-PSCs showed the highest possibility in the commercialization because they exhibited the lowest bandgap and highest PCE of exceeding 20% among all kinds of $CsPbX_3$-based IMH-PSCs. Compared with the early studies in which $CsPbI_3$ perovskite converted to yellow-phase immediately when exposed to air, the stability of the $CsPbI_3$ perovskite in recent studies has made a big advance. However, it is still far from the required stability for commercialization. Therefore, stabilizing the $CsPbI_3$ perovskite, especially stabilizing it from the intrinsic lattice structure, is still the primary task in the near future. Moreover, according to the S-Q limit, the ideal bandgap for a light absorber is ~1.3 eV, which is still smaller than that of the $CsPbI_3$ perovskite.[210] Therefore, it is also necessary to make efforts to narrow the bandgap of the $CsPbI_3$ perovskite. As mentioned above, it is possible to achieve the narrow bandgap by composition engineering on the Pb-site and/or I-site. However, only a handful of reported works can achieve this on the $CsPbI_3$ perovskite till now.[172] Therefore, similar to $CsPbBr_3$ perovskites, narrowing the bandgap and then obtaining a bandgap close to 1.3 eV for $CsPbI_3$ perovskites is of importance. Meanwhile, as mentioned above, the $CsPbI_3$ perovskite in α-phase had the lower bandgap than the other two black phases, however, it has not been achieved experimentally up to date. Therefore, achieving the $CsPbI_3$ perovskite in α-phase is also a future task . Certainly, similar to the $CsPbBr_3$- and $CsPb(Br_xI_{1-x})_3$-based IMH-PSCs, the $CsPbI_3$-based IMH-PSCs can also be employed into tandem cells to maximize the utilization of sunlight.

In general, the studies of the three kinds of IMH-PSCs are still in the early stage. Although a big advance has been made on improving the film synthesis methods, most of the mechanisms concerning their electronic structure and photovoltaic properties are still lacking, which are of importance for their applications in solar cells as this information can give us rational guidelines to improve their PCEs. Therefore, much more experimental and theoretical research efforts should be devoted in future to understand the electronic structure, interfacial charge recombination and the relationship between the lattice structure and stability in $CsPbX_3$-based IMH-PSCs. Moreover, all of $CsPbX_3$ perovskites display different band structures from traditional OMH perovskites. This implies that their CBMs and VBMs have a large shift when compared with OMH perovskites. It is well known that the current ETMs and HTMs are optimized for OMH perovskites. Therefore, they are not the best choices for the $CsPbX_3$ perovskite. For example, the V_{OC}s for all of the reported $CsPbBr_3$-based IMH-PSCs were in the range of 1.2-1.5 V, with E_{loss} ($E_{loss} = E_g - eV_{OC}$) higher than 0.8 eV. However, E_{loss} has been reduced to ~0.4 eV in OMH-PSCs. One of the main reasons is the band structure mismatch between $CsPbX_3$ perovskites and ETMs/HTMs. Therefore, exploring new ETMs and HTMs with better energy level alignment with IMH perovskites is vital as well for the development of $CsPbX_3$-based IMH-PSCs. Last but not the least, the research of Pb-based IMH perovskites is still the mainstream currently, which, however, is toxic and harmful for our health and environment. Non-toxic lead-free IMH perovskites with good properties are preferable. Recently, PSCs based on lead-free IMH perovskites have been studied, however, the performance was not high and more efforts are still needed in future.

Overall, although the photovoltaic performances of $CsPbX_3$-based IMH-PSCs are still lower than those of OMH-PSCs, the development of the $CsPbX_3$-based IMH-PSC is spectacular in the past few years. More future theoretical and experimental research efforts will help realize more efficient and stable $CsPbX_3$-based IMH-PSCs.

Declaration of competing interest

The authors declare that they have no known competing financial interests or personal relationships that could have appeared to influence the work reported in this paper.

Acknowledgments

J. L. acknowledges the funding support from the Research Grant of Fudan University, China (No. IDH2021070), and the Natural Science Foundation of Shanghai (Grant Number 21ZR1404900). Y. B. Q. acknowledges the support from the Energy Materials and Surface Sciences Unit of the Okinawa Institute of Science and Technology Graduate University.

References

[1] A. Kojima, K. Teshima, Y. Shirai, T. Miyasaka, Organometal Halide Perovskites as Visible-Light Sensitizers for Photovoltaic Cells, J. Am. Chem. Soc. 131 (2009) 6050-6051.
[2] J. Burschka, N. Pellet, S.-J. Moon, R. Humphry-Baker, P. Gao, M.K. Nazeeruddin, M. Graetzel, Sequential deposition as a route to high-performance perovskite-sensitized solar cells, Nature 499 (2013) 316-319.
[3] N. Ahn, D.-Y. Son, I.-H. Jang, S.M. Kang, M. Choi, N.-G. Park, Highly Reproducible Perovskite Solar Cells with Average Efficiency of 18.3% and Best Efficiency of 19.7% Fabricated via Lewis Base Adduct of Lead(II) Iodide, J. Am. Chem. Soc. 137 (2015) 8696-8699.
[4] Q. Chen, H. Zhou, Z. Hong, S. Luo, H.-S. Duan, H.-H. Wang, Y. Liu, G. Li, Y. Yang, Planar Heterojunction Perovskite Solar Cells via Vapor-Assisted Solution Process, J. Am. Chem. Soc. 136 (2014) 622-625.
[5] W. Chen, Y. Wu, Y. Yue, J. Liu, W. Zhang, X. Yang, H. Chen, E. Bi, I. Ashraful, M. Graetzel, L. Han, Efficient and stable large-area perovskite solar cells with inorganic charge extraction layers, Science 350 (2015) 944-948.
[6] D.W. deQuilettes, S.M. Vorpahl, S.D. Stranks, H. Nagaoka, G.E. Eperon, M.E. Ziffer, H.J. Snaith, D.S. Ginger, Impact of microstructure on local carrier lifetime in perovskite solar cells, Science 348 (2015) 683-686.
[7] Q. Dong, Y. Fang, Y. Shao, P. Mulligan, J. Qiu, L. Cao, J. Huang, Electron-hole diffusion lengths > 175 mu m in solution-grown $CH_3NH_3PbI_3$ single crystals, Science 347 (2015) 967-970.
[8] C. Eames, J.M. Frost, P.R.F. Barnes, B.C. O'Regan, A. Walsh, M.S. Islam, Ionic transport in hybrid lead iodide perovskite solar cells, Nat. Commun. 6 (2015) 7497.
[9] M.A. Green, A. Ho-Baillie, H.J. Snaith, The emergence of perovskite solar cells, Nat. Photon. 8 (2014) 506-514.
[10] Z. Guo, Y. Wan, M. Yang, J. Snaider, K. Zhu, L. Huang, Long-range hot-carrier transport in hybrid perovskites visualized by ultrafast microscopy, Science 356 (2017) 59-62.

[11] L. Han, Improved charge carrying for solar cells, Nature 567 (2019) 465-467.
[12] J. Hieulle, C. Stecker, R. Ohmann, L.K. Ono, Y. B. Qi, Scanning Probe Microscopy Applied to Organic-Inorganic Halide Perovskite Materials and Solar Cells, Small Methods 2 (2018) 1700295.
[13] Y. Jiang, L. Qiu, E.J. Juarez-Perez, L.K. Ono, Z. Hu, Z. Liu, Z. Wu, L. Meng, Q. Wang, Y. B. Qi, Reduction of lead leakage from damaged lead halide perovskite solar modules using self-healing polymer-based encapsulation, Nat. Energy 4 (2019) 585-593.
[14] E.J. Juarez-Perez, Z. Hawash, S.R. Raga, L.K. Ono, Y. B. Qi, Thermal degradation of $CH_3NH_3PbI_3$ perovskite into NH_3 and CH_3I gases observed by coupled thermogravimetry-mass spectrometry analysis, Energy Environ. Sci. 9 (2016) 3406-3410.
[15] L.K. Ono, Y. B. Qi, S. Liu, Progress toward Stable Lead Halide Perovskite Solar Cells, Joule 2 (2018) 1961-1990.
[16] D. Shi, V. Adinolfi, R. Comin, M. Yuan, E. Alarousu, A. Buin, Y. Chen, S. Hoogland, A. Rothenberger, K. Katsiev, Y. Losovyj, X. Zhang, P.A. Dowben, O.F. Mohammed, E.H. Sargent, O.M. Bakr, Low trap-state density and long carrier diffusion in organolead trihalide perovskite single crystals, Science 347 (2015) 519-522.
[17] S.D. Stranks, G.E. Eperon, G. Grancini, C. Menelaou, M.J.P. Alcocer, T. Leijtens, L.M. Herz, A. Petrozza, H.J. Snaith, Electron-Hole Diffusion Lengths Exceeding 1 Micrometer in an Organometal Trihalide Perovskite Absorber, Science 342 (2013) 341-344.
[18] J. Tong, Z. Song, D.H. Kim, X. Chen, C. Chen, A.F. Palmstrom, P.F. Ndione, M.O. Reese, S.P. Dunfield, O.G. Reid, J. Liu, F. Zhang, S.P. Harvey, Z. Li, S.T. Christensen, G. Teeter, D. Zhao, M.M. Al-Jassim, M.F.A.M. van Hest, M.C. Beard, S.E. Shaheen, J.J. Berry, Y. Yan, K. Zhu, Carrier lifetimes of > 1 μs in Sn-Pb perovskites enable efficient all-perovskite tandem solar cells, Science 364 (2019) 475-479.
[19] G. Xing, N. Mathews, S. Sun, S.S. Lim, Y.M. Lam, M. Graetzel, S. Mhaisalkar, T.C. Sum, Long-Range Balanced Electron- and Hole-Transport Lengths in Organic-Inorganic $CH_3NH_3PbI_3$, Science 342 (2013) 344-347.
[20] S. Bai, P. Da, C. Li, Z. Wang, Z. Yuan, F. Fu, M. Kawecki, X. Liu, N. Sakai, J.T.-W. Wang, S. Huettner, S. Buecheler, M. Fahlman, F. Gao, H.J. Snaith, Planar perovskite solar cells with long-term stability using ionic liquid additives, Nature 571 (2019) 245-250.
[21] H. Chen, F. Ye, W. Tang, J. He, M. Yin, Y. Wang, F. Xie, E. Bi, X. Yang, M. Gratzel, L. Han, A solvent- and vacuum-free route to large-area perovskite films for efficient solar modules, Nature 550 (2017) 92-95.
[22] J.-P. Correa-Baena, M. Saliba, T. Buonassisi, M. Graetzel, A. Abate, W. Tress, A. Hagfeldt, Promises and challenges of perovskite solar cells, Science 358 (2017) 739-744.
[23] G.E. Eperon, S.D. Stranks, C. Menelaou, M.B. Johnston, L.M. Herz, H.J. Snaith, Formamidinium lead trihalide: a broadly tunable perovskite for efficient planar heterojunction solar cells, Energy Environ. Sci. 7 (2014) 982-988.
[24] M. Graetzel, The light and shade of perovskite solar cells, Nat. Mater. 13 (2014) 838-842.
[25] J.H. Heo, S.H. Im, J.H. Noh, T.N. Mandal, C.-S. Lim, J.A. Chang, Y.H. Lee, H.-j. Kim, A. Sarkar, M.K. Nazeeruddin, M. Graetzel, S.I. Seok, Efficient inorganic-organic hybrid heterojunction solar cells containing perovskite compound and polymeric hole conductors, Nat. Photon. 7 (2013) 487-492.

[26] N.J. Jeon, J.H. Noh, Y.C. Kim, W.S. Yang, S. Ryu, S.I. Seok, Solvent engineering for high-performance inorganic-organic hybrid perovskite solar cells, Nat. Mater. 13 (2014) 897-903.
[27] Q. Jiang, Y. Zhao, X. Zhang, X. Yang, Y. Chen, Z. Chu, Q. Ye, X. Li, Z. Yin, J. You, Surface passivation of perovskite film for efficient solar cells, Nat. Photon. 13 (2019) 460-466.
[28] E.J. Juarez-Perez, L.K. Ono, M. Maeda, Y. Jiang, Z. Hawash, Y. B. Qi, Photodecomposition and thermal decomposition in methylammonium halide lead perovskites and inferred design principles to increase photovoltaic device stability, J. Mater. Chem. A 6 (2018) 9604-9612.
[29] L.K. Ono, Y. B. Qi, Research progress on organic-inorganic halide perovskite materials and solar cells, J. Phys. D Appl. Phys. 51 (2018) 093001.
[30] D. Mierwaldt, V. Roddatis, M. Risch, J. Scholz, J. Geppert, M.E. Abrishami, C. Jooss, Environmental TEM Investigation of Electrochemical Stability of Perovskite and Ruddlesden–Popper Type Manganite Oxygen Evolution Catalysts, Adv. Sustain. Syst. 1 (2017) 1700109.
[31] S. Wang, Y. Jiang, E.J. Juarez-Perez, L.K. Ono, Y. B. Qi, Accelerated degradation of methylammonium lead iodide perovskites induced by exposure to iodine vapour, Nat. Energy 2 (2017) 16195.
[32] W.-J. Yin, T. Shi, Y. Yan, Unusual defect physics in $CH_3NH_3PbI_3$ perovskite solar cell absorber, Appl. Phys. Lett. 104 (2014) 063903.
[33] M. Saliba, T. Matsui, K. Domanski, J.-Y. Seo, A. Ummadisingu, S.M. Zakeeruddin, J.-P. Correa-Baena, W.R. Tress, A. Abate, A. Hagfeldt, M. Gratzel, Incorporation of rubidium cations into perovskite solar cells improves photovoltaic performance, Science 354 (2016) 206-209.
[34] M. Saliba, T. Matsui, J.-Y. Seo, K. Domanski, J.-P. Correa-Baena, M.K. Nazeeruddin, S.M. Zakeeruddin, W. Tress, A. Abate, A. Hagfeldt, M. Gratzel, Cesium-containing triple cation perovskite solar cells: improved stability, reproducibility and high efficiency, Energy Environ. Sci. 9 (2016) 1989-1997.
[35] H. Choi, J. Jeong, H.-B. Kim, S. Kim, B. Walker, G.-H. Kim, J.Y. Kim, Cesium-doped methylammonium lead iodide perovskite light absorber for hybrid solar cells, Nano Energy 7 (2014) 80-85.
[36] C. Yi, J. Luo, S. Meloni, A. Boziki, N. Ashari-Astani, C. Grätzel, S.M. Zakeeruddin, U. Röthlisberger, M. Grätzel, Entropic stabilization of mixed A-cation ABX_3 metal halide perovskites for high performance perovskite solar cells, Energy Environ. Sci. 9 (2016) 656-662.
[37] J.-W. Lee, D.-H. Kim, H.-S. Kim, S.-W. Seo, S.M. Cho, N.-G. Park, Formamidinium and Cesium Hybridization for Photo- and Moisture-Stable Perovskite Solar Cell, Adv. Energy Mater. 5 (2015) 1501310.
[38] A. Swarnkar, A.R. Marshall, E.M. Sanehira, B.D. Chernomordik, D.T. Moore, J.A. Christians, T. Chakrabarti, J.M. Luther, Quantum dot-induced phase stabilization of alpha-$CsPbI_3$ perovskite for high-efficiency photovoltaics, Science 354 (2016) 92-95.
[39] G. Tong, T. Chen, H. Li, W. Song, Y. Chang, J. Liu, L. Yu, J. Xu, Y. B. Qi, Y. Jiang, High Efficient Hole Extraction and Stable All-Bromide Inorganic Perovskite Solar Cells via Derivative-Phase Gradient Bandgap Architecture, Solar RRL 3 (2019) 1900030.
[40] G. Tong, L.K. Ono, Y. B. Qi, Recent Progress of All-Bromide Inorganic Perovskite Solar Cells, Energy Technol. 8 (2020).
[41] W. Chen, X. Li, Y. Li, Y. Li, A review: crystal growth for high-performance all-inorganic perovskite solar cells, Energy Environ. Sci. 13 (2020) 1971-1996.

[42] N.A.N. Ouedraogo, Y. Chen, Y.Y. Xiao, Q. Meng, C.B. Han, H. Yan, Y. Zhang, Stability of all-inorganic perovskite solar cells, Nano Energy 67 (2020) 104249.
[43] W. Xiang, W. Tress, Review on Recent Progress of All-Inorganic Metal Halide Perovskites and Solar Cells, Adv. Mater. 31 (2019) 1902851.
[44] J. Chen, W.C.H. Choy, Efficient and Stable All-Inorganic Perovskite Solar Cells, Solar RRL 4 (2020) 2000408.
[45] J. Zhang, G. Hodes, Z. Jin, S. Liu, All-Inorganic $CsPbX_3$ Perovskite Solar Cells: Progress and Prospects, Angew. Chem. Int. Ed. 58 (2019) 15596-15618.
[46] H. Chen, S. Xiang, W. Li, H. Liu, L. Zhu, S. Yang, Inorganic Perovskite Solar Cells: A Rapidly Growing Field, Solar RRL 2 (2018) 1700188.
[47] J. Liang, J. Liu, Z. Jin, All-Inorganic Halide Perovskites for Optoelectronics: Progress and Prospects, Solar RRL 1 (2017) 1700086.
[48] T. Cai, J. Wang, W. Li, K. Hills-Kimball, H. Yang, Y. Nagaoka, Y. Yuan, R. Zia, O. Chen, Mn^{2+}/Yb^{3+} Codoped $CsPbCl_3$ Perovskite Nanocrystals with Triple-Wavelength Emission for Luminescent Solar Concentrators, Adv. Sci. 7 (2020) 2001317.
[49] J. Yang, X. Yuan, L. Fan, Y. Zheng, F. Ma, H. Li, J. Zhao, H. Liu, Enhancing Mn Emission of $CsPbCl_3$ Perovskite Nanocrystals via Incorporation of Rubidium Ions, Mater. Res. Bull. 133 (2021) 111080.
[50] X. Zhang, B. Xu, J. Zhang, Y. Gao, Y. Zheng, K. Wang, X.W. Sun, All-Inorganic Perovskite Nanocrystals for High-Efficiency Light Emitting Diodes: Dual-Phase $CsPbBr_3$-$CsPb_2Br_5$ Composites, Adv. Funct. Mater. 26 (2016) 4595-4600.
[51] N. Yantara, S. Bhaumik, F. Yan, D. Sabba, H.A. Dewi, N. Mathews, P.P. Boix, H.V. Demir, S. Mhaisalkar, Inorganic Halide Perovskites for Efficient Light-Emitting Diodes, J. Phys. Chem. Lett. 6 (2015) 4360-4364.
[52] H.-C. Wang, S.-Y. Lin, A.-C. Tang, B.P. Singh, H.-C. Tong, C.-Y. Chen, Y.-C. Lee, T.-L. Tsai, R.-S. Liu, Mesoporous Silica Particles Integrated with All-Inorganic $CsPbBr_3$ Perovskite Quantum-Dot Nanocomposites (MP-PQDs) with High Stability and Wide Color Gamut Used for Backlight Display, Angew. Chem. Int. Ed. 55 (2016) 7924-7929.
[53] J. Li, L. Xu, T. Wang, J. Song, J. Chen, J. Xue, Y. Dong, B. Cai, Q. Shan, B. Han, H. Zeng, 50-Fold EQE Improvement up to 6.27% of Solution-Processed All-Inorganic Perovskite $CsPbBr_3$ QLEDs via Surface Ligand Density Control, Adv. Mater. 29 (2017) 1603885.
[54] W. Ahmad, J. Khan, G. Niu, J. Tang, Inorganic $CsPbI_3$ Perovskite-Based Solar Cells: A Choice for a Tandem Device, Solar RRL 1 (2017) 1700048.
[55] L. Protesescu, S. Yakunin, M.I. Bodnarchuk, F. Krieg, R. Caputo, C.H. Hendon, R.X. Yang, A. Walsh, M.V. Kovalenko, Nanocrystals of Cesium Lead Halide Perovskites ($CsPbX_3$, X = Cl, Br, and I): Novel Optoelectronic Materials Showing Bright Emission with Wide Color Gamut, Nano Lett. 15 (2015) 3692-3696.
[56] J. Song, J. Li, X. Li, L. Xu, Y. Dong, H. Zeng, Quantum Dot Light-Emitting Diodes Based on Inorganic Perovskite Cesium Lead Halides ($CsPbX_3$), Adv. Mater. 27 (2015) 7162-7167.
[57] Z. Wang, Y. Wang, Z. Nie, Y. Ren, H. Zeng, Laser induced ion migration in all-inorganic mixed halide perovskite micro-platelets, Nanoscale Adv. 1 (2019) 4459-4465.

[58] H. Zhang, X. Fu, Y. Tang, H. Wang, C. Zhang, W.W. Yu, X. Wang, Y. Zhang, M. Xiao, Phase segregation due to ion migration in all-inorganic mixed-halide perovskite nanocrystals, Nat. Commun. 10 (2019) 1088.
[59] T. Atsue, I.B. Ogunniranye, O.E. Oyewande, Investigation of material properties of halide mixed lead - Free double perovskite for optoelectronic applications using first-principles study, Mater. Sci. Semicon. Proc. 133 (2021) 105963.
[60] A. Surendran, X. Yu, R. Begum, Y. Tao, Q.J. Wang, W.L. Leong, All Inorganic Mixed Halide Perovskite Nanocrystal–Graphene Hybrid Photodetector: From Ultrahigh Gain to Photostability, ACS Appl. Mater. Interfaces 11 (2019) 27064-27072.
[61] J. Li, Q. Yu, Y. He, C.C. Stoumpos, G. Niu, G.G. Trimarchi, H. Guo, G. Dong, D. Wang, L. Wang, M.G. Kanatzidis, $Cs_2PbI_2Cl_2$, All-Inorganic Two-Dimensional Ruddlesden–Popper Mixed Halide Perovskite with Optoelectronic Response, J. Am. Chem. Soc. 140 (2018) 11085-11090.
[62] A.K. Jena, A. Kulkarni, T. Miyasaka, Halide Perovskite Photovoltaics: Background, Status, and Future Prospects, Chem. Rev. 119 (2019) 3036-3103.
[63] J. Shamsi, A.S. Urban, M. Imran, L. De Trizio, L. Manna, Metal Halide Perovskite Nanocrystals: Synthesis, Post-Synthesis Modifications, and Their Optical Properties, Chem. Rev. 119 (2019) 3296-3348.
[64] D. Ji, S. Feng, L. Wang, S. Wang, M. Na, H. Zhang, C. Zhang, X. Li, Regulatory tolerance and octahedral factors by using vacancy in $APbI_3$ perovskites, Vacuum, 164 (2019) 186-193.
[65] A. Dutta, N. Pradhan, Phase-Stable Red-Emitting $CsPbI_3$ Nanocrystals: Successes and Challenges, ACS Energy Lett. 4 (2019) 709-719.
[66] F. Bertolotti, L. Protesescu, M.V. Kovalenko, S. Yakunin, A. Cervellino, S.J.L. Billinge, M.W. Terban, J.S. Pedersen, N. Masciocchi, A. Guagliardi, Coherent Nanotwins and Dynamic Disorder in Cesium Lead Halide Perovskite Nanocrystals, ACS Nano 11 (2017) 3819-3831.
[67] V.K. Ravi, G.B. Markad, A. Nag, Band Edge Energies and Excitonic Transition Probabilities of Colloidal $CsPbX_3$ (X = Cl, Br, I) Perovskite Nanocrystals, ACS Energy Lett. 1 (2016) 665-671.
[68] Y. Wang, M.I. Dar, L.K. Ono, T. Zhang, M. Kan, Y. Li, L. Zhang, X. Wang, Y. Yang, X. Gao, Y. B. Qi, M. Grätzel, Y. Zhao, Thermodynamically stabilized β-$CsPbI_3$–based perovskite solar cells with efficiencies >18%, Science 365 (2019) 591-595.
[69] J. Hieulle, S. Luo, D.-Y. Son, A. Jamshaid, C. Stecker, Z. Liu, G. Na, D. Yang, R. Ohmann, L.K. Ono, L. Zhang, Y. B. Qi, Imaging of the Atomic Structure of All-Inorganic Halide Perovskites, J. Phys. Chem. Lett. 11 (2020) 818-823.
[70] C.C. Stoumpos, C.D. Malliakas, J.A. Peters, Z. Liu, M. Sebastian, J. Im, T.C. Chasapis, A.C. Wibowo, D.Y. Chung, A.J. Freeman, B.W. Wessels, M.G. Kanatzidis, Crystal Growth of the Perovskite Semiconductor $CsPbBr_3$: A New Material for High-Energy Radiation Detection, Cryst. Growth Des. 13 (2013) 2722-2727.
[71] J. Song, Q. Cui, J. Li, J. Xu, Y. Wang, L. Xu, J. Xue, Y. Dong, T. Tian, H. Sun, H. Zeng, Ultralarge All-Inorganic Perovskite Bulk Single Crystal for High-Performance Visible–Infrared Dual-Modal Photodetectors, Adv. Opt. Mater. 5 (2017) 1700157.
[72] H. Zhu, M.T. Trinh, J. Wang, Y. Fu, P.P. Joshi, K. Miyata, S. Jin, X.-Y. Zhu, Organic Cations Might Not Be Essential to the Remarkable Properties of Band Edge Carriers in Lead Halide Perovskites, Adv. Mater. 29 (2017) 1603072.

[73] E.M. Hutter, R.J. Sutton, S. Chandrashekar, M. Abdi-Jalebi, S.D. Stranks, H.J. Snaith, T.J. Savenije, Vapour-Deposited Cesium Lead Iodide Perovskites: Microsecond Charge Carrier Lifetimes and Enhanced Photovoltaic Performance, ACS Energy Lett. 2 (2017) 1901-1908.
[74] S. Dastidar, S. Li, S.Y. Smolin, J.B. Baxter, A.T. Fafarman, Slow Electron–Hole Recombination in Lead Iodide Perovskites Does Not Require a Molecular Dipole, ACS Energy Lett. 2 (2017) 2239-2244.
[75] C.L. Kennedy, A.H. Hill, E.S. Massaro, E.M. Grumstrup, Ultrafast Excited-State Transport and Decay Dynamics in Cesium Lead Mixed Halide Perovskites, ACS Energy Lett. 2 (2017) 1501-1506.
[76] X. Li, Y. Wu, S. Zhang, B. Cai, Y. Gu, J. Song, H. Zeng, $CsPbX_3$ Quantum Dots for Lighting and Displays: Room-Temperature Synthesis, Photoluminescence Superiorities, Underlying Origins and White Light-Emitting Diodes, Adv. Funct. Mater. 26 (2016) 2435-2445.
[77] M. Kulbak, D. Cahen, G. Hodes, How Important Is the Organic Part of Lead Halide Perovskite Photovoltaic Cells? Efficient $CsPbBr_3$ Cells, J. Phys. Chem. Lett. 6 (2015) 2452-2456.
[78] M. Kulbak, S. Gupta, N. Kedem, I. Levine, T. Bendikov, G. Hodes, D. Cahen, Cesium Enhances Long-Term Stability of Lead Bromide Perovskite-Based Solar Cells, J. Phys. Chem. Lett. 7 (2016) 167-172.
[79] C. Cetin, P. Chen, M. Hao, D. He, Y. Bai, M. Lyu, J.-H. Yun, L. Wang, Inorganic p-Type Semiconductors as Hole Conductor Building Blocks for Robust Perovskite Solar Cells, Adv. Sustain. Syst. 2 (2018) 1800032.
[80] N. Arora, M.I. Dar, A. Hinderhofer, N. Pellet, F. Schreiber, S.M. Zakeeruddin, M. Graetzel, Perovskite solar cells with CuSCN hole extraction layers yield stabilized efficiencies greater than 20%, Science 358 (2017) 768-771.
[81] Z. Hawash, L.K. Ono, Y. B. Qi, Recent Advances in spiro-MeOTAD Hole Transport Material and Its Applications in Organic-Inorganic Halide Perovskite Solar Cells, Adv. Mater. Interfaces 5 (2018) 1700623.
[82] L.K. Ono, S.R. Raga, M. Remeika, A.J. Winchester, A. Gabe, Y. B. Qi, Pinhole-free hole transport layers significantly improve the stability of $MAPbI_3$-based perovskite solar cells under operating conditions, J. Mater. Chem. A 3 (2015) 15451-15456.
[83] G. You, L. Liu, J. Wang, M. Zhao, C. Zhao, X. Cai, J. Tang, F. Lu, T. Jiu, Tris(pentafluorophenyl)borane-Modified P3CT-K as an Efficient Hole-Transport Layer for Inverted Planar $MAPbI_3$ Perovskite Solar Cells, Adv. Sustain. Syst. 5 (2021) 2100107.
[84] J. Liang, C. Wang, Y. Wang, Z. Xu, Z. Lu, Y. Ma, H. Zhu, Y. Hu, C. Xiao, X. Yi, G. Zhu, H. Lv, L. Ma, T. Chen, Z. Tie, Z. Jin, J. Liu, All-Inorganic Perovskite Solar Cells, J. Am. Chem. Soc. 138 (2016) 15829-15832.
[85] J. Liang, C. Wang, Y. Wang, Z. Xu, Z. Lu, Y. Ma, H. Zhu, Y. Hu, C. Xiao, X. Yi, G. Zhu, H. Lv, L. Ma, T. Chen, Z. Tie, Z. Jin, J. Liu, Correction to “All-Inorganic Perovskite Solar Cells”, J. Am. Chem. Soc. 139 (2017) 2852-2852.
[86] W. Nie, H. Tsai, R. Asadpour, J.-C. Blancon, A.J. Neukirch, G. Gupta, J.J. Crochet, M. Chhowalla, S. Tretiak, M.A. Alam, H.-L. Wang, A.D. Mohite, High-efficiency solution-processed perovskite solar cells with millimeter-scale grains, Science 347 (2015) 522-525.

[87] C. Stecker, K. Liu, J. Hieulle, R. Ohmann, Z. Liu, L.K. Ono, G. Wang, Y. B. Qi, Surface Defect Dynamics in Organic-Inorganic Hybrid Perovskites: From Mechanism to Interfacial Properties, ACS Nano 13 (2019) 12127-12136.
[88] J.J. Yoo, G. Seo, M.R. Chua, T.G. Park, Y. Lu, F. Rotermund, Y.-K. Kim, C.S. Moon, N.J. Jeon, J.-P. Correa-Baena, V. Bulovic, S.S. Shin, M.G. Bawendi, J. Seo, Efficient perovskite solar cells via improved carrier management, Nature 590 (2021), 587-593.
[89] R. Garai, M.A. Afroz, R.K. Gupta, P.K. Iyer, Efficient Trap Passivation of $MAPbI_3$ via Multifunctional Anchoring for High-Performance and Stable Perovskite Solar Cells, Adv. Sustain. Syst. 4 (2020) 2000078.
[90] J. Duan, Y. Zhao, B. He, Q. Tang, High-Purity Inorganic Perovskite Films for Solar Cells with 9.72 % Efficiency, Angew. Chem. Int. Ed. 57 (2018) 3787-3791.
[91] Y. Jiang, M.R. Leyden, L. Qiu, S. Wang, L.K. Ono, Z. Wu, E.J. Juarez-Perez, Y. B. Qi, Combination of Hybrid CVD and Cation Exchange for Upscaling Cs-Substituted Mixed Cation Perovskite Solar Cells with High Efficiency and Stability, Adv. Funct. Mater. 28 (2018) 1703835.
[92] M.R. Leyden, L.K. Ono, S.R. Raga, Y. Kato, S. Wang, Y. B. Qi, High performance perovskite solar cells by hybrid chemical vapor deposition, J. Mater. Chem. A 2 (2014) 18742-18745.
[93] L. Qiu, Z. Liu, L.K. Ono, Y. Jiang, D.-Y. Son, Z. Hawash, S. He, Y. B. Qi, Scalable Fabrication of Stable High Efficiency Perovskite Solar Cells and Modules Utilizing Room Temperature Sputtered SnO_2 Electron Transport Layer, Adv. Funct. Mater. 29 (2019) 1806779.
[94] H. Lu, Y. Liu, P. Ahlawat, A. Mishra, W.R. Tress, F.T. Eickemeyer, Y. Yang, F. Fu, Z. Wang, C.E. Avalos, B.I. Carlsen, A. Agarwalla, X. Zhang, X. Li, Y. Zhan, S.M. Zakeeruddin, L. Emsley, U. Rothlisberger, L. Zheng, A. Hagfeldt, M. Gratzel, Vapor-assisted deposition of highly efficient, stable black-phase $FAPbI_3$ perovskite solar cells, Science 370 (2020) eabb8985.
[95] L.K. Ono, M.R. Leyden, S. Wang, Y. B. Qi, Organometal halide perovskite thin films and solar cells by vapor deposition, J. Mater. Chem. A 4 (2016) 6693-6713.
[96] L. Qiu, S. He, Y. Jiang, D.-Y. Son, L.K. Ono, Z. Liu, T. Kim, T. Bouloumis, S. Kazaoui, Y. B. Qi, Hybrid chemical vapor deposition enables scalable and stable Cs-FA mixed cation perovskite solar modules with a designated area of 91.8 cm^2 approaching 10% efficiency, J. Mater. Chem. A 7 (2019) 6920-6929.
[97] S. Wang, L.K. Ono, M.R. Leyden, Y. Kato, S.R. Raga, M.V. Lee, Y. B. Qi, Smooth perovskite thin films and efficient perovskite solar cells prepared by the hybrid deposition method, J. Mater. Chem. A 3 (2015) 14631-14641.
[98] J. Lei, F. Gao, H. Wang, J. Li, J. Jiang, X. Wu, R. Gao, Z. Yang, S. Liu, Efficient planar $CsPbBr_3$ perovskite solar cells by dual-source vacuum evaporation, Sol. Energy Mater. Sol. Cells, 187 (2018) 1-8.
[99] Y. Zhang, L. Luo, J. Hua, C. Wang, F. Huang, J. Zhong, Y. Peng, Z. Ku, Y.-b. Cheng, Moisture assisted $CsPbBr_3$ film growth for high-efficiency, all-inorganic solar cells prepared by a multiple sequential vacuum deposition method, Materials Science in Semiconductor Processing, 98 (2019) 39-43.
[100] G. Tong, T. Chen, H. Li, L. Qiu, Z. Liu, Y. Dang, W. Song, L.K. Ono, Y. Jiang, Y. B. Qi, Phase transition induced recrystallization and low surface potential barrier leading to 10.91%-efficient $CsPbBr_3$ perovskite solar cells, Nano Energy 65 (2019) 104015.

[101] Z. Wu, S.R. Raga, E.J. Juarez-Perez, X. Yao, Y. Jiang, L.K. Ono, Z. Ning, H. Tian, Y. B. Qi, Improved Efficiency and Stability of Perovskite Solar Cells Induced by C=O Functionalized Hydrophobic Ammonium-Based Additives, Adv. Mater. 30 (2018) 1703670.
[102] Z. Liu, L.K. Ono, Y. B. Qi, Additives in metal halide perovskite films and their applications in solar cells, J. Energy Chem. 46 (2020) 215-228.
[103] J. Peng, D. Walter, Y. Ren, M. Tebyetekerwa, Y. Wu, T. Duong, Q. Lin, J. Li, T. Lu, M.A. Mahmud, O.L.C. Lem, S. Zhao, W. Liu, Y. Liu, H. Shen, L. Li, F. Kremer, H.T. Nguyen, D.-Y. Choi, K.J. Weber, K.R. Catchpole, T.P. White, Nanoscale localized contacts for high fill factors in polymer-passivated perovskite solar cells, Science 371 (2021) 390-395.
[104] Z. Wu, M. Jiang, Z. Liu, A. Jamshaid, L.K. Ono, Y. B. Qi, Highly Efficient Perovskite Solar Cells Enabled by Multiple Ligand Passivation, Adv. Energy Mater. 10 (2020) 1903696.
[105] W. Zhao, Z. Yao, F. Yu, D. Yang, S. Liu, Alkali Metal Doping for Improved $CH_3NH_3PbI_3$ Perovskite Solar Cells, Adv. Sci. 5 (2018) 1700131.
[106] Y. Li, J. Duan, H. Yuan, Y. Zhao, B. He, Q. Tang, Lattice Modulation of Alkali Metal Cations Doped $Cs_{1-x}R_xPbBr_3$ Halides for Inorganic Perovskite Solar Cells, Solar RRL 2 (2018) 1800164.
[107] Duan, Y. Zhao, X. Yang, Y. Wang, B. He, Q. Tang, Lanthanide Ions Doped $CsPbBr_3$ Halides for HTM-Free 10.14%-Efficiency Inorganic Perovskite Solar Cell with an Ultrahigh Open-Circuit Voltage of 1.594 V, Adv. Energy Mater. 8 (2018) 1802346.
[108] T. Chen, G. Tong, E. Xu, H. Li, P. Li, Z. Zhu, J. Tang, Y. B. Qi, Y. Jiang, Accelerating hole extraction by inserting 2D Ti_3C_2-MXene interlayer to all inorganic perovskite solar cells with long-term stability, J. Mater. Chem. A 7 (2019) 20597-20603.
[109] J. Duan, Y. Zhao, Y. Wang, X. Yang, Q. Tang, Hole-Boosted $Cu(Cr,M)O_2$ Nanocrystals for All-Inorganic $CsPbBr_3$ Perovskite Solar Cells, Angew. Chem. Int. Ed. 58 (2019) 16147-16151.
[110] Y. Zhao, J. Duan, H. Yuan, Y. Wang, X. Yang, B. He, Q. Tang, Using SnO_2 QDs and $CsMBr_3$ (M = Sn, Bi, Cu) QDs as Charge-Transporting Materials for 10.6%-Efficiency All-Inorganic $CsPbBr_3$ Perovskite Solar Cells with an Ultrahigh Open-Circuit Voltage of 1.610 V, Solar RRL 3 (2019) 1800284.
[111] X. Li, Y. Tan, H. Lai, S. Li, Y. Chen, S. Li, P. Xu, J. Yang, All-Inorganic $CsPbBr_3$ Perovskite Solar Cells with 10.45% Efficiency by Evaporation-Assisted Deposition and Setting Intermediate Energy Levels, ACS Appl. Mater. Interfaces 11 (2019) 29746-29752.
[112] H. Yuan, Y. Zhao, J. Duan, Y. Wang, X. Yang, Q. Tang, All-inorganic $CsPbBr_3$ perovskite solar cell with 10.26% efficiency by spectra engineering, J. Mater. Chem. A 6 (2018) 24324-24329.
[113] G. Tong, T. Chen, H. Li, W. Song, Y. Chang, J. Liu, L. Yu, J. Xu, Y. B. Qi, Y. Jiang, High Efficient Hole Extraction and Stable All-Bromide Inorganic Perovskite Solar Cells via Derivative-Phase Gradient Bandgap Architecture, Solar RRL 3 (2019) 1900030.
[114] J. Duan, T. Hu, Y. Zhao, B. He, Q. Tang, Carbon-Electrode-Tailored All-Inorganic Perovskite Solar Cells To Harvest Solar and Water-Vapor Energy, Angew. Chem. Int. Ed. 57 (2018) 5746-5749.
[115] Q.A. Akkerman, M. Gandini, F. Di Stasio, P. Rastogi, F. Palazon, G. Bertoni, J.M. Ball, M. Prato, A. Petrozza, L. Manna, Strongly emissive perovskite nanocrystal inks for high-voltage solar cells, Nat. Energy 2 (2016) 16194.

[116] J. Duan, Y. Zhao, B. He, Q. Tang, Simplified Perovskite Solar Cell with 4.1% Efficiency Employing Inorganic $CsPbBr_3$ as Light Absorber, Small 14 (2018) 1704443.
[117] J. Duan, M. Wang, Y. Wang, J. Zhang, Q. Guo, Q. Zhang, Y. Duan, Q. Tang, Effect of Side-Group-Regulated Dipolar Passivating Molecules on $CsPbBr_3$ Perovskite Solar Cells, ACS Energy Lett. (2021) 2336-2342.
[118] F.T. Si, O. Isabella, M. Zeman, Too Many Junctions? A Case Study of Multijunction Thin-Film Silicon Solar Cells, Adv. Sustain. Syst. 1 (2017) 1700077.
[119] Q. Ma, S. Huang, X. Wen, M.A. Green, A.W.Y. Ho-Baillie, Hole Transport Layer Free Inorganic $CsPbIBr_2$ Perovskite Solar Cell by Dual Source Thermal Evaporation, Adv. Energy Mater. 6 (2016) 1502202.
[120] C.F.J. Lau, X. Deng, Q. Ma, J. Zheng, J.S. Yun, M.A. Green, S. Huang, A.W.Y. Ho-Baillie, $CsPbIBr_2$ Perovskite Solar Cell by Spray-Assisted Deposition, ACS Energy Lett. 1 (2016) 573-577.
[121] Y. Guo, X. Yin, J. Liu, W. Que, Highly efficient $CsPbIBr_2$ perovskite solar cells with efficiency over 9.8% fabricated using a preheating-assisted spin-coating method, J. Mater. Chem. A 7 (2019) 19008-19016.
[122] J. Bian, Y. Wu, W. Bi, L. Liu, X. Su, B. Zhang, Efficient $CsPbIBr_2$ Perovskite Solar Cells: Precise Control of Film Growth through the Application of Organic Iodized Salt and Anti-solvent, Energy Fuels 34 (2020) 11472-11478.
[123] W. Zhu, Q. Zhang, D. Chen, Z. Zhang, Z. Lin, J. Chang, J. Zhang, C. Zhang, Y. Hao, Intermolecular Exchange Boosts Efficiency of Air-Stable, Carbon-Based All-Inorganic Planar $CsPbIBr_2$ Perovskite Solar Cells to Over 9%, Adv. Energy. Mater. 8 (2018) 1802080.
[124] J. Liang, Z. Liu, L. Qiu, Z. Hawash, L. Meng, Z. Wu, Y. Jiang, L.K. Ono, Y. B. Qi, Enhancing Optical, Electronic, Crystalline, and Morphological Properties of Cesium Lead Halide by Mn Substitution for High-Stability All-Inorganic Perovskite Solar Cells with Carbon Electrodes, Adv. Energy Mater. 8 (2018) 1800504.
[125] J. Liang, P. Zhao, C. Wang, Y. Wang, Y. Hu, G. Zhu, L. Ma, J. Liu, Z. Jin, $CsPb_{0.9}Sn_{0.1}IBr_2$ Based All-Inorganic Perovskite Solar Cells with Exceptional Efficiency and Stability, J. Am. Chem. Soc. 139 (2017) 14009-14012.
[126] W.S. Subhani, K. Wang, M. Du, X. Wang, S. Liu, Interface-Modification-Induced Gradient Energy Band for Highly Efficient $CsPbIBr_2$ Perovskite Solar Cells, Adv. Energy Mater. 9 (2019) 1803785.
[127] W. Zhu, Z. Zhang, W. Chai, Q. Zhang, D. Chen, Z. Lin, J. Chang, J. Zhang, C. Zhang, Y. Hao, Band Alignment Engineering Towards High Efficiency Carbon-Based Inorganic Planar $CsPbIBr_2$ Perovskite Solar Cells, Chemsuschem 12 (2019) 2318-2325.
[128] R.J. Sutton, G.E. Eperon, L. Miranda, E.S. Parrott, B.A. Kamino, J.B. Patel, M.T. Hörantner, M.B. Johnston, A.A. Haghighirad, D.T. Moore, H.J. Snaith, Bandgap-Tunable Cesium Lead Halide Perovskites with High Thermal Stability for Efficient Solar Cells, Adv. Energy Mater. 6 (2016) 1502458.
[129] Q. Ma, S. Huang, S. Chen, M. Zhang, C.F.J. Lau, M.N. Lockrey, H.K. Mulmudi, Y. Shan, J. Yao, J. Zheng, X. Deng, K. Catchpole, M.A. Green, A.W.Y. Ho-Baillie, The Effect of Stoichiometry on the Stability of Inorganic Cesium Lead Mixed-Halide Perovskites Solar Cells, J. Phys. Chem. C 121 (2017) 19642-19649.

[130] Y. Wang, T. Zhang, F. Xu, Y. Li, Y. Zhao, A Facile Low Temperature Fabrication of High Performance $CsPbI_2Br$ All-Inorganic Perovskite Solar Cells, Solar RRL 2 (2018) 1700180.
[131] Z. Zeng, J. Zhang, X. Gan, H. Sun, M. Shang, D. Hou, C. Lu, R. Chen, Y. Zhu, L. Han, In Situ Grain Boundary Functionalization for Stable and Efficient Inorganic $CsPbI_2Br$ Perovskite Solar Cells, Adv. Energy Mater. 8 (2018) 1801050.
[132] J. Xue, R. Wang, K. Wang, Z. Wang, I. Yavuz, Y. Wang, Y. Yang, X. Gao, T. Huang, S. Nuryyeva, J. Lee, Y. Duan, L. Liao, R. Kaner, Y. Yang, Crystalline Liquid-Like Behaviro: Surface-Induced Secondary Grain Growth of Photovoltaic Perovskite Thin Film, J. Am. Chem. Soc. 141 (2019) 13948-13953.
[133] M. Wang, F. Cao, M. Wang, K. Deng, L. Li, Intermediate-Adduct-Assisted Growth of Stable $CsPbI_2Br$ Inorganic Perovskite Films for High-Efficiency Semitransparent Solar Cells, Adv. Mater. 33 (2021) 2006745.
[134] J.V. Patil, S.S. Mali, C.K. Hong, A-Site Rubidium Cation-Incorporated $CsPbI_2Br$ All-Inorganic Perovskite Solar Cells Exceeding 17% Efficiency, Solar RRL 4 (2020) 2000164.
[135] L. Wang, H. Zhou, J. Hu, B. Huang, M. Sun, B. Dong, G. Zheng, Y. Huang, Y. Chen, L. Li, Z. Xu, N. Li, Z. Liu, Q. Chen, L. Dun. C. Yan, A $Eu^{3+}Eu^{2+}$ ion redox shuttle imparts operational durability to Pb-I perovskite solar cells, Science 363 (2019) 265-270.
[136] W. Xiang, Z. Wang, D.J. Kubicki, W. Tress, J. Luo, D. Prochowicz, S. Akin, L. Emsley, J. Zhou, G. Dietler, M. Grätzel, A. Hagfeldt, Europium-Doped $CsPbI_2Br$ for Stable and Highly Efficient Inorganic Perovskite Solar Cells, Joule 3 (2019) 205-214.
[137] C.F.J. Lau, M. Zhang, X. Deng, J. Zheng, J. Bing, Q. Ma, J. Kim, L. Hu, M.A. Green, S. Huang, A. Ho-Baillie, Strontium-Doped Low-Temperature-Processed $CsPbI_2Br$ Perovskite Solar Cells, ACS Energy Lett. 2 (2017) 2319-2325.
[138] J.K. Nam, S.U. Chai, W. Cha, Y.J. Choi, W. Kim, M.S. Jung, J. Kwon, D. Kim, J.H. Park, Potassium Incorporation for Enhanced Performance and Stability of Fully Inorganic Cesium Lead Halide Perovskite Solar Cells, Nano Lett. 17 (2017) 2028-2033.
[139] D. Bai, J. Zhang, Z. Jin, H. Bian, K. Wang, H. Wang, L. Liang, Q. Wang, S.F. Liu, Interstitial Mn^{2+}-Driven High-Aspect-Ratio Grain Growth for Low-Trap-Density Microcrystalline Films for Record Efficiency $CsPbI_2Br$ Solar Cells, ACS Energy Lett. 3 (2018) 970-978.
[140] F. Yang, D. Hirotani, G. Kapil, M.A. Kamarudin, C.H. Ng, Y. Zhang, Q. Shen, S. Hayase, All-Inorganic $CsPb_{1-x}Ge_xI_2Br$ Perovskite with Enhanced Phase Stability and Photovoltaic Performance, Angew. Chem. Int. Ed. 57 (2018) 12745-12749.
[141] L. Fu, Y. Zhang, B. Chang, B. Li, S. Zhou, L. Zhang, L. Yin, A fluorine-modulated bulk-phase heterojunction and tolerance factor for enhanced performance and structure stability of cesium lead halide perovskite solar cells, J. Mater. Chem. A 6 (2018) 13263-13270.
[142] H. Bian, D. Bai, Z. Jin, K. Wang, L. Liang, H. Wang, J. Zhang, Q. Wang, S. Liu, Graded Bandgap $CsPbI_{2+x}Br_{1-x}$ Perovskite Solar Cells with a Stabilized Efficiency of 14.4%, Joule 2 (2018) 1500-1510.
[143] J. Zhang, D. Bai, Z. Jin, H. Bian, K. Wang, J. Sun, Q. Wang, S. Liu, 3D–2D–0D Interface Profiling for Record Efficiency All-Inorganic $CsPbBrI_2$ Perovskite Solar Cells with Superior Stability, Adv. Energy Mater. 8 (2018) 1703246.

[144] J. He, J. Su, Z. Lin, J. Ma, L. Zhou, S. Zhang, S. Liu, J. Chang, Y. Hao, Enhanced Efficiency and Stability of All-Inorganic $CsPbI_2Br$ Perovskite Solar Cells by Organic and Ionic Mixed Passivation, Adv. Sci. 8 (2021) 2101376.
[145] N. Li, Z. Zhu, J. Li, A.K.-Y. Jen, L. Wang, Inorganic $CsPb_{1-x}Sn_xIBr_2$ for Efficient Wide-Bandgap Perovskite Solar Cells, Adv. Energy Mater. 8 (2018) 1800525.
[146] Y. You, W. Tian, M. Wang, F. Cao, H. Sun, L. Li, PEG Modified $CsPbIBr_2$ Perovskite Film for Efficient and Stable Solar Cells, Adv. Mater. Interfaces 7 (2020) 2000537.
[147] B. Gao, J. Meng, Highly Stable All-Inorganic $CsPbIBr_2$ Perovskite Solar Cells with 11.30% Efficiency Using Crystal Interface Passivation, ACS Appl. Energy Mater. 3 (2020) 8249-8256.
[148] H. Wang, S. Cao, B. Yang, H. Li, M. Wang, X. Hu, K. Sun, Z. Zang, NH_4Cl-Modified ZnO for High-Performance $CsPbIBr_2$ Perovskite Solar Cells via Low-Temperature Process, Solar RRL 4 (2020) 1900363.
[149] H. Wang, H. Li, S. Cao, M. Wang, J. Chen, Z. Zang, Interface Modulator of Ultrathin Magnesium Oxide for Low-Temperature-Processed Inorganic $CsPbIBr_2$ Perovskite Solar Cells with Efficiency Over 11%, Solar RRL 4 (2020) 2000226.
[150] C. Zhang, K. Wang, Y. Wang, W.S. Subhani, X. Jiang, S. Wang, H. Bao, L. Liu, L. Wan, S. Liu, Low-Temperature Crystallization of $CsPbIBr_2$ Perovskite for High Performance Solar Cells, Solar RRL 4 (2020) 2000254.
[151] Q. Zeng, X. Zhang, X. Feng, S. Lu, Z. Chen, X. Yong, S.A.T. Redfern, H. Wei, H. Wang, H. Shen, W. Zhang, W. Zheng, H. Zhang, J.S. Tse, B. Yang, Polymer-Passivated Inorganic Cesium Lead Mixed-Halide Perovskites for Stable and Efficient Solar Cells with High Open-Circuit Voltage over 1.3 V, Adv. Mater. 30 (2018) 1705393.
[152] C. Liu, W. Li, C. Zhang, Y. Ma, J. Fan, Y. Mai, All-Inorganic $CsPbI_2Br$ Perovskite Solar Cells with High Efficiency Exceeding 13%, J. Am. Chem. Soc. 140 (2018) 3825-3828.
[153] J.H. Heo, F. Zhang, C. Xiao, S.J. Heo, J.K. Park, J.J. Berry, K. Zhu, S.H. Im, Efficient and Stable Graded $CsPbI_{3-x}Br_x$ Perovskite Solar Cells and Submodules by Orthogonal Processable Spray Coating, Joule 5 (2021) 481-494.
[154] G. Yin, H. Zhao, H. Jiang, S. Yuan, T. Niu, K. Zhao, Z. Liu, S. Liu, Precursor Engineering for All-Inorganic $CsPbI_2Br$ Perovskite Solar Cells with 14.78% Efficiency, Adv. Funct. Mater. 28 (2018) 1803269.
[155] Y. Han, H. Zhao, C. Duan, S. Yang, Z. Yang, Z. Liu, S. Liu, Controlled n-Doping in Air-Stable $CsPbI_2Br$ Perovskite Solar Cells with a Record Efficiency of 16.79%, Adv. Funct. Mater. 30 (2020) 1909972.
[156] D. Zhou, J. Huang, J. Liu, H. Yan, J. Zhang, M. Zhang, G. Liang, L. Lu, X. Zhang, P. Xu, H.-S. Kwok, G. Li, Dual Passivation Strategy for High Efficiency Inorganic $CsPbI_2Br$ Solar Cells, Solar RRL 5 (2021) 2100112.
[157] S. Yang, W. Liu, Y. Han, Z. Liu, W. Zhao, C. Duan, Y. Che, H. Gu, Y. Li, S. Liu, 2D $Cs_2PbI_2Cl_2$ Nanosheets for Holistic Passivation of Inorganic $CsPbI_2Br$ Perovskite Solar Cells for Improved Efficiency and Stability, Adv. Energy. Mater. 10 (2020) 2002882.
[158] C. Liu, J. He, M. Wu, Y. Wu, P. Du, L. Fan, Q. Zhang, D. Wang, T. Zhang, All-Inorganic $CsPbI_2Br$ Perovskite Solar Cell with Open-Circuit Voltage over 1.3 V by Balancing Electron and Hole Transport, Solar RRL 4 (2020) 2000016.

[159] Y. Zhang, C. Wu, D. Wang, Z. Zhang, X. Qi, N. Zhu, G. Liu, X. Li, H. Hu, Z. Chen, L. Xiao, B. Qu, High Efficiency (16.37%) of Cesium Bromide—Passivated All-Inorganic $CsPbI_2Br$ Perovskite Solar Cells, Solar RRL 3 (2019) 1900254.
[160] H. Peng, M. Cai, J. Zhou, Y. Yang, X. Ding, Y. Tao, G. Wu, X. Liu, J.H. Pan, S. Dai, Structurally Reinforced All-Inorganic $CsPbI_2Br$ Perovskite by Nonionic Polymer via Coordination and Hydrogen Bonds, Solar RRL 4 (2020) 2000216.
[161] H. Li, L. Yin, Efficient Bidentate Molecules Passivation Strategy for High-Performance and Stable Inorganic $CsPbI_2Br$ Perovskite Solar Cells, Solar RRL 4 (2020) 2000268.
[162] Q. Yuan, S. Yi, D. Han, F. Wang, Q. Li, R. Huang, Y. Cui, R. Zheng, D.-Y. Zhou, L. Feng, S_8 Additive Enables $CsPbI_2Br$ Perovskite with Reduced Defects and Improved Hydrophobicity for Inverted Solar Cells, Solar RRL 5 (2021) 2000714.
[163] G.E. Eperon, G.M. Paternò, R.J. Sutton, A. Zampetti, A.A. Haghighirad, F. Cacialli, H.J. Snaith, Inorganic caesium lead iodide perovskite solar cells, J. Mater. Chem. A 3 (2015) 19688-19695.
[164] P. Wang, X. Zhang, Y. Zhou, Q. Jiang, Q. Ye, Z. Chu, X. Li, X. Yang, Z. Yin, J. You, Solvent-controlled growth of inorganic perovskite films in dry environment for efficient and stable solar cells, Nat. Commun. 9 (2018) 2225.
[165] J. Liang, C. Wang, P. Zhao, Z. Lu, Y. Ma, Z. Xu, Y. Wang, H. Zhu, Y. Hu, G. Zhu, L. Ma, T. Chen, Z. Tie, J. Liu, Z. Jin, Solution synthesis and phase control of inorganic perovskites for high-performance optoelectronic devices, Nanoscale 9 (2017) 11841-11845.
[166] C.F.J. Lau, Z. Wang, N. Sakai, J. Zheng, C.H. Liao, M. Green, S. Huang, H.J. Snaith, A. Ho-Baillie, Fabrication of Efficient and Stable $CsPbI_3$ Perovskite Solar Cells through Cation Exchange Process, Adv. Energy Mater. 9 (2019) 1901685.
[167] J. Yuan, X. Ling, D. Yang, F. Li, S. Zhou, J. Shi, Y. Qian, J. Hu, Y. Sun, Y. Yang, X. Gao, S. Duhm, Q. Zhang, W. Ma, Band-Aligned Polymeric Hole Transport Materials for Extremely Low Energy Loss α-$CsPbI_3$ Perovskite Nanocrystal Solar Cells, Joule 2 (2018) 2450-2463.
[168] E.M. Sanehira, A.R. Marshall, J.A. Christians, S.P. Harvey, P.N. Ciesielski, L.M. Wheeler, P. Schulz, L.Y. Lin, M.C. Beard, J.M. Luther, Enhanced mobility $CsPbI_3$ quantum dot arrays for record-efficiency, high-voltage photovoltaic cells, Sci. Adv. 3 (2017) eaao4204.
[169] L.A. Frolova, D.V. Anokhin, A.A. Piryazev, S.Y. Luchkin, N.N. Dremova, K.J. Stevenson, P.A. Troshin, Highly Efficient All-Inorganic Planar Heterojunction Perovskite Solar Cells Produced by Thermal Coevaporation of CsI and PbI_2. J. Phys. Chem. Lett. 8 (2017) 67-72.
[170] C.-Y. Chen, H.-Y. Lin, K.-M. Chiang, W.-L. Tsai, Y.-C. Huang, C.-S. Tsao, H.-W. Lin, All-Vacuum-Deposited Stoichiometrically Balanced Inorganic Cesium Lead Halide Perovskite Solar Cells with Stabilized Efficiency Exceeding 11%, Adv. Mater. 29 (2017) 1605290.
[171] J. Liang, X. Han, J.-H. Yang, B. Zhang, Q. Fang, J. Zhang, Q. Ai, M.M. Ogle, T. Terlier, A.A. Martí, J. Lou, Defect-Engineering-Enabled High-Efficiency All-Inorganic Perovskite Solar Cells, Adv. Mater. 31 (2019) 1903448.
[172] F. Liu, C. Ding, Y. Zhang, T.S. Ripolles, T. Kamisaka, T. Toyoda, S. Hayase, T. Minemoto, K. Yoshino, S. Dai, M. Yanagida, H. Noguchi, Q. Shen, Colloidal Synthesis of Air-Stable Alloyed $CsSn_{1-x}Pb_xI_3$ Perovskite Nanocrystals for Use in Solar Cells, J. Am. Chem. Soc. 139 (2017) 16708-16719.

[173] F. Liu, C. Ding, Y. Zhang, T. Kamisaka, Q. Zhao, J.M. Luther, T. Toyoda, S. Hayase, T. Minemoto, K. Yoshino, B. Zhang, S. Dai, J. Jiang, S. Tao, Q. Shen, GeI_2 Additive for High Optoelectronic Quality $CsPbI_3$ Quantum Dots and Their Application in Photovoltaic Devices, Chem. Mater. 31 (2019) 798-807.
[174] Y. Hu, F. Bai, X. Liu, Q. Ji, X. Miao, T. Qiu, S. Zhang, Bismuth Incorporation Stabilized α-$CsPbI_3$ for Fully Inorganic Perovskite Solar Cells, ACS Energy Lett. 2 (2017) 2219-2227.
[175] H. Zhao, J. Xu, S. Zhou, Z. Li, B. Zhang, X. Xia, X. Liu, S. Dai, J. Yao, Preparation of Tortuous 3D γ-$CsPbI_3$ Films at Low Temperature by CaI_2 as Dopant for Highly Efficient Perovskite Solar Cells, Adv. Funct. Mater. 29 (2019) 1808986.
[176] C.F.J. Lau, X. Deng, J. Zheng, J. Kim, Z. Zhang, M. Zhang, J. Bing, B. Wilkinson, L. Hu, R. Patterson, S. Huang, A. Ho-Baillie, Enhanced performance via partial lead replacement with calcium for a $CsPbI_3$ perovskite solar cell exceeding 13% power conversion efficiency, J. Mater. Chem. A 6 (2018) 5580-5586.
[177] S. Xiang, W. Li, Y. Wei, J. Liu, H. Liu, L. Zhu, H. Chen, The synergistic effect of non-stoichiometry and Sb-doping on air-stable α-$CsPbI_3$ for efficient carbon-based perovskite solar cells, Nanoscale 10 (2018) 9996-10004.
[178] A.K. Jena, A. Kulkarni, Y. Sanehira, M. Ikegami, T. Miyasaka, Stabilization of α-$CsPbI_3$ in Ambient Room Temperature Conditions by Incorporating Eu into $CsPbI_3$, Chem. Mater. 30 (2018) 6668-6674.
[179] Z. Yao, Z. Jin, X. Zhang, Q. Wang, H. Zhang, Z. Xu, L. Ding, S. Liu, Pseudohalide (SCN^-)-doped $CsPbI_3$ for high-performance solar cells, J. Mater. Chem. C 7 (2019) 13736-13742.
[180] G. Murugadoss, R. Thangamuthu, Metals doped cesium based all inorganic perovskite solar cells: Investigations on Structural, morphological and optical properties, Sol. Energy 179 (2019) 151-163.
[181] Z. Yao, W. Zhao, S. Chen, Z. Jin, S.F. Liu, Mn Doping of $CsPbI_3$ Film Towards High-Efficiency Solar Cell, ACS Appl. Energy Mater. 3 (2020) 5190-5197.
[182] Q. Wang, X. Zheng, Y. Deng, J. Zhao, Z. Chen, J. Huang, Stabilizing the α-Phase of $CsPbI_3$ Perovskite by Sulfobetaine Zwitterions in One-Step Spin-Coating Films, Joule 1 (2017) 371-382.
[183] B. Li, Y. Zhang, L. Fu, T. Yu, S. Zhou, L. Zhang, L. Yin, Surface passivation engineering strategy to fully-inorganic cubic $CsPbI_3$ perovskites for high-performance solar cells, Nat. Commun. 9 (2018) 1076.
[184] Y. Jiang, J. Yuan, Y. Ni, J. Yang, Y. Wang, T. Jiu, M. Yuan, J. Chen, Reduced-Dimensional α-$CsPbX_3$ Perovskites for Efficient and Stable Photovoltaics, Joule 2 (2018) 1356-1368.
[185] B. Yu, J. Shi, S. Tan, Y. Cui, W. Zhao, H. Wu, Y. Luo, D. Li, Q. Meng, Efficient (>20 %) and Stable All-Inorganic Cesium Lead Triiodide Solar Cell Enabled by Thiocyanate Molten Salts, Angew. Chem. Int. Ed. 60 (2021) 13436-13443.
[186] K. Sakthi Velu, J. Anandha Raj, P. Sathappan, B. Suganya Bharathi, S. Mohan Doss, S. Selvam, P. Manisankar, T. Stalin, Poly (ethylene glycol) stabilized synthesis of inorganic cesium lead iodide polycrystalline light-absorber for perovskite solar cell, Mater. Lett. 240 (2019) 132-135.
[187] Z. Wu, Z. Liu, Z. Hu, Z. Hawash, L. Qiu, Y. Jiang, L.K. Ono, Y. B. Qi, Highly Efficient and Stable Perovskite Solar Cells via Modification of Energy Levels at the Perovskite/Carbon Electrode Interface, Adv. Mater. 31 (2019) 1804284.

[188] C. Yan, Z. Li, Y. Sun, J. Zhao, X. Huang, J. Yang, Z. Ci, L. Ding, Z. Jin, Decreasing energy loss and optimizing band alignment for high performance $CsPbI_3$ solar cells through guanidine hydrobromide post-treatment, J. Mater. Chem. A 8 (2020) 10346-10353.
[189] F. Bai, J. Zhang, Y. Yuan, H. Liu, X. Li, C.-C. Chueh, H. Yan, Z. Zhu, A.K.-Y. Jen, A 0D/3D Heterostructured All-Inorganic Halide Perovskite Solar Cell with High Performance and Enhanced Phase Stability, Adv. Mater. 31 (2019) 1904735.
[190] P. Luo, W. Xia, S. Zhou, L. Sun, J. Cheng, C. Xu, Y. Lu, Solvent Engineering for Ambient-Air-Processed, Phase-Stable $CsPbI_3$ in Perovskite Solar Cells, J. Phys. Chem. Lett. 7 (2016) 3603-3608.
[191] H. Wang, H. Liu, Z. Dong, W. Li, L. Zhu, H. Chen, Composition Manipulation Boosts the Efficiency of Carbon-based $CsPbI_3$ Perovskite Solar Cells to Beyond 14%, Nano Energy 84 (2021) 105881.
[192] S.M. Yoon, H. Min, J.B. Kim, G. Kim, K.S. Lee, S.I. Seok, Surface Engineering of Ambient-Air-Processed Cesium Lead Triiodide Layers for Efficient Solar Cells, Joule 5 (2021) 183-196.
[193] A. Shpatz Dayan, B.-E. Cohen, S. Aharon, C. Tenailleau, M. Wierzbowska, L. Etgar, Enhancing Stability and Photostability of $CsPbI_3$ by Reducing Its Dimensionality, Chem. Mater. 30 (2018) 8017-8024.
[194] Y. Wang, T. Zhang, M. Kan, Y. Zhao, Bifunctional Stabilization of All-Inorganic α-$CsPbI_3$ Perovskite for 17% Efficiency Photovoltaics, J. Am. Chem. Soc. 140 (2018) 12345-12348.
[195] Y. Wang, T. Zhang, M. Kan, Y. Li, T. Wang, Y. Zhao, Efficient α-$CsPbI_3$ Photovoltaics with Surface Terminated Organic Cations, Joule 2 (2018) 2065-2075.
[196] Y. Wang, G. Chen, D. Ouyang, X. He, C. Li, R. Ma, W.-J. Yin, W.C.H. Choy, High Phase Stability in $CsPbI_3$ Enabled by Pb–I Octahedra Anchors for Efficient Inorganic Perovskite Photovoltaics, Adv. Mater. 32 (2020) 2000186.
[197] T. Zhang, M.I. Dar, G. Li, F. Xu, N. Guo, M. Grätzel, Y. Zhao, Bication lead iodide 2D perovskite component to stabilize inorganic α-$CsPbI_3$ perovskite phase for high-efficiency solar cells, Sci. Adv. 3 (2017) e1700841.
[198] USA Environmental Protection Agency Lead Laws and Regulations. http://www2.epa.gov/lead/lead-laws-and-regulations (08/26/2021).
[199] B. Hailegnaw, S. Kirmayer, E. Edri, G. Hodes, D. Cahen, Rain on Methylammonium Lead Iodide Based Perovskites: Possbile Environmental Effects of Perovskite Solar Cells. J. Phys. Chem. Lett. 6 (2015) 1543-1547.
[200] P. Su, Y. Liu, J. Zhang, C. Chen, B. Yang, C. Zhang, X. Zhao, Pb-Based Perovskite Solar Cells and the Underlying Pollution behind Clean Energy: Dynamic Leaching of Toxic Substances from Discarded Perovskite Solar Cells, J. Phys. Chem. Lett. 11 (2020) 2812-2817.
[201] M. H. Kumar, S. Dharani, W. L. Leong, P. P. Boix, R. R. Prabhakar, T. Baikie, C. Shi, H. Ding, R. Ramesh, M. Asta, M. Graetzel, S. G. Mhaisalkar, N. Mathews, Lead-Free Halide Perovskite Solar Cells with High Photocurrents Realized Through Vacancy Modulation. Advanced Materials 26 (2014) 7122-7127.
[202] X. Han, J. Liang, J. Yang, K. Soni, Q. Fang, W. Wang, J. Zhang, S. Jia, A. A. Martí, Y. Zhao, J. Lou, Lead-free Double Perovskite Cs_2SnX_6: Facile Soluiton Synthesis and Excellent Stability, Small 15 (2019) 1901650.

[203] B. Wu, W. Ning, Q. Xu, M. Manjappa, M. Feng, S. Ye, J. Fu, S. Lie, T. Yin, F. Wang, T. W. Goh, P. C. Harikesh, Y. K. E. Tay, Z. X. Shen, F. Huang, R. Singh, G. Zhou, F. Gao, T. C. Sum, Strong Self-Trapping by Deformation Potential Limits Photovoltaic Performance in Bismuth Double Perovskite. Science Advances 7 (2021) eabd3160.
[204] B. Park, B. Philippe, X. Zhang, H. Rensmo, G. Boschloo, E. M. J. Johansson, Bismuth Based Hybrid Perovskites $A_3Bi_2I_9$ (A: Methylammonium or Cesium) for Solar Cell Application. Advanced Materials 27 (2015) 6806-6813.
[205] P. Xu, S. Chen, H. Xiang, X. Gong, S. Wei, Influence of Defects and Synthesis Conditions on the Photovoltaic Performance of Perovskite Semiconductor $CsSnI_3$. Chem. Mater. 26 (2014) 6068-6072.
[206] M. Chen, M. Ju, H. F. Garces, A. D. Carl, L. K. Ono, Z. Hawash, Y. Zhang, T. Shen, Y. Qi, R. L. Grimm, D. Pacifici, X. Zeng, Y. Zhou, N. P. Padture, Highly Stable and Efficient All-Inorganic Lead-Free Perovskite Solar Cells with Native-Oxide Passivation. Nat. Commun. 10 (2019) 16.
[207] T. Ye, K. Wang, Y. Hou, D. Yang, N. Smith, B. Magill, J. Yoon, R. R. H. H. Mudiyanselage, G. A. Khodaparast, K. Wang, S. Priya, Ambient-Air-Stable Lead-Free $CsSnI_3$ Solar Cells with Greater than 7.5% Efficiency. J. Am. Chem. Soc. 143 (2021) 4319-4328.
[208] J. Duan, H. Xu, W.E.I. Sha, Y. Zhao, Y. Wang, X. Yang, Q. Tang, Inorganic perovskite solar cells: an emerging member of the photovoltaic community, J. Mater. Chem. A 7 (2019) 21036-21068.
[209] F.H. Alharbi, S. Kais, Theoretical limits of photovoltaics efficiency and possible improvements by intuitive approaches learned from photosynthesis and quantum coherence, Renew. Sustain. Energy Rev. 43 (2015) 1073-1089.
[210] W. Shockley, H.J. Queisser, Detailed Balance Limit of Efficiency of p-n Junction Solar Cells, J. Appl. Phys. 32 (1961) 510-519.